UNDERSTANDING REGIONAL WATER RESOURCE DYNAMICS DUE TO LAND-COVER/LAND-USE AND CLIMATE CHANGES IN THE NORTH CAROLINA PIEDMONT

Josh Gray

A dissertation submitted to the faculty of the University of North Carolina at Chapel Hill in partial fulfillment of the requirements for the degree of Doctor of Philosophy in the Department of Geography.

Chapel Hill
2012

Approved by:

Conghe Song

Lawrence Band

Chip Konrad

Aaron Moody

Ge Sun

Abstract

JOSH GRAY: Understanding regional water resource dynamics due to land-cover/land-use and climate changes in the North Carolina Piedmont. (Under the direction of Conghe Song.)

The spatiotemporal distribution of freshwater resources on Earth is controlled by interacting climatologic, ecological, and physical processes. These dynamics are likely to change in the future due to climate and land cover changes with important implications for life on Earth. Ecosystem simulation models which couple these processes are increasingly relied upon to provide projections of probable future changes so that resources may be sustainably managed and future growth and development planned. The majority of these models depend critically on surface descriptions such as land cover and vegetation abundance obtained from remotely sensed images, and remote sensing methods have played an essential role in accurately parameterizing and implementing models at appreciable spatial scales. However, significant challenges exist for investigations adopting an integrated remote sensing and ecosystem simulation approach.

This investigation sought to quantify the likely impacts of climate change and land cover change on the water cycle of the Eno River basin in central North Carolina. Special attention was paid to addressing and overcoming existing remote sensing methodological limitations related to mapping leaf area index (LAI) and land cover. Improved methods were developed and the resulting products used to parameterize two different ecohydrologic models which were then used to quantify the hydrological effects of various climate and land cover change scenarios. The improved methods are demonstrated to overcome several of the major existing limitations to mapping LAI and land cover accurately, consistently, and efficiently with diverse data sources. These improvements lead to greater confidence in simulated results and future projections. The results of this investigation highlight the dominant role that climate plays in structuring basin response, and indicate that future changes may increase water stress in the area, particularly under scenarios of reduced growing season precipitation.

Acknowledgments

I am indebted to my advisor, Conghe Song, for his patient guidance and direction over the past several years. He challenged me to become a more careful and creative student of Earth science. His kindness and devotion to my growth has had a positive impact on my academic, professional, and personal development. I am grateful to my dissertation committee: Lawrence Band, Chip Konrad, Aaron Moody, and Ge Sun, whose support and insights have been invaluable in the development and refinement of this work. I am particularly grateful for Lawrence Band who granted me the opportunity to pursue this degree, and to Aaron Moody whose mentorship and friendship has enriched my personal and academic life. Additionally, I am thankful for the financial support of the NASA Earth and Space Science Fellowship program which has supported my graduate studies.

Outside of the university, I have benefited from the devotion and love of my family whose innumerable sacrifices have afforded me more opportunities than I deserve. I have found their unflagging support to be a great source of personal strength. I am indebted to friends and colleagues too numerous to name, particularly the brethren of the OSC. I am grateful for the support and encouragement of Courtney Gray, without whom this would not be possible. She is a picture of grace and a constant source of inspiration.

Table of Contents

List of Tables

List of Figures

Chapter 1
Introduction

Water is essential for life on Earth. Of the hydrosphere's 1,386 million cubic kilometers of water, 97.5% is saline. The 2.5% that is freshwater is 69% ice or permanent snow and 29.9% groundwater. The sum contents of all Earth's rivers, lakes, and reservoirs is only 0.26% of all freshwater stores (Shiklomanov, 2000). The spatiotemporal distribution of groundwater and surface resources are determined by climatic, physical, and biological processes. First order control on terrestrial water cycles is determined by climatic patterns of precipitation and temperature. Topographic controls distribute precipitation across the landscape through stream networks and lateral and vertical soil moisture fluxes. Vegetation covers much of Earth's surface and exerts a strong influence on local water balances through ecological water use (transpiration), and alterations of the surface energy budget. In temperate forested areas such as the southeastern United States, over 70% of the precipitation is returned to the atmosphere via transpiration or evaporation. This combined latent heat flux, known as evapotranspiration (ET), is an important component of terrestrial energy and water budgets. While the providence of precipitated water depends on the mesoscale weather patterns associated with a particular location, in regions like the Amazon, evapotranspired water is an important source of water vapor for local precipitation. In any case, the latent heat flux is an important component of surface energy budgets and is the process responsible for the generally appreciated cooling effect of forests. In turn, spatial patterns of temperature and precipitation control the distribution and composition of Earth's vegetation communities. These interactions between geological, climatological, and ecological processes are responsible for the observed patterns of surface and ground water resources on Earth, and future changes in their dynamics may alter water availability, vegetation water stress, and flood/drought frequency with important consequences

for life on Earth (Vorosmarty et al., 2000; Jackson et al., 2001).

Global climate modeling activities have progressed to ensemble efforts comprised of many individual models that are increasingly converging on future climate predictions under a variety of development and emissions scenarios. The most recent report of the Intergovernmental Panel on Climate Change (IPCC) indicates that anthropogenic activities, most notably emissions of greenhouse gases, has very likely contributed to an observed global warming pattern, and that these changes are likely to persist or be exacerbated in the future. Regional patterns of temperature change indicate that in the coming century high latitude areas will experience the greatest warming and increases in precipitation, while many already dry regions such as the western United States and Mediterranean stand to get significantly drier. These changes have important implications for water resources. In general, regions are expected to become more water stressed in the future due to decreases in glacial and snow fed river runoff, decreases in precipitation over many regions, salinization in coastal areas due to sea-level rise, and increased extreme event frequency (IPCC, 2007). In addition to overall changes in the magnitude of annual precipitation, changes in precipitation seasonality and variability may place additional strains on water availability with some regions transitioning to more extreme hydrologic regimes with longer, more intense droughts and a greater frequency of floods and extreme weather events (Oki and Kanae, 2006).

Land cover and land use influence local, regional, and global water cycles in a number of ways (DeFries et al., 2004; Foley et al., 2005; Piao et al., 2007; Scanlon et al., 2007). Surface physical properties determine the fate of precipitation by controlling the partitioning of water into evaporated, transpired, ground storage, and runoff. Vegetation distributions, most importantly abundance and composition, control the relative magnitudes of latent heat fluxes with important climate feedbacks related to relative atmospheric moisture content and surface energy fluxes. Land uses influence water balances through alteration of these surface physical properties and by determining consumptive withdrawals of freshwater from surface and ground stores and, in some cases, water inputs in the form of irrigation. Globally there is a trend toward increasingly human-dominated land uses that stand to appreciably impact water availability in the future (Brown et al., 2005b; White et al., 2009). Agricultural land uses are

replacing natural vegetation communities in many parts of the world, and impervious surface proportions are increasing in many developed and developing catchments. While increases in catchment impervious surface are generally well understood to produce more extreme, temporally variable patterns of runoff, other changes in land cover and land use, particularly vegetation changes, produce hydrologic changes that are mediated through a variety of eco-physiological processes and feedbacks that are more difficult to understand. Improved understanding of these processes and their various interactions is critical if hydrological sciences is to successfully inform environmental decision making and water resource management.

Assessing the impacts of future climate and land cover changes argues for a simulation modeling approach capable of modeling the interacting climatic, physical, and biological processes which determine water balances at multiple spatial and temporal scales (Rodriguez-Iturbe, 2000; Allen and Ingram, 2002; Jackson et al., 2009; Vose et al., 2011). Much progress has been made in developing these types of models, and there is a large diversity of approaches reported in the literature (Sellers et al., 1997). At one extreme are conceptually simple empirical models which seek to exploit relationships determined between measured variables such as streamflow, ET, and ecosystem productivity and environmental drivers. This pragmatic approach has multiple benefits including relatively rapid development and simple implementation. Despite their simplicity, these models are useful, especially for monitoring and management of contemporary conditions, because simulated processes are constrained by observed relationships and thus are likely to provide realistic estimates given similar environmental forcing regimes. However, empirical approaches have significant limitations, chiefly the inability to produce reliable results when biological, climatic, and physical process interactions change, invalidating established empirical relationships. At the other extreme, many recent modeling approaches have focused on detailed process models coupling many physical subcomponent models and their various interactions. These models typically have higher input data requirements, computational requirements, and generally more complicated implementations than their empirical counterparts. However, coupled models offer significant advantages, most importantly the ability to simulate complex, possibly non-linear, interactions between various processes and therefore have greater utility in assessing the impacts of future changes that may alter environmental

dynamics than do empirical models.

Regardless of the modeling approach adopted, there is a need for some quantity of input data to parameterize the model. These data include maps of land cover, vegetation composition and abundance distributions, climate series, topographic information, soils maps and parameters, stream network maps, and parameters describing the physical properties of vegetation and other land surfaces. Increasingly, remote sensing images and methods are employed to provide these data at the spatial scales necessary for modeling investigations (Lucas and Curran, 1999; DeFries, 2008). Among the model inputs available from remotely sensed images, topographic, vegetation, and land cover information are the most commonly retrieved and a robust literature has developed concerning the development and refinement of these techniques. Remote sensing methods of mapping land cover was one of the initial applications of remote sensing imagery and this subdiscipline enjoys the most robust literature in all of remote sensing science, with a multitude of *ad hoc* and operational approaches at spatial scales ranging from the entire Earth to a few hundred square meters. The importance of global vegetation distributions in influencing hydrologic and climatological processes has motivated a myriad of investigations seeking to characterize these distributions with remotely sensed images. Many efforts have focused on mapping leaf area index (LAI) from diverse data sources, but the majority of methods are predicated on the relationship between vegetation abundance and differential reflectance of electromagnetic radiation across different frequency intervals.

Despite the proven utility of remote sensing methods to provide more or less reliable estimates of land cover and vegetation distributions on Earth, there remain significant challenges that impose limitations on their use in modeling studies. With respect to land cover mapping, the most significant challenge is to leverage the vast and growing archives of Earth imagery to obtain consistent and accurate time series of land cover maps which may be used to assess historical dynamics and project future changes (Loveland et al., 2002). At present, products from the majority of large-scale land cover mapping initiatives have been limited in temporal resolution to consideration of a single or a few time points. The principal difficulty in obtaining temporally dense products is the lack of automated methods capable of efficiently utilizing huge data volumes and ensuring consistency between maps of land cover at various time intervals.

In short, existing methods either require extensive ground reference data and human intervention, or are limited by the requirement that individual images be identical in terms of spectral reflectance properties. There is therefore a need to develop efficient methods of utilizing existing data archives that overcome these existing limitations. Methods of mapping vegetation abundance, either biomass or LAI, are similarly limited by methodological challenges (Baret and Guyot, 1991; Asner et al., 2003; Ganguly et al., 2008b,a). The most commonly employed approach relates the greenness of a pixel to the density of vegetated canopies. However, once stands have reached a closed canopy condition the pixel greenness changes very little, and so the sensitivity of greenness measures to further increases in LAI diminishes. This leads to the inability to reliably retrieve estimates of vegetation abundance in high biomass regions. This is especially problematic considering that a large portion of Earth's vegetation exists in densely forested stands, and these areas exert the most significant impacts on climate and hydrological processes. The lack of temporal dimension in LAI products is also a significant limitation of these remote sensing methods. Typically, maps of LAI and biomass are produced for a single date in time (usually during the peak of the growing season), and therefore cannot offer insight on vegetation temporal dynamics. This is especially problematic for assimilating these data into ecosystem modeling investigations which typically require information about the temporal evolution of vegetation during the year.

This dissertation seeks to understand the individual and combined impacts of climate and land cover changes on the hydrology of a moderately sized (the 360 km^2 Eno River basin) watershed in central North Carolina. Quantifying the expected changes in water resources due to climate and land cover changes is critical in this area because rapidly growing regional populations are placing intense pressures on existing resources and reshaping the landscape (Burkett et al., 2000). I adopt an ecohydrolgic simulation approach utilizing two existing models which bracket the structural variability seen across ecohydrological models. An important feature of this investigation is its reliance on a modeling approach which integrates the best available data from remote sensing data sources. To this end, I focus on making significant methodological progress in remote sensing methods of characterizing land cover and vegetation distributions which improve the accuracy of model inputs and therefore the reliability of the

simulated results. I first develop a novel multi-sensor information fusion approach to mapping LAI which overcomes challenges related to retrieving estimates in high biomass stands and characterizing temporal vegetation patterns. Next, I address the limitations of existing land cover mapping approaches and develop a method capable of efficiently assimilating data from arbitrarily large archives in order to obtain consistent and accurate maps of temporal land cover dynamics with a minimum of user intervention and reference information. Finally, I use these products to parameterize two ecohydrolgic models, a process-oriented detailed physical model (RHESSys) and an empirically based model (WaSSI), and assess the impacts of multiple climate and land cover scenarios on long-term streamflow and ET patterns in the basin.

Chapter 2
Mapping leaf area index using spatial, spectral, and temporal information from multiple sensors

2.1 Introduction

Terrestrial vegetation plays a critical role in regulating the exchange of energy and mass between ecosystems and the atmosphere. Radiation absorption, evapotranspiration and carbon exchange are among the most important biophysical processes that strongly depend on vegetation structure. Process-based models are increasingly being used to understand ecosystem dynamics in response to changing environmental drivers such as climate change and land-cover/land-use change. Simulation results from these models are highly dependent on the accuracy of landscape biophysical parameters, particularly those related to vegetation structure and distribution. Leaf area index (LAI) is perhaps the most important biophysical variable characterizing vegetation abundance and distribution across the landscape. Thus, ecosystem process models are very sensitive to its parameterization (Running et al., 1989; Bonan, 1993; Nemani et al., 1993; Running and Hunt, 1993). LAI is typically taken to be the total one-sided leaf area per unit ground area (Chen and Black, 1992), but nonrandom foliage distribution (clumping) makes measuring this quantity directly difficult because most optically-based measurement methods rely on the assumption that foliage is randomly distributed in the canopy. Instead, effective LAI (L_e, the product of LAI and the clumping coefficient) is often estimated and converted to LAI as necessary with independently estimated clumping information (Chen, 1996; Chen et al., 2003). Remote sensing provides the only viable option for mapping LAI continuously over the landscape. Therefore, mapping LAI using remotely sensed data has been a major objective in remote sensing application (Running et al., 1986; Spanner et al., 1994; Chen and Cihlar, 1996; Myneni et al., 2002; Colombo et al., 2003; Soudani et al., 2006; Song

and Dickinson, 2008).

Numerous algorithms have been developed in the literature for mapping LAI using remotely sensed data. One such approach is the inversion of canopy reflectance models (e.g., Myneni et al. (1997); Knyazikhin et al. (1998); Peddle et al. (2004)). Inversion methods have a number of attractive qualities such as a firm physical foundation and the ability to apply them across large spatial scales since they are not generally restricted to a single biome type. However, they are often difficult to parameterize and may be mathematically ill-posed (i.e., solutions may not be unique). Another approach is based on empirically developed models, which are perhaps the most commonly employed methodology (Peterson et al., 1987; Spanner et al., 1990; Chen and Cihlar, 1996; Turner et al., 1999). Most empirical approaches relate ground-based LAI to remotely sensed spectral vegetation indices (SVI) and use the site-specific, empirical relationship to map LAI for the spatial extent over which the model was developed. This approach has been successful, but has serious limitations. The most significant limitation is the tendency of SVI to lose sensitivity, or "saturate", at high to moderate levels of LAI (Baret and Guyot, 1991). Furthermore, there are a wide variety of such LAI/SVI relationships in the literature and little guidance exists about which SVI is most appropriate for LAI estimation, and which form the empirical relationship should take. Additionally, the product of such investigations usually lacks temporal dimension and represents LAI at a single "snap-shot" in time.

The tendency for SVI to saturate at moderately high LAI (LAI>3) is one of the major limitations for modeling of LAI using spectral information (Gower et al., 1999; Turner et al., 1999). One potential method of overcoming this limitation is to use additional information from remotely sensed imagery as predictors in the empirical model, particularly information from the spatial domain such as image texture (Wulder et al., 1998). There are many measurements to quantify image spatial information. Geostatistical parameters of image semivariograms and first-order texture measures, such as local variance, provide information on the vegetation content in the scene (Curran, 1988; Woodcock et al., 1988), and have been used to estimate vegetation structural parameters such as crown diameter (Cohen et al., 1990; Bruniquel-Pinel and Gastellu-Etchegorry, 1998; Song and Woodcock, 2003), stocking density (St-Onge and

Cavayas, 1995), successional trajectories (Song and Woodcock, 2002), LAI (Song and Dickinson, 2008), and to improve classification accuracy (Ferro and Warner, 2002; Warner and Steinmaus, 2005). Second-order texture measures are another method of measuring spatial information and can be derived from the grey level co-occurrence matrix (GLCM) (Haralick et al., 1973; Haralick, 1979; Baraldi and Parmiggiani, 1995). GLCM features have been used to increase classification accuracy (Franklin and Peddle, 1989; Carr and de Miranda, 1998; Franklin et al., 2000, 2001; Puissant et al., 2005), and to estimate forest structural attributes (Kayitakire et al., 2006). Texture measures improve the performance of empirical LAI models by contributing forest structural information (e.g. stem density, crown diameter, and crown closure). For example, Wulder et al. (1996) found that including texture variables as a complimentary predictor along with NDVI improved the correlation between observed and modeled LAI values in pine and aspen stands. Wulder et al. (1998) observed a 20% increase in model performance when multiple texture variables were used in addition to NDVI for predicting LAI in deciduous stands. They argued that texture variables are a better predictor of LAI in spectrally heterogeneous stands than vegetation indices. Colombo et al. (2003) also found a significant improvement in empirical LAI prediction across diverse cover types when texture metrics were included with vegetation indices. In that study, the improved performance resulted from the texture variables distinguishing between vegetation types rather than contributing stand structural information. It is clear from these results that texture measures include information about structural attributes of forest stands that can improve estimates of LAI. However, the precise nature of this structural information is difficult to ascertain since a particular texture is the result of many phenomenon including crown diameter, stocking density, the size and distribution of canopy gaps, and illumination/view geometry. Nevertheless, we might expect the relationship of LAI with texture to follow from changes in forest structure as a stand matures. For example, the texture of a forest canopy could be expected to become smoother as a young sparse stand matures into an even-aged, closed canopy, but then become rougher with further stand development due to increased canopy gaps and an increasingly uneven age and height distribution. Thus, we should expect rough textures to be associated with higher leaf areas in stands maturing beyond a closed canopy, even aged

condition, whereas smoother textures would be associated with higher leaf areas as a stand develops from a field condition towards a closed canopy.

An additional challenge results from the tradeoff between spatial and temporal resolutions that is necessary due to the physical and technological limitations of remote sensing systems. Sensor systems that have the spatial resolution required for local and regional-scale studies typically lack the temporal resolution required to produce maps for the evolution of vegetation through a growing season, especially considering that cloud-cover may significantly reduce the actual number of usable images in any one year. This difficulty has motivated the exploration of various image fusion techniques to combine desirable image characteristics across multiple sensors and spatial resolutions. Some examples of these techniques include HSV transforms (Carper et al., 1990) and wavelet decompositions (Yocky, 1996; Nunez et al., 1999). These techniques have focused on enhancing the spatial resolution of multispectral imagery with panchromatic images ("pan-sharpening"), but they introduce spectral distortions which limits their application to studies which require rigorous estimates of surface reflectance or spectral radiance (Chavez et al., 1991; Hilker et al., 2009). Gao et al. (2006) attempted to overcome this limitation by developing the STARFM algorithm to generate synthetic Landsat images using MODIS and Landsat image pairs. Hilker et al. (2009) used STARFM to investigate phenological patterns in British Columbia and found that the predicted and observed Landsat reflectance values were well correlated. However, the effectiveness of the STARFM algorithm is strongly dependent on the number of homogeneous coarse-resolution pixels in the study-area, significantly limiting its application to highly heterogeneous areas such as suburban and urban landscapes. Creating synthetic imagery is not the only way to combine complimentary information from multiple sensors. Instead, multiple phenomena may be investigated independently with imagery having spatial, spectral and temporal resolutions commensurate with the process under investigation and the resulting information combined to investigate a more complicated phenomenon for which no single data source had optimum resolutions.

The goal of this study was to develop an algorithm to produce L_e maps with both high temporal and spatial resolutions, capturing both its heterogeneity in space and its variation in time, which are essential inputs for process-based ecosystem models. To accomplish this goal,

we developed a model to map L_e which combines complimentary spatial, spectral and temporal information from IKONOS, Landsat and MODIS remotely sensed imagery, respectively. We chose to estimate L_e rather than LAI because it is determined solely by radiation interaction with the canopy, and therefore comports better with both the remote sensing perspective, and indirect field-based measurement techniques. The model was able to generate daily maps of L_e at Landsat spatial resolution for a study site in North Carolina.

2.2 Methods

2.2.1 Study Area

We took the 10x10 km extent of an IKONOS image centered on the Blackwoods Division of Duke Forest (35° 58′ 25″ N, 79° 5′ 35″ W) as the study area for this investigation (Fig. 2.1). The Blackwoods Division of Duke Forest is an approximately 1000 ha research forest near Chapel Hill in Orange County, North Carolina. Forests are a well partitioned mix of pine and hardwood stands on acidic clay-loam soils. Loblolly pine (*Pinus taeda*) is the dominant evergreen species but shortleaf and Virginia pines (*Pinus echinata* and *Pinus virginiana*, resp.) are also common. Hardwood species include white oak (*Quercus alba*), post oak (*Quercus stellata*), blackjack oak (*Quercus marilandica*), mockernut and pignut hickory (*Carya tomentosa* and *Carya glabra*), sweetgum (*Liquidambar styraciflua*), and tulip poplar (*Liriodendron tulipifera*) in the overstorey, with red maple (*Acer rubrum*), flowering dogwood (*Cornus florida*), and redbud (*Cercis canadensis*) commonly found in the understorey. Hardwood stands exhibit a mixed age distribution with some individuals in excess of 200 years old. Though some unmanaged pine stands are over 100 years old, the majority used in this study are much younger planted and managed stands of evenly aged individuals. July is the warmest month with average maximum temperatures reaching 32° C, and January is the coldest with average maximum temperatures of 11° C. Precipitation averages 1180 mm and is evenly distributed throughout the year.

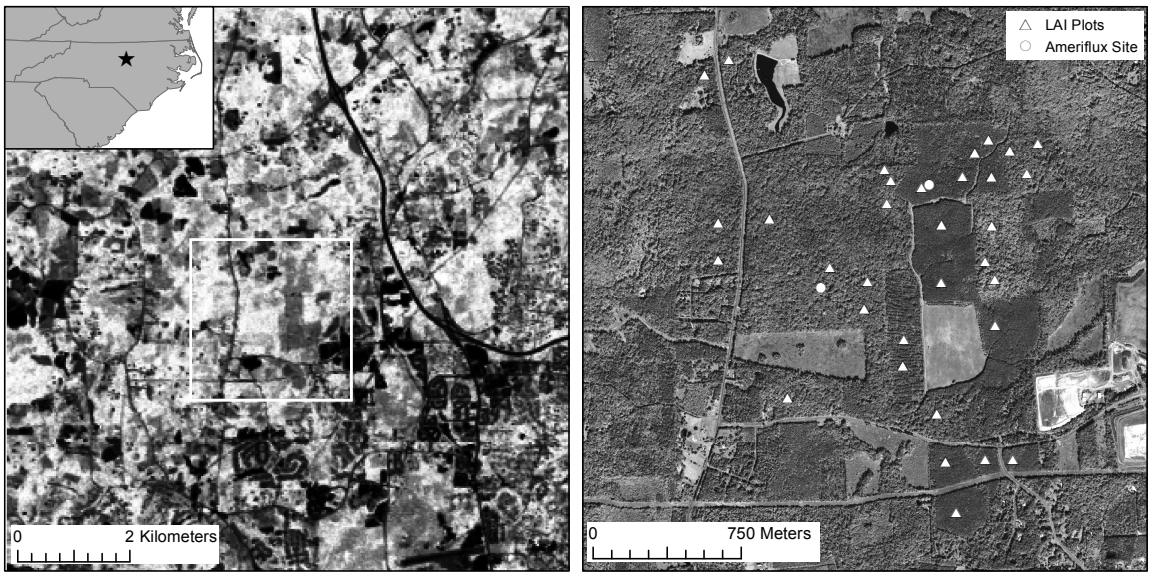

Figure 2.1: Left: May, 19 2009 Landsat TM NDVI image of study-area (10 km x 10 km extent of IKONOS image). Right: The Duke Forest research area where ground-observations of LAI were made. Sampling plots are shown on the panchromatic IKONOS image.

2.2.2 Ground L_e Measurement

There are two approaches to estimating LAI on the ground: direct and indirect (for a review of *in situ* LAI estimation see Breda (2003); Jonckheere et al. (2004); Weiss et al. (2004)). Direct approaches, such as destructive harvesting, typically result in a set of allometric equations which estimate LAI as a function of more easily observed quantities such as stem diameter. Though this methodology can produce very accurate estimates of LAI, it is much less efficient than indirect techniques. Indirect approaches use optical instruments and Beer's law of radiation attenuation to predict L_e under certain assumptions about the spatial distribution and orientation of leaves in the canopy (Norman and Welles, 1983). We used a pair of LAI-2000 Plant Canopy Analyzers (Li-cor, Lincoln, Nebraska) (Welles and Norman, 1991) to estimate L_e in 33 stands within the Blackwoods Division of Duke Forest in June and July of 2008 and 2009 (Fig. 2.1). The devices were deployed in paired operating mode with one unit collecting out of canopy radiation measurements in a large, open field and the other device collecting below canopy measurements. Observations were conducted at dawn or dusk under diffuse

lighting conditions. The footprint of such measurements depends on the height of the canopy. In our case, the footprint of the field observations are circles with radii ranging from 20 to 70 meters. FV2000 software (Li-Cor, Lincoln, Nebraska) was used to merge the datasets and convert above and below canopy radiation measurements to L_e estimates. The device was configured to average four individual below canopy measurements (taken facing the cardinal directions) to estimate plot L_e. The LAI-2000 instrument utilizes an optical sensor which simultaneously records radiation in five concentric zenith rings. Chen et al. (2006) argues that estimates may suffer from a multiple scattering effect that is greatest at the largest zenith angles, and therefore recommends calculating L_e estimates neglecting the fifth and/or fourth sensor ring. We investigated this multiple scattering effect by estimating L_e with all five sensor rings and excluding the fifth ring.

2.2.3 Model Overview

The central idea of our approach is to use a phenological function to track the variation of L_e between minimum and maximum values for individual pixels, similar to the approach taken by the ECOCLIMAP project (Masson et al., 2003), but at a much higher spatial resolution. The temporal component of the L_e trajectory is separate from the spatial and spectral components, and therefore the two phenomena may be modeled independently with data appropriate for each. Equation 2.1 shows how the L_e of a single pixel may be determined as a function of time (t) by adding to the pixel's minimum L_e an increment of the total annual L_e amplitude determined by a phenological function $f(t)$ that indicates the relative position along a phenological trajectory. At peak L_e $f(t) \rightarrow 1$ and L_e is equal to its maximum value, whereas during the dormant period $f(t) \rightarrow 0$ and L_e is at its minimum.

$$L_e(t) = \min(L_e) + f(t)\,[\max(L_e) - \min(L_e)] \tag{2.1}$$

Separate empirical models for evergreen and deciduous forest types were developed based on ground observations using a combination of spectral and spatial information from Landsat and IKONOS imagery to generate a map of maximum L_e (Eq. 2.2). It should be noted that Eq. 2.1

is a special case of a simple linear equation with the coefficient equal to $\max(L_e) - \min(L_e)$, and the intercept equal to $\min(L_e)$. As such, the model could be expressed generically and solved for arbitrary dates during the growing season. However, the majority of field observations are obtained during the peak of the growing season, and errors in the estimation of the coefficient are minimized when the difference in L_e is greatest, making the stated form of the equation the most relevant realization.

$$\max(L_e) = \beta_0 + \beta_1 \mathrm{SVI}_1 + \beta_2 \mathrm{SVI}_2 + \beta_3 \mathrm{TEX} \tag{2.2}$$

Where $\mathrm{SVI}_{1,2}$ and TEX are spectral and textural predictors, respectively, and β_i are empirical coefficients determined from linear regression. Minimum L_e is mapped by assuming that deciduous vegetation will be absent during the dormant season (L_e=0), and evergreen L_e will fall to about one-half of its maximum value, based on the findings of McCarthy et al. (2007) that showed the mean ratio of annual maximum to annual minimum LAI was 1.8 for loblolly pine stands in our study area. Pure deciduous or evergreen pixels are rare in this study area and so we treat each pixel as having some contribution from both vegetation types. A deciduousness parameter, ω, is calculated for each pixel from the normalized difference of winter and summer NDVI (Eq. 2.3). After linear scaling between zero and one, this deciduousness parameter is taken to represent the sub-pixel fraction of deciduous vegetation. This parameter is then used in Eq. 2.4 to mix the L_e contributions from evergreen, L_{ep}, and deciduous, L_{ed}, vegetation in each pixel.

$$\omega = \frac{\mathrm{NDVI}_{summer} - \mathrm{NDVI}_{winter}}{\mathrm{NDVI}_{summer} + \mathrm{NDVI}_{winter}} \tag{2.3}$$

$$L_e = (1 - \omega) L_{ep} + \omega L_{ed} \tag{2.4}$$

The phenological function, $f(t)$, is determined by fitting a nonlinear model (Eq. 2.5) to a time series of MODIS NDVI. These estimates are then transformed via a simple linear scaling to values between zero and one to be used as phenological coefficients in the composite model

(Eq. 2.6).

$$\text{MODSVI}(t) = \left(\frac{1}{1 + e^{a-bt}} - \frac{1}{1 + e^{a'-b't}} \right) g + h \tag{2.5}$$

$$f(t) = \frac{\text{MODSVI}(t)}{\text{MODSVI}_{\text{max}} - \text{MODSVI}_{\text{min}}} \tag{2.6}$$

Where MODSVI, $\text{MODSVI}_{\text{max}}$, and $\text{MODSVI}_{\text{min}}$ are MODIS NDVI and its corresponding minimum and maximum value within a year for a pixel, and a, b, a', b', g, and h are empirical parameters.

2.2.4 Spatial & Spectral Information: Texture and SVI

A single Landsat TM image (path 16, row 35, collection date: May 19, 2009) was used to calculate the SVI used as predictors in the empirical modeling effort. This image was selected because it was the cloud free image closest in time to the field data collection. Texture measures were calculated on a panchromatic IKONOS image (collection date: September 24, 2004), which was the only available image from this sensor covering the entire study area. Although there is a lag in time between the IKONOS image and the Landsat image, we believe that the texture information should still be helpful in overcoming the problem of spectral signal saturation. The TM image was orthorectified to the IKONOS image and atmospherically corrected using a dark object subtraction technique with downwelling diffuse radiation modeled using the 6S radiative transfer code (Song et al., 2001).

There is little agreement in the literature about which SVI are best suited for estimating LAI. For this reason we chose to calculate a suite of commonly used indices and used a model selection procedure to determine the most explanatory model. We calculated a variety of SVI, including the simple ratio (SR), reduced simple ratio (RSR), normalized difference vegetation index (NDVI), normalized difference water index (NDWI), enhanced vegetation index (EVI) and the structural index (SI) (Table 2.1). Homogeneous areas surrounding the study plots were selected and used to obtain a single average value of each SVI for each study plot. These areas varied in size depending on the heterogeneity of the forest stand surrounding the study

plots, but were 90 m by 90 m on average, and were non-overlapping.

First-order texture metrics such as windowed variance and second-order metrics such as GLCM features have been used successfully to estimate forest structural attributes (see Section 2.1). However, second-order metrics require extensive parameterization. To calculate GLCM features, it is first necessary to determine the appropriate window-size, grey-level quantization and offset distance and direction (Haralick et al., 1973). It is also necessary to determine which subset of the many GLCM features will be used for prediction. In comparison, first-order metrics require only the selection of the optimum window-size, and the full gamut of image grey-levels may be used without incurring significant computational penalties. For these reasons, we chose to use windowed variance as the only texture predictor in the L_e estimation effort. We calculated image semivariograms on samples from the IKONOS panchromatic image that were representative of the deciduous and evergreen plots measured on the ground. The range of these semivariograms indicates the characteristic spatial scale of the pattern, or the distance at which ground objects are no longer related. We chose to use the maximum range (13 meters, and 13 pixels) among the image samples as the geographic window size for calculating the variance across the entire image. This approach follows the recommendations by Franklin et al. (1996) for determining optimum geographic windows with empirical semivariograms. The same homogeneous areas surrounding the study plots used for averaging SVI were used to average the variance values resulting in a single texture predictor for each plot.

Name	Abbv.	Formula	Citation
Simple Ratio	SR	$\frac{\rho_{\text{nir}}}{\rho_{\text{red}}}$	Jordan (1969)
Reduced Simple Ratio	RSR[a]	$\frac{\rho_{\text{nir}}}{\rho_{\text{red}}} \cdot \left[1 - \frac{\rho_{\text{swir}} - \rho_{\text{swir}}^{\text{min}}}{\rho_{\text{swir}}^{\text{max}} - \rho_{\text{swir}}^{\text{min}}}\right]$	Brown et al. (2000)
Norm. Diff. Vegetation Index	NDVI	$\frac{\rho_{\text{nir}} - \rho_{\text{red}}}{\rho_{\text{nir}} + \rho_{\text{red}}}$	Rouse et al. (1973)
Norm. Diff. Water Index	NDWI[b]	$\frac{\rho_{\text{nir1}} - \rho_{\text{nir2}}}{\rho_{\text{nir1}} + \rho_{\text{nir2}}}$	Gao (1996)
Enhanced Vegetation Index	EVI[c]	$G\frac{\rho_{\text{nir}} - \rho_{\text{red}}}{\rho_{\text{nir}} + C_1\rho_{\text{red}} - C_2\rho_{\text{blue}} + L}$	Huete et al. (1999)
Structural Index	SI	$\frac{\rho_4}{\rho_5}$	Fiorella and Ripple (1993)

[a] $\rho_{\text{swir}}^{\text{min}}$ and $\rho_{\text{swir}}^{\text{max}}$ are the scene min and max SWIR reflectance

[b] Gao (1996) specifies ρ_{nir1} and ρ_{nir2} as two spectral channels centered at 0.86 μm and 1.24 μm, respectively. Lacking a Landsat band fitting this definition for ρ_{nir2}, we substitute band 5, the SWIR channel.

[c] The coefficients adopted in the MODIS-EVI algorithm are; $L = 1, C_1 = 6, C_2 = 7.5$, and $G = 2.5$

Table 2.1: Formulae for spectral vegetation indices used in this investigation. Reflectances, ρ, are specified in a sensor independent manner based on their original specification. We take Landsat bands 1, 3, 4, and 5 as blue, red, nir, and swir, respectively.

2.2.5 Temporal Information: Phenology

Tracking the onset and duration of phenological events has long been investigated using remotely sensed imagery. Approaches usually rely on fitting a nonlinear model to a set of indicator variables, such as spectral vegetation indices (Jonsson and Eklundh, 2002). Phenological events occur quite rapidly in vegetation communities like the ones in our study area. Obtaining a temporally dense time series of images is essential for successful model fitting. Though the spatial resolution of Landsat imagery is appealing for regional and local-scale investigations, its revisit time is too infrequent to ensure reliably cloud-free images at an acceptable interval. Instead we used the MODIS 16-day composite SVI products for fitting the phenological model.

We obtained a growing season length time series of MODIS NDVI at 250 m spatial resolution (MOD13Q1 product) and used the accompanying metadata to restrict pixels to only the most reliable observations. The 500 m MODIS land-cover product (MCD12Q1) was used to further segregate the pixels into deciduous and evergreen pixels using the IGBP biome definitions of that product. A daily time series of average, high-quality NDVI observations for each cover type was constructed by averaging the NDVI value of all pixels having the appropriate day of year as indicated by the composite day of year image included in the MOD13Q1 product. This is essentially "decompositing" the 16-day MOD13Q1 product using the composite day of year. Further filtering of values was necessary to remove outliers. We used a 16-day moving window on the time series and flagged as outliers values which either exceeded the third quartile maximum by more than 1.5 times the interquartile range, or were below the first quartile minimum by 1.5 times the interquartile range or more (Tukey definition). Averages calculated using fewer than 20 pixels were also excluded. Equation 2.5 (Fischer, 1994; Zhang et al., 2003; Fisher et al., 2006) was fit to the refined time series using weighted nonlinear least squares regression techniques. Weighted regression was used because each estimate of daily mean NDVI is computed from a potentially different number of observations and the variances of the observations are therefore not necessarily equal. Weighting each observation by the reciprocal of the measurement's variance leads to unbiased estimates.

2.2.6 Empirical Model Selection

There are a wide variety of published empirical LAI models taking a variety of mathematical forms. Most use a single SVI as a predictor and thus neglect potential complimentary information from other sensors (Fassnacht et al., 1997). Also, multiple competing models are generally not considered, or the selection procedure is not rigorous. In this investigation, we relied on a model selection procedure based on information theoretic criteria to compare multiple models (Burnham and Anderson, 2002). In this procedure a portfolio of candidate models are proposed, fit to the data, and then ranked according to the Akaike information criterion (AIC), a relative measure of the goodness of fit of a model which allows for comparisons between models with varying numbers of parameters. Multiple regression with two complimentary SVI predictors and one, or no texture predictors (Eq. 2.2) was used to model the ground observed L_e. Initial exploratory analysis indicated that one of either SR or RSR as the first SVI predictor and SI or EVI as the second SVI predictor best explained the field observations. Thus, we proposed eight candidate models (four different models using only SVI predictors, and the same four models with the addition of the texture variable), fit them to the data, and ranked them according to the AIC selection procedure. The best among this portfolio of models was selected as the empirical relation to map maximum L_e.

2.3 Results

2.3.1 Spatial & Spectral L_e Model

A comparison of L_e estimates obtained by excluding the fifth sensor ring reveals the same pattern found by Chen et al. (2006), i.e. an increase in estimated L_e when the highest zenith angle ring was excluded (Fig. 2.2). This indicates either multiple scattering, which violates the assumption of opaque leaves at blue wavelengths (a critical assumption of the LAI-2000 instrument), or stand-level clumping leading to a violation of the assumption of randomly distributed foliage. As a result, we used the estimates obtained by excluding the fifth sensor ring as the L_e estimates for subsequent modeling.

Model	Parameters										AICc	AIC Wt	R^2
	SR_c	SR_d	RSR_c	RSR_d	EVI_c	EVI_d	SI_c	SI_d	VAR_c	VAR_d			
SEV	1.0e1***	2.9$^{\cdot}$	-	-	-1.0e2***	-4.8e1*	-	-	-1.6e-5	1.1e-4**	87.4	0.71	0.73
REV	-	-	5.2***	1.7	-3.0e1*	-1.8e1*	-	-	-3.2e-5	9.6e-5**	90.0	0.20	0.71
SE	1.0e1***	4.3e-1	-	-	-1.0e2***	-8.3	-	-	-	-	92.5	0.05	0.61
RE	-	-	5.1***	2.0e-1	-3.4e1*	-3.7	-	-	-	-	93.7	0.03	0.59
RS	-	-	1.3	4.8e-1	-	-	3.7	0.7	-	-	100.4	<0.01	0.50
RSV	-	-	3.3	-1.8e-1	-	-	8.3e-1	-2.2	-5.5e-5	6.0e-5	101.1	<0.01	0.59
SSV	-1.2e-1	-4.6e-1	-	-	-	-	7.4**	2.4e-1	-3.6e-5	6.8e-5$^{\cdot}$	101.5	<0.01	0.59
SS	1.7***	2.0e-1$^{\cdot}$	-	-	-	-	8.3e-1**	-6.2e-2	-	-	189.8	<0.01	0.33

Table 2.2: Candidate models ranked by AIC with finite sample size correction (AICc) and associated parameter estimates. All models have effective LAI (L_e) as the dependent variable. Model names are abbreviations which indicate the predictor variables included (e.g. "SEV" include the Simple Ratio (S), Enhanced Vegetation Index (E), and Variance (V)). Refer to Table 2.1 for SVI formulae. Subscripts, c and d, designate the parameter estimate for conifer and deciduous plots, respectively. "VAR" refers to the windowed variance measure of texture. Sig: ***: <0.001, **: <0.01, *: <0.05, ˙: <0.1

The overall best model included SR and EVI as SVI predictors along with the texture variable (local variance) and explained 73% of the observed variability in the ground data (Table 2.2). The second best model replaced SR with RSR and achieved an R^2 of 0.71. Both of the best models had residual standard errors of 0.7. The two best models included texture as a predictor and explained significantly more variability than the best models which did not include a texture predictor. Figure 2.3 shows that texture offered the greatest improvement to deciduous L_e prediction and accounted for more variability within these stands than any other predictor. Deciduous L_e was positively correlated with image texture in all models that included it as a predictor. In evergreen stands L_e was positively correlated with SR and RSR and there was no significant correlation with texture variables. There were significant negative correlations with EVI among both evergreen and deciduous models for the two best models. The AIC weight indicates the relative likelihood of each candidate model and may be used for multi-model averaging when there are multiple competing models. In this case, the best model has a much higher likelihood than the next best model and we therefore choose it for mapping maximum L_e across the entire study area.

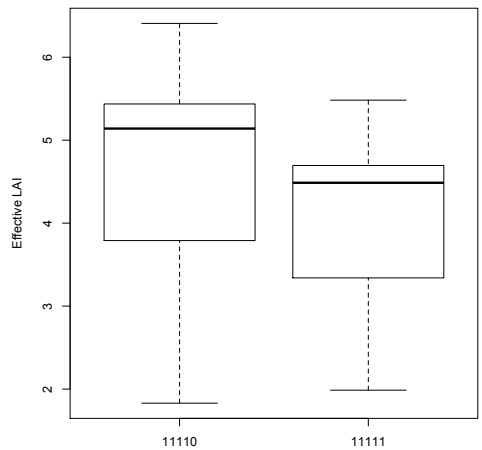

Figure 2.2: Comparison of L_e estimates, 11111: all five sensor rings used, 11110: first four sensor rings used.

2.3.2 Phenology

Table 2.3 provides the parameter values estimated via weighted nonlinear least squares regression. There were no significant differences between parameter values for deciduous and evergreen models. For this reason we selected the deciduous model as $f(t)$ in Eq. 2.1 and neglect the evergreen model. Figure 2.4 shows the data used for the fitting procedure, the identified outliers, and the weights assigned to each observation. It was determined that removal of outliers and observations averaged from less than 20 pixels was necessary in order to obtain stable parameter estimates in an automated fashion. It should be noted that this is the

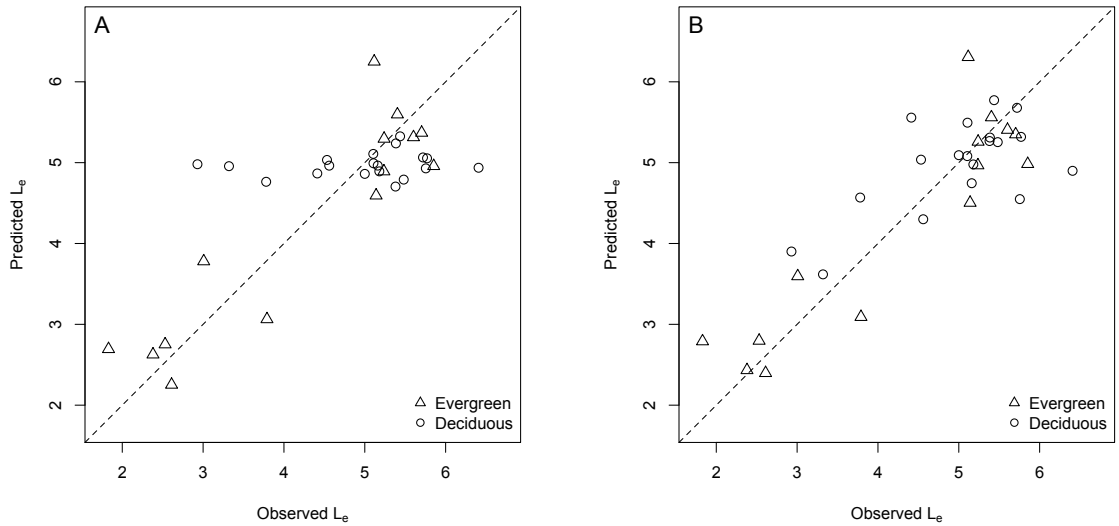

Figure 2.3: Comparison of observed and predicted L_e using models SE (A) and SEV (B). Model SEV contains a texture estimator which leads to a significant improvement in model fit for deciduous stands.

variability that remains after the initial restriction to pixels identified by the MODIS algorithm as being "good data". If these outliers and high variance estimates are not removed, there is too much variance for the nonlinear least squares procedure and extensive user adjustment of initial parameter values is required. In order to use the phenological information in the composite model we must adjust the model from one that predicts NDVI as a function of day of the year to one that yields a coefficient between zero and one indicating the relative position along the phenological trajectory (Eq. 2.5 vs. Eq. 2.6). This is accomplished by calculating the expected NDVI for each day in the growing season with the phenological model and then linearly scaling these values between zero and one.

2.3.3 Modeled L_e

The empirical L_e model identified as best through the model selection procedure was used to generate a single map of max(L_e). The deciduousness parameter, ω, was calculated according to Eq. 2.3 for every forested pixel within the study area using the summer Landsat TM image and a winter image (collection date: January 25, 2008, there were no cloud free images of the study area available in 2009). Equation 2.4 was then used to calculate maximum L_e for

	Deciduous		Conifer	
Parameter	Estimate	Std. Error	Estimate	Std. Error
a	18.61***	3.38	16.29***	3.76
b	0.166***	0.030	0.144***	0.033
a'	15.16***	1.47	16.62***	1.97
b'	0.049***	0.005	0.054***	0.007
g	0.292***	0.008	0.299***	0.010
f	0.516***	0.006	0.512***	0.008

Table 2.3: Weighted nonlinear least squares estimates of parameter values for Eq. 2.5. Sig: ***: <0.001

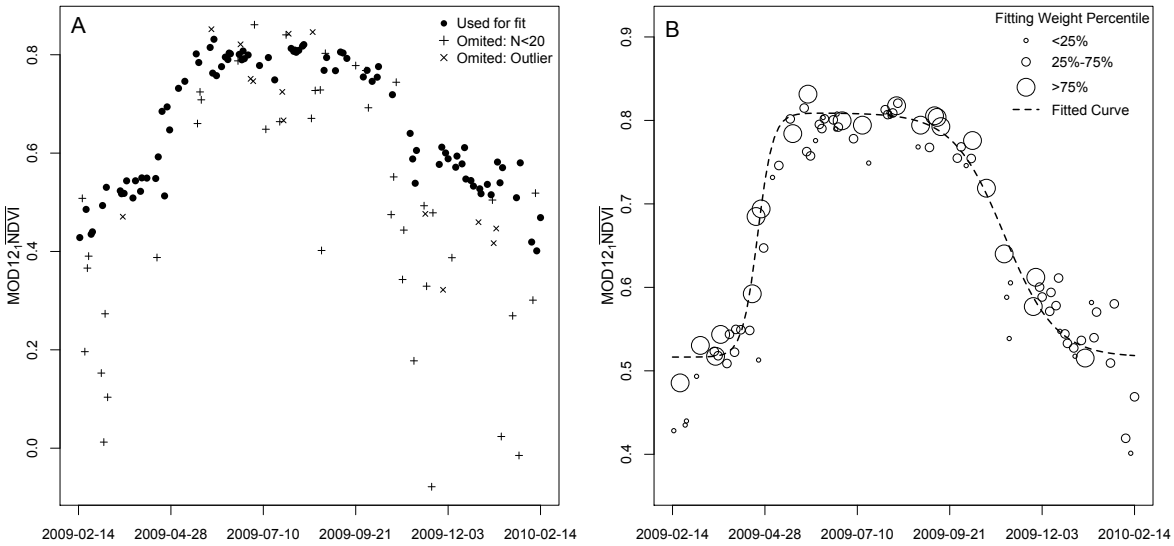

Figure 2.4: Mean NDVI for MOD12Q1 Type 1 Deciduous forests indicating points omitted from fitting procedure by outlier detection or too few pixels used in calculation (A), and the full range of just the data used for fitting (B). Point sizes indicate the relative weight used in the nonlinear least squares fit. Dashed line is fit. Note that the figures have different scales.

each pixel by weighted mixing of estimated L_e contributions according to the deciduous or evergreen model. Minimum L_e was determined using this same equation and the previously stated assumptions regarding minimum L_e among cover types. Thus, the model was fully determined and used to generate daily maps of L_e for forested pixels within the study area. We lacked ground observations of L_e for non-forested plots and were thus unable to produce an empirical relationship for these cover types. However, LAI is typically low in non-forest vegetation, thus spectral signal saturation is much less of a problem. For these areas we used the best L_e model based only on SVI.

Validation of a product such as this is complicated by the lack of time series of LAI or L_e estimates across many sites. However, two AmeriFlux sites within our study area (Fig. 2.1) provide these data for a single deciduous and evergreen stand. The temporal dynamics of pine LAI were reconstructed using data on leaf litterfall mass and timing, specific leaf area, leaf elongation rates, and fascicle, and shoot counts (McCarthy et al., 2007). Hardwood LAI was estimated using conventional litterfall techniques (Oishi et al., 2008). We used these data for a plot level comparison of LAI estimates for a single year. We performed an additional, coarser scale, evaluation of the model utilizing the MODIS LAI product (MCD15A2) for the 2009 calendar year. This product is produced at an 8-day interval and a 1x1 km pixel size. The main MODIS LAI algorithm relies on a lookup table generated from a radiative transfer model. A backup algorithm based on biome specific empirical equations and SVI is used when the main algorithm fails (Knyazikhin et al., 1999). We chose to directly compare our L_e estimates with AmeriFlux and MODIS LAI estimates because measurements (our own unpublished data) have shown that there is only minor clumping in the closed canopy forests in our study area, and thus the differences are likely small. Figure 2.5 compares our modeled L_e with the AmeriFlux LAI at the evergreen and deciduous site. Our modeled estimates of evergreen maximum and minimum L_e agree very well with the AmeriFlux estimates, and the onset and duration of the green-up and senescence period are also predicted well. Our model predicts a deciduous maximum L_e that is one unit smaller than the AmeriFlux LAI estimate, but captures the start and duration of the green-up period well. The lower peak L_e predicted by the model may be due to a minor effect of leaf clumping in the canopy. Our model predicts a

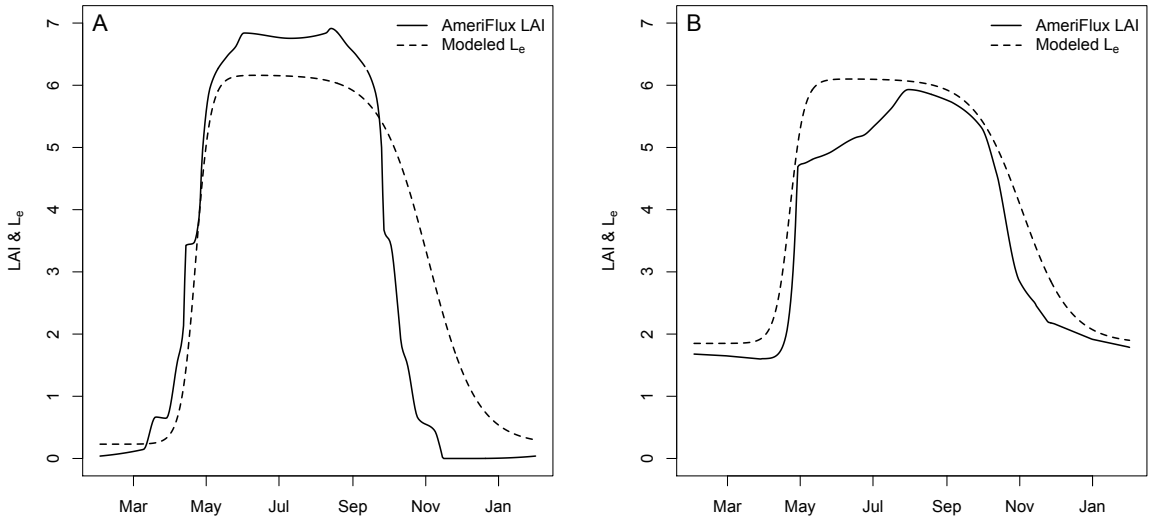

Figure 2.5: Daily estimates of L_e using our model compared to AmeriFlux daily estimates of LAI at a deciduous (A) and evergreen (B) site within the study area. AmeriFlux estimates represent canopy LAI, the sum of deciduous and evergreen LAI contributions within each site. For example, though the evergreen site is primarily *P. taeda* there are small LAI contributions from various deciduous understorey species. These data are reconstructed from litterfall collection as described by McCarthy et al. (2007)

prolonged senescence period compared to the reconstructed AmeriFlux LAI for the deciduous stand. This is because the phenological model is based on 250x250 m MODIS SVI and 500x500 m MODIS land-cover, at which scales there are very few pure deciduous or evergreen pixels in the heterogeneous landscape of our study area. This problem would probably be ameliorated for larger study areas with a more homogeneous land-cover composition.

We resampled our L_e surfaces to MODIS spatial resolution (1x1 km pixels) and compared our annual L_e pattern to time series of MODIS LAI estimates for spatially coincident pixels. The single 1x1 km resampled pixel centered on the Blackwoods study site covered four 500 m spatial resolution MODIS land cover (MCD12Q1) pixels, 75% of which were classified as deciduous broadleaf forest and 25% were identified as evergreen needleleaf forest. We also chose a developed pixel where 75% of the pixel was classified as urban in the MCD12Q1 product, with the remainder being classified as forest. Figure 2.6 compares the MODIS LAI estimates with the resampled estimates from our model over a calendar year. The MODIS LAI/FPAR

quality control bitfield is displayed below the time series. Modeled maximum L_e agrees with the MODIS maximum LAI estimate and the green-up period characteristics are similar for both sets of estimates at the Blackwoods pixel. At the urban pixel, MODIS estimated maximum LAI exceeds our estimate by two units, and our modeled minimum is one unit lower than that estimated by the MODIS algorithm. At the urban pixel, the green-up and senescence periods are difficult to discern due to the high amount of variability in the estimates. This variability is common to both pixel's MODIS LAI trajectories, and is not fully explained by the QC flags. For instance, DOY 225 has an exceptionally low LAI estimate in both time series, but the QC flag at the Blackwoods site does not indicate any problems, whereas mixed clouds are indicated over the developed pixel. It can be seen that estimates produced with the backup MODIS LAI algorithm are generally lower than the main algorithm, but limiting analysis to only main algorithm estimates does not significantly reduce variability in the LAI trend, especially over the developed pixel. The unsteady temporal trend of MODIS LAI has been noted by other investigators and may be addressed using a variety of gap-filling and smoothing techniques Verger et al. (2008); Kobayashi et al. (2010); Verger et al. (2011).

2.4 Discussion

Our results support previous work indicating that texture measures generally improve empirical models of LAI in forests when compared to using SVI alone (Wulder et al., 1996, 1998; Song and Dickinson, 2008). It has been hypothesized that this improvement is due to the textural features containing forest structural information. Indeed, this line of reasoning is supported by studies which have shown relationships between image texture and structural variables such as canopy diameter and stocking density (St-Onge and Cavayas, 1995; Song and Woodcock, 2003; Song, 2007; Song and Dickinson, 2008). Others have argued that the improvement is due to the textural information providing a pseudo-classification of the image (Colombo et al., 2003), which is likely the case in study-sites with many diverse vegetation communities. Our results support the former hypothesis more strongly than the latter by showing the greatest improvement in modeling efficiency for a single land cover type (deciduous stands), although a

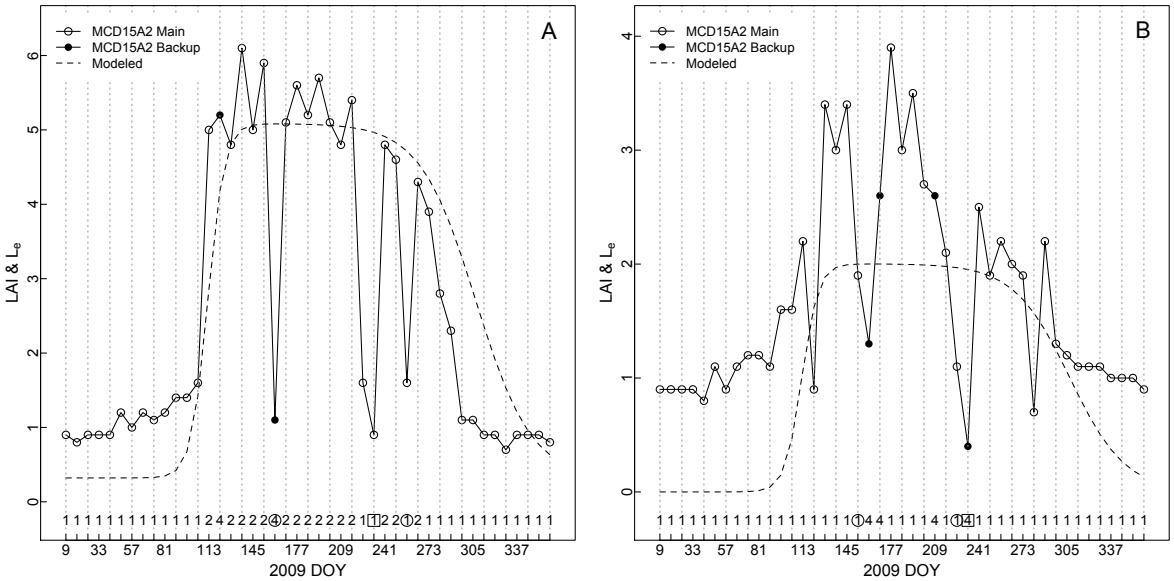

Figure 2.6: Comparison of estimated L_e and the MODIS LAI product (MCD15A2) for single MODIS pixels centered on the Blackwoods study site (A) and a mostly developed pixel (B) over the 2009 calendar year. Numbers underneath each MODIS LAI estimate correspond to the five level confidence score (1: best result possible, 2: main algorithm with saturation, 3: main algorithm failed due to bad geometry, 4: main algorithm failed due to problems other than bad geometry, and 5: pixel not produced at all). Symbols surrounding this quality score indicate the cloud state (squares indicate that significant clouds were present, and circles indicate that mixed clouds were present on the pixel).

direct comparison between these studies is complicated by the use of different texture metrics and vegetation types.

Wulder et al. (1998) showed the greatest improvement in LAI prediction with texture measures among evergreen stands, but our results showed an insignificant relationship in these stands. In contrast, texture was the single best predictor of deciduous L_e in this investigation. However, it is important to note that we used a single measure of texture and a single window-size to calculate this metric. While we believe we gain interpretability and simplicity with this approach, it is possible that different measures of image texture may contain complimentary information. For instance, the lack of a significant relationship between evergreen L_e and variance may be the result of a non-optimal window size for evergreen variance calculation. In fact, the deciduous crowns were much larger than the evergreens and a "one-size-fits-all" approach to variance calculation may have been inadequate. However, using multiple window sizes increases the reliance on image classification. The positive relationship between first-order image variance and L_e observed in this study may indicate that variance captures information about canopy complexity which may be reasoned to increase with LAI as canopies mature. We have also demonstrated that multiple SVI can provide complimentary information and that multiple candidate models may be rigorously compared using AIC based model selection procedures.

We found that extensive filtering of MODIS SVI was required in order to obtain stable parameter estimates to the proposed phenological model in an automated fashion. Even after restricting the data to pixels identified as reliable by the MOD13Q1 algorithm, there was still too much variability and the nonlinear least squares approach was unstable and sensitive to initial parameter estimates. We used a simple phenological model because it has been demonstrated to perform well for forested vegetation. It is inadequate, however, for multi-peak phenologies characteristic of multiple crop rotations, and an alternative model would be required if capturing such vegetation changes was important in a given study area. We observed that there was no significant difference between deciduous and evergreen phenological models. We believe that this results from heterogeneity in pixels assumed to be pure deciduous or evergreen. The MODIS land-cover product used for constructing the time series has a spatial

resolution of 500 m which is likely too large for a study area as small and heterogeneous as ours. It should be noted, however, that the same lack of difference in phenologies was found when a much more restrictive pixel selection procedure was employed. Using the NLCD land-cover product we attempted to identify MODIS resolution pixels with at least 80% homogeneity in NLCD land-cover definition. This resulted in far fewer pixels available for the calculation of daily NDVI averages and necessitated that the area considered for phenological signal extraction be much larger. However, the lack of difference between evergreen and deciduous phenology under this more restrictive pixel selection procedure does not rule out the possibility that landscape heterogeneity is the underlying cause. Rather, it most likely indicates that there are very few homogeneous stands, and there is confusion in the classified map. This hypothesis is supported by field observations of abundant deciduous herbaceous and woody understory species in stands which would appear to be pure evergreen from a satellite view. Another possible source of phenological error is geolocation errors in the MODIS product. However, the difficulty in finding pure MODIS pixels using a finer scale product such as the NLCD lends stronger support to the hypothesis that subpixel heterogeneity is the dominant factor.

It is important to note that by relying on NDVI time series to fit the function $f(t)$ there is an implicit assumption of linearity in the relationship between SVI and NDVI that is likely violated in some cases, particularly in densely vegetated pixels. However, whereas this leads to underestimation of LAI in simple linear empirical relationships, the most likely effect on our model is a seasonal trajectory which reaches peak L_e too early in the growing season. In reality, some very densely vegetated pixels may continue to accumulate leaf area throughout the summer. This could possibly be avoided by utilizing a conversion function to convert MODIS NDVI observations to LAI, or by using the MODIS LAI product directly to fit the phenological function. In our case, using MODIS LAI to fit $f(t)$ would have exacerbated the mixed pixel problem due to the coarser spatial resolution of that product in comparison to NDVI, and would not have permitted the decompositing process used to obtain a finer temporal resolution time series. Nevertheless, this is probably a viable option in areas with larger, more heterogeneous forested areas, and a smoothing approach such as the one employed

by Gao et al. (2008) would be useful in obtaining a reasonable time series from MODIS LAI estimates.

The lack of time series of LAI ground observations prevented a rigorous validation, but comparison of predicted L_e at the two sites where time series LAI data was available are encouraging. The green-up period and time to peak LAI was well predicted for both deciduous and evergreen sites. Peak LAI for deciduous was under predicted, but the magnitude of the error is within the limits that are generally accepted among other studies. The senescence pattern for the deciduous vegetation is not well matched by our model. This is most likely the result of contamination of the phenological signal due to pixel heterogeneity as previously discussed. At the MODIS scale, our modeled estimates compared favorably over the predominately deciduous Blackwoods pixel, but not as well over the urban pixel where MODIS maximum and minimum LAI exceeded our estimates by two and one unit, respectively. There is a large amount of variability in the single pixel time series of MODIS LAI estimates, and although this product is not intended to be used at the scale of an individual pixel, it has important implications for studies utilizing this product for fine spatial scale ecosystem simulations. Our algorithm does not rely on instantaneous surface reflectance for estimating L_e and therefore produces a much smoother temporal trend of L_e. This more realistic trend, along with the finer spatial resolution and greater flexibility in land-cover designation are the main advantages of our algorithm over the MODIS product for local to regional-scale ecosystem simulation applications.

The accuracy of L_e estimates produced with our algorithm are determined primarily by the accuracy of the maps of minimum and maximum L_e. To overcome the problem of signal saturation using spectral information alone, we included image texture information based on findings from other studies (Colombo et al., 2003; Song and Dickinson, 2008; Song et al., 2010). It appears that this method works, at least for deciduous vegetation. However, the use of texture measures introduces its own limitations such as increased computational and data requirements. Texture measures also increase the dependency on land-cover maps because they are significant predictors of L_e only in closed canopy forest stands. The dependence on a single phenological function introduces several limitations. First, the double logistic function

is only capable of fitting SVI time series with a single yearly maximum, making it unsuitable for fitting time series of agricultural areas with multiple rotations in a year. Second, we must rely on coarser spatial resolution SVI estimates from MODIS in order to achieve the necessary temporal resolution for time series construction. As previously discussed, the main limitation of this approach is that it is difficult to fit vegetation specific phenological models in areas with few land-cover patches that are homogeneous at the MODIS SVI spatial resolution. In this investigation, this was evident in the lack of significant difference in models fitted to evergreen and deciduous SVI time series, and the prolonged senescence period evident in the estimated L_e time series. An additional issue associated with this approach is that relatively coarse land cover schema (e.g. "deciduous" as opposed to "oak") obscure phenological differences between individual species. With our approach, a single phenology is prescribed for all deciduous species. However, since the coarse spatial resolution SVI represent the bulk contribution to greenness from all species, the effect is likely not severe except in extreme cases where there are strong sub-pixel species gradients. A more serious limitation of this approach is that a single, land cover specific phenology is prescribed for the entire study-area which results in an insensitivity to environmental gradients affecting phenology. However, our method is primarily aimed at improving vegetation representation at spatial scales where these differences are small; in larger study areas where this effect is not small, existing moderate to coarse resolution vegetation representations are likely adequate and finer scale representations would be computationally infeasible.

This investigation combined complimentary information from IKONOS, Landsat, and MODIS sensors across a wide range of spatial resolutions. Our approach to using images from multiple sensors at a variety of temporal and spatial resolutions might best be thought of as information fusion rather than image fusion. The distinguishing feature is that we have combined complimentary information from multiple images without resorting to the production of synthetic images. The main application of this technique in this study was the fusing of phenological information from temporally dense MODIS observations with vegetation pattern information from higher spatial resolution Landsat imagery. Our approach is applicable to all naturally vegetated landscapes, particularly forested areas with high LAI, but is not applicable

in landscapes dominated by agricultural crops with multiple rotations due to the phenological model used.

2.5 Conclusions

In this study, we developed an algorithm which takes complimentary information from multiple remote sensing sensors, IKONOS, Landsat, and MODIS, to produce L_e surfaces at high spatial and temporal resolutions. We used spatial information from IKONOS imagery, spectral information from Landsat imagery, and temporal information from time series of MODIS NDVI. The data fusion approach used in this study did not have the production of synthetic images as its goal, instead we extracted spatial, spectral, and temporal information from the appropriate sensors and used the information directly in our algorithm. The approach is capable of producing L_e maps at Landsat spatial resolution and an arbitrary temporal resolution. Our L_e map compares well with the LAI trajectories independently developed for two AmeriFlux sites within the study area. Although we implemented the algorithm for a 100 km^2 study area, the approach can be applied to any size study area for which the necessary imagery is available. Our approach is particularly appealing in areas with high forest coverage and high LAI where traditional approaches based only on spectral information suffer from signal saturation. However, our approach is not applicable to agricultural landscapes with complex crop rotations. The L_e maps generated using this approach would be suitable for local to regional scale ecosystem simulation studies requiring accurate representation of the spatial patterns of vegetation at fine temporal and spatial scales. Another application would be to use these maps to test the effects of spatial resolution in process models such as GCMs which typically use coarser spatial scale maps of vegetation. Future improvements to this model should explore other texture metrics (possibly multiscale), improve upon the phenological model to address the problem of pixel heterogeneity and complex crop rotations, and obtain the ground data necessary for a robust validation.

Chapter 3
Consistent classification of image time series with automatic adaptive signature generalization

3.1 Introduction

It is well understood that land cover plays an important role in regulating energy and mass exchanges between the terrestrial ecosystem and the atmosphere with important implications for biological and climatological cycles (Foley et al., 2005). Human-dominated land uses have played a central role in shaping the observed pattern of land cover change, and there are concerns about how increasingly anthropogenically dominated environments will be able to reliably supply ecosystem services such as clean water and carbon sequestration in the future (DeFries et al., 2004). Characterizing historic land cover patterns, and monitoring current conditions are therefore of critical importance to efforts to model Earth system processes, and has motivated many efforts to map these patterns using remotely sensed images (Franklin and Wulder, 2002). In fact, land cover mapping, broadly defined, is without a doubt the most common scientific application of remotely sensed data, which are uniquely well suited to the task. Notable global efforts include early work with AVHRR data (Defries and Townshend, 1994), and the operationally produced MODIS global land cover product (Friedl et al., 2002). With a few important exceptions, such as the National Land Cover Dataset (NLCD) generated for the conterminous United States (Vogelmann et al., 2001), there have been few large scale mappings of land cover at fine spatial resolution. Historically, this type of mapping activity has been out of reach due to the practical, financial, and computational challenges associated with constructing and processing large archives of images. Recent developments such as the opening of the Landsat archive and advances in large-scale distributed computing on massive datasets have relaxed these limitations. Therefore, there is growing interest in methods to efficiently

utilize these archives to gain understandings of land cover dynamics at unprecedented spatial and temporal scales.

The essential challenge to reliably characterizing patterns of land cover dynamics with remotely sensed images is accurately and consistently classifying time series of images, preferably in an automated fashion (Loveland et al., 2002; Rogan et al., 2008). Consistency among land cover maps is essential to mapping change and is achieved by minimizing semantic errors between classified maps at different times. This amounts to ensuring that class spectral signatures are adapted to image differences, but correspond to the same land cover class for supervised classification approaches. Image differences result from varying irradiance, illumination/view geometry, atmospheric effects, surface moisture conditions, and other physical scene changes such as phenological development. Accounting for these image differences in class spectral signatures, or signature generalization (Woodcock et al., 2001), is the main challenge to mapping image time series. Fundamentally, two options exist: adjust spectral signatures so they are matched to individual images, or adjust the images themselves so that a single set of signatures may be used across all image dates. The former is the approach taken in generating the NLCD and most ad hoc land cover mapping investigations, whereby a few image dates are classified independently with unique training data. Aside from the practical limitations involved with assembling the extensive reference data, this method can invite inconsistency in class definitions due to training set differences, but is capable of adapting signatures to substantial spectral differences between images. In contrast, generalizing a single set of class spectral signatures across time and space by enforcing radiometric consistency among images is known as "signature extension" (Minter, 1978) and is more amenable to an automated workflow as the only *a priori* information required is a single set of class spectral signatures.

Signature extension methods rely on either relative (e.g., Hall et al. (1991); Olthof et al. (2005)), or absolute image corrections (e.g, Song et al. (2001); Pax-Lenney et al. (2001)) to account for atmospheric, radiometric, and irradiance differences between images, and have been implemented for decades (Botkin et al., 1984). Most existing signature extension experiments have been limited by data availability to consideration of a few discrete time steps, limiting the utility of the approach in comparison to independent mapping. Therefore, given developments

in data availability and computational power, the impetus to develop signature extension methods has never been stronger (Woodcock et al., 2001). However, there are significant limitations to signature extension methods. First, not all atmospheric and view/illumination effects can be completely accounted for. Further, even if correction procedures were 100% successful in removing such effects, signature extension methods are incapable of accounting for actual changes in class spectral signatures associated with phenology, moisture status, or other scene changes. Likewise, relative image normalization assumes linear relationships between images which may not be valid when spectral differences associated with phenology or moisture differences are present. Thus, signature extension methods would not be expected to perform well when image pairs were out of season, or when the surface was wet at one image date but not the other. Thus, traditional signature extension is severely limited in its application to temporally irregular time series of images that result when cloud conditions or other factors limit image acquisitions.

These concerns motivated the development of a novel approach to spectral signature generalization which overcomes the limitations associated with signature extension while maintaining an automated workflow with limited reference data requirements. Importantly, the approach is able to derive consistent class spectral signatures which are adaptive to a wide range of image differences, not only atmospheric and irradiance effects, yet has no requirement for relative or absolute image correction procedures. The essential concept of our approach is that class signatures may be derived independently for each image date from locations that have stable land cover. This approach is a development and refinement of previously recognized concepts, such as combining band difference and classification maps to map stable/change locations, and deriving spectral signatures from stable sites (Pilon et al., 1988; Sader, 1995; Mertens and Lambin, 2000; Fortier et al., 2011). However, the potential of these methods to enable automatic signature generalization across image time series, particularly temporally irregular ones, has not been previously explored. The objective of this study was to develop such an approach and provide an assessment of its performance relative to existing signature extension methods under multiple conditions.

3.2 Methods

3.2.1 Automatic Adaptive Signature Generalization Overview

Figure 3.1 compares workflows for a traditional signature extension approach and the automatic adaptive signature generalization (AASG) method developed in this investigation. The essential concept is that training sites may be derived independently for each image in a time series by identifying locations that have not undergone a land cover change, labeling these locations with an existing classified map, and using these training sites to condition a unique classifier for each image date. In this way, class spectral definitions are consistent through time and adaptive to differences between images due to atmospheric effects, view/illumination geometry, surface moisture conditions, and phenological differences. This obviates the need to correct for image differences with absolute or relative correction. Furthermore, since class signatures are uniquely adapted to individual images, the AASG method has the potential to classify temporally irregular time series in which vegetation has undergone phenological change. This is not possible with traditional signature extension, even if image differences were removed perfectly, and so limits the potential of that method to utilize temporally sparse data archives. Given any image pair, the AASG approach has the potential to be at least as accurate as traditional signature extension and independent image classification while maintaining an automated workflow and increasing data flexibility, attractive features for large-scale operational approaches.

The principal challenge is to identify stable areas that are suitable to train the classifier for each image. Two goals guide the selection of these locations: identify pixels that have not changed class between the image dates, and account for spatial uncertainty in the image pair and the classified map used to identify and label the locations. Image change detection has perhaps one of the most robust literatures in all of remote sensing science (see the reviews by Singh (1989), Coppin and Bauer (1996) and Lu et al. (2004), for example), but many effective approaches are based on simple band differencing and thresholding. If it is assumed that the majority of the image area did not change class (a condition usually met when the image covers a sufficiently large area), then the observed radiometric differences for most pixels may

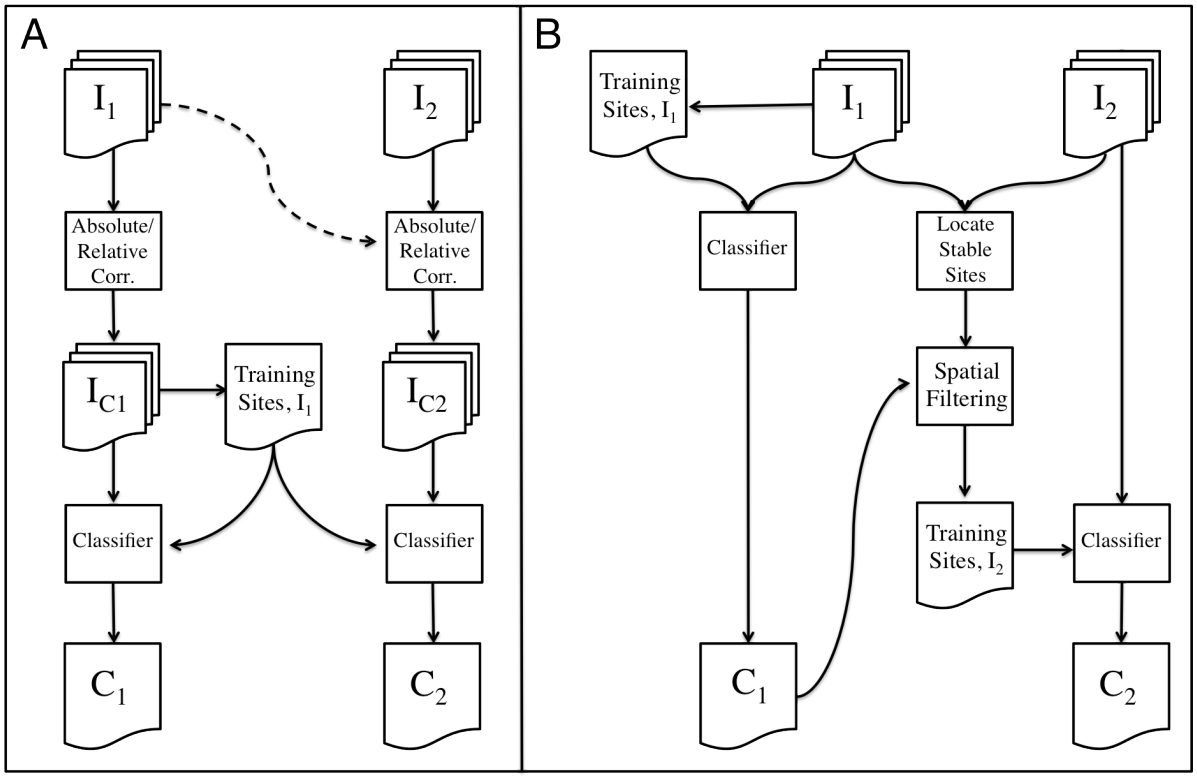

Figure 3.1: Comparison of workflows for traditional signature extension approaches (A), and the AASG method developed in this investigation (B). In both cases, the goal is to create classified maps C_1 and C_2 from input images I_1 and I_2. Signature extension requires that corrected images I_{C1} and I_{C2} be created either with a relative (dashed line), or absolute image correction procedure so that the training site information from I_1 may be used to classify I_2. In contrast, the approach proposed here automatically generates unique training sites for I_2 from stable locations in the scene.

be attributed to atmospheric effects, illumination/view geometry, or surface condition changes related to phenology or moisture differences. Considering the band difference histogram, stable locations would be located in an interval around the mean, and radiometric differences due to class changes would be in the tails of the distribution. Thus, for an image pair at times 1 and 2 (I_1 and I_2), a difference map can be constructed for each band n: $\Delta I_n = I_{1,n} - I_{2,n}$ and stable locations should be found among those pixels where ΔI_n is in the interval $\mu \pm c \cdot \sigma$, where μ is the mean and σ is the standard deviation of ΔI_n, and c is a user-selected constant determining the width of the stable interval. The resulting binary stable pixel masks may be combined by intersection to refine the stable locations based on multiple band differences. The fact that there is usually high covariance among image bands means that it is not typically necessary to use all image bands to identify class changes, and a few band difference images will suffice for most classification schema.

Once stable pixels have been identified, a single classified map at time 1 (C_1) is used to assign class labels to the stable locations. However, these locations may not yet be used to generate class signatures for the image at time 2 (I_2) because of spatial uncertainty due to misregistration of the individual images and the classified map (Townshend et al., 1992). This misregistration presents two challenges: identifying if a pixel is actually stable, and correctly labeling the pixel. Confusion occurs in the former case along boundaries between stable and unstable pixel regions, and in the latter along the boundaries between different land cover regions. Provided that the images and classified map have been coregistered to within a pixel of each other, then a class-by-class erode filter with a 3×3 kernel may be used to account for both sources of uncertainty (Fig. 3.2). This procedure significantly reduces the number of pixels available to be used as training data, particularly in small study areas or when landscapes are heterogeneous at fine spatial scales. Care must therefore be taken in the selection of stable pixels (through the selection of c), especially in complex landscapes and with complex classification schema.

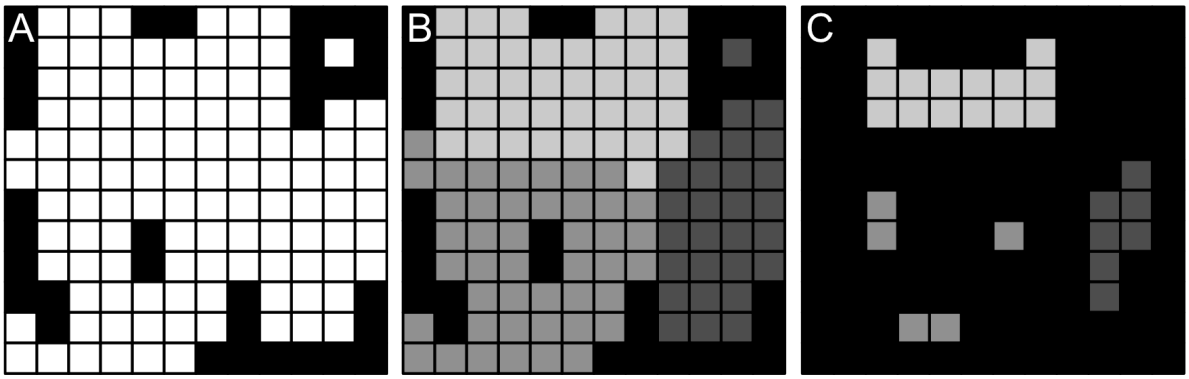

Figure 3.2: Illustration of the spatial filtering process necessary to account for spatial uncertainty due to image misregistration. First, a binary map of stable locations are determined using band differencing and thresholding (white pixels in A are stable, black are not). Next, class labels are assigned to stable pixels using an existing classified map (three classes are evident in B). Finally, an erode filter (3×3 kernel) is applied to each class in the labeled stable pixels map to create a final map (C) of locations which are assumed to be both stable and accurately classified.

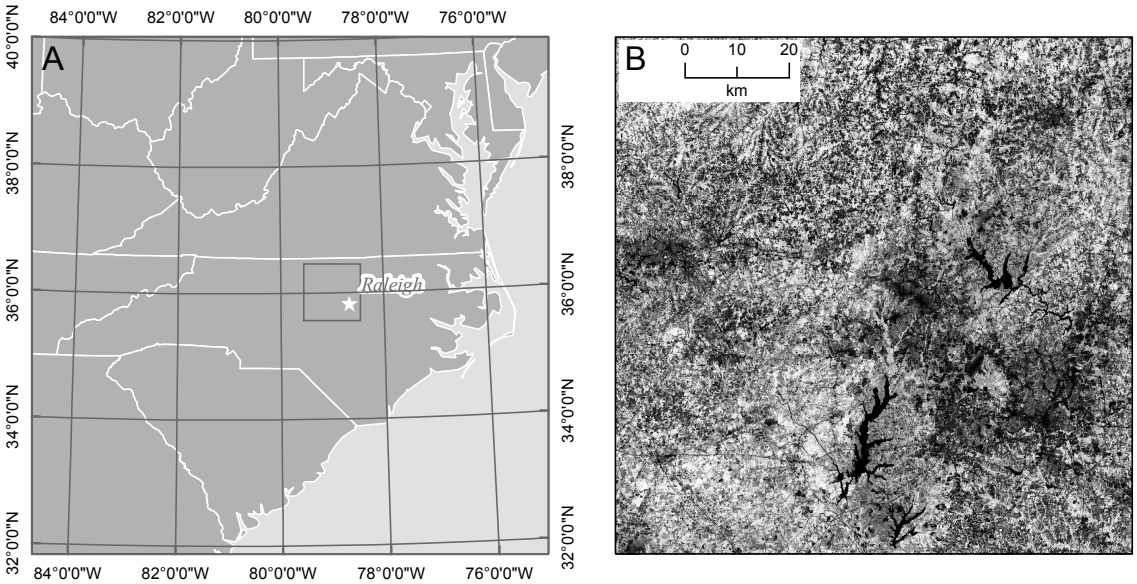

Figure 3.3: Our 100×100 km study-area shown in the context of the mid-Atlantic region of the United States (A), and NDVI over the entire study-area on 2005/7/27 (B).

3.2.2 Study Area, Data, and Preprocessing

A region of central North Carolina around the capital, Raleigh, was chosen to compare the performance of AASG and signature extension approaches. This study area was selected because it contains a wide variety of natural and human-dominated land cover types, has experienced widespread land cover change associated with urbanization and shifting agricultural practices over the past several decades, and is one of the fastest growing metropolitan areas in the United States. One winter and two summer Landsat TM images (WRS path: 16, row: 35, image dates: 1992/3/1, 1992/5/4, and 2005/7/27) were subset to a 100×100 km area around the cities of Raleigh and Durham (Fig. 3.3, center: $35°0'4''\text{N}, 79°0'1''\text{W}$) and converted to planetary top-of-atmosphere reflectance (ρ_0) using the constants and updated calibration coefficients provided by Chander et al. (2009). In order to increase class separability, we then derived a limited selection of spectral derivatives and ancillary information for each image: simple ratio vegetation index (Jordan, 1969), normalized difference vegetation index (Rouse et al., 1973), structural index (Fiorella and Ripple, 1993), and the topographic wetness index calculated from a National Elevation Dataset 30 m resolution digital elevation model (as defined by Beven and Kirkby (1979): $\text{TWI} = \ln(A/\tan\beta)$, where A is upslope contributing area and β is local surface slope).

We used maximum-likelihood classification to map land cover in 2005 to obtain a reference map for the AASG approach and spectral signatures for the signature extension approach. The classifier was trained on user-defined reference sites (delineated using 2005 color aerial photography), TM spectral bands (ρ_0), and derived/ancillary information from the 2005/7/27 TM image for seven land cover types: water, urban, suburban, deciduous forest, evergreen forest, wetlands, and crops/pasture. The suburban class is defined as the mix of natural vegetation, managed vegetation, and impervious surfaces characteristic of suburban neighborhoods. There is a strong correspondence between this class and the "developed, open space", "developed, low intensity", and "developed, medium intensity" classes used in the 2001 National Land Cover Dataset (Homer et al., 2004).

3.2.3 Assessment of Performance

Performance of the automatic adaptive signature generalization method was compared to traditional signature extension with three different levels of image correction: conversion to ρ_0, conversion to surface reflectance (ρ) via atmospheric correction, and relative correction of ρ_0 between image pairs. Additionally, the ability of AASG to classify image pairs that are from different seasons was tested. This potential application is particularly appealing because signature extension would be expected to perform poorly in such cases due to changes in vegetation spectral signatures associated with phenological development. Furthermore, high quality anniversary date images are not always available when constructing a time series of images, particularly in areas with frequent cloud cover. Finally, the sensitivity of classification accuracy to selection of the thresholding parameter c was assessed. It should be stressed that this investigation sought to demonstrate the efficacy of the proposed method relative to existing signature extension methods for consistently and accurately classifying time series of images, and not to demonstrate improvements in overall map accuracy for individual classified maps, or to suggest a particular supervised classification algorithm. In fact, an attractive aspect of the AASG aproach is its flexibility with respect to classification algorithm. Therefore, maximum-likelihood classification (MLC) was used for all tests because it is well understood, easily implemented, and relatively computationally efficient.

Classification of Summer-Summer Image Pairs

Class signatures were extracted from the 2005/7/27 TM ρ_0 image and used to classify the 1992/5/4 TM ρ_0 image using MLC for a "baseline" signature extension approach (i.e., correcting only for differences in irradiance, not atmospheric effects). Next, the relative image correction procedure proposed by Hall et al. (1991) was used to generate a 1992/5/4 rectified TOA reflectance ($\hat{\rho}_0$) relative to 2005/7/27 ρ_0. The Hall et al. (1991) correction works by fitting band-by-band linear transfer functions between control points assumed to represent areas with the same average surface reflectance between image dates (e.g., deep reservoirs and bright concrete), and then applying these functions to one of the images in order to rectify it to the

other. The relatively corrected 1992/5/4 $\hat{\rho}_0$ image was then classified as before, with MLC and the class spectral signatures extracted from the 2005/7/27 ρ_0 image. We then applied an absolute atmospheric correction to both the 1992/5/4 and 2005/7/27 TM images to obtain surface reflectance (ρ) images. A simple dark object subtraction (DOS) procedure was used (specifically, the "DOS3" method outlined in Song et al. (2001)), because such corrections have been shown to perform well for signature extension (Pax-Lenney et al., 2001). Class signatures were extracted from the 2005/7/27 ρ image using the same training sites as before, and were then used to classify the 1992/5/4 ρ image using MLC. Finally, we used the AASG method to classify the 1992/5/4 ρ_0 image using the 2005/7/27 ρ_0 image and the 2005/7/27 classified map. Landsat TM bands three and four were used in the differencing/thresholding procedure with the parameter c set at 0.5.

Accuracy of the four 1992/5/4 classified maps were assessed using over 100 validation sites selected with a simple random sampling design (Stehman, 1999) and labeled using leaf-on aerial photographs collected in 1993 and 2005. Homogeneous blocks of pixels (3×3) were employed as the assessment unit because they are robust against spatial misregistration (Stehman and Wickham, 2011). Confusion matrices, overall map accuracy, kappa coefficient of agreement, and class specific producer's and user's accuracies were generated for each classified map (Congalton, 1991; Foody, 2002).

Classification of Summer-Winter Image Pairs

A similar procedure was used to test the ability of AASG to classify image pairs with significantly mismatched collection dates. Specifically, we tested the performance of the AASG method when presented with a late winter Landsat TM ρ_0 image (1992/3/1) and the 2005/7/27 ρ_0 image along with the 2005/7/27 classified map. Given the same resources, traditional signature extension would be expected to perform poorly. Deciduous vegetation and seasonally snow covered surfaces, for example, would have very different spectral signatures than their summer counterparts. However, the AASG method derives spectral signatures from the individual images themselves, and the signatures therefore have the ability to adapt to more than just atmospheric and illumination/view geometry effects. If stable locations can be reliably

identified, then the AASG method could perform as well as independent image classification for any set of collection dates in a time series. It should be noted that in cases where the class spectral signatures change in such a way as to introduce class confusion, the achievable classification accuracy may be lower than an in-season image pair due to reduced class separability.

The main challenge in identifying stable locations with the proposed band-by-band differencing and thresholding approach when class signatures have changed through time is that while there will be large radiometric differences for certain bands in some classes, other classes will show no change in their spectral signatures (Fig. 3.4). In these cases the implicit assumption that the band difference histogram is unimodal and normally distributed no longer applies, and using the mean-based thresholding procedure to identify stable locations is unreliable. For example, discriminating stable sites based on a near-infrared band thresholding procedure in an image dominated by deciduous vegetation would neglect all locations which are stable, but not deciduous vegetation, resulting in few or no training sites for all other classes. A possible alternative is to use a selection of bands in the thresholding procedure which are unaffected by the physical changes in particular class signatures. The penalty for imposing this type of limitation is that some band combinations are incapable of discriminating class changes when the classes share a similar spectral response across the selected bands. Pixels which have undergone such a change are mistakenly identified as stable and assigned an incorrect class label. These misclassified pixels reduce class separability by contaminating the spectral signatures, resulting in degraded classifier performance. However, if land cover change is rare, then very few pixels in the image will have experienced actual class changes, and even fewer will have experienced the type of land cover change that is impossible to discriminate with a particular selection of bands. The result is very few misclassified pixels contaminating the class spectral signatures and minimal impact on classifier performance, at least for classification algorithms such as MLC which rely on mean spectral response.

We hypothesized that TM band 3 difference alone could be used to identify stable locations between the 2005/7/27 and 1992/3/1 images, based on its demonstrated effectiveness for this purpose in previous investigations (e.g., Ridd and Liu (1998)). Band 3 is sensitive to

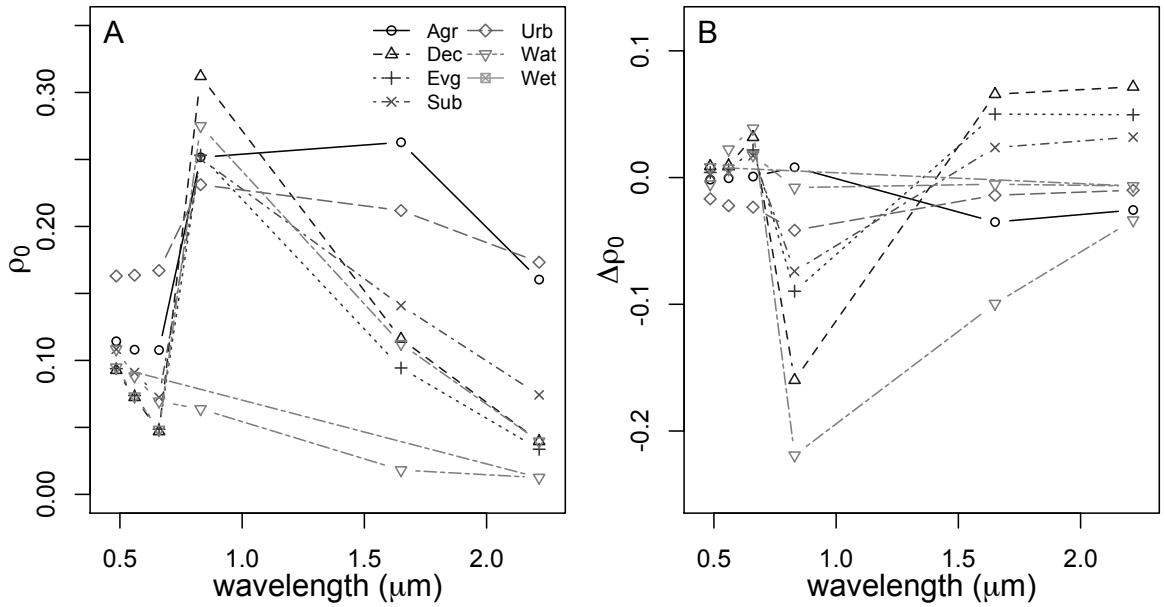

Figure 3.4: Mean summer spectral signatures (A) and the difference between winter and summer mean spectral signatures $\Delta\rho_0$ (B) for the land cover classes considered in this investigation.

class changes, particularly those altering the barren/impervious surface and natural vegetation proportions which are associated with urbanization and other anthropogenic changes, but is relatively similarly affected across all classes by atmospheric effects (Fig. 3.4), making it the best choice for identifying stable locations in our study area. We used the AASG approach with this image differencing criteria and $c = 0.5$ to classify the 1992/3/1 ρ_0 image given the 2005/7/27 ρ_0 image and the 2005 classified map. Another baseline performance comparison was conducted by classifying the 1992/3/1 ρ_0 image using spectral signatures derived from 2005/7/27 ρ_0 image. Accuracy of the two classified maps was assessed using the same validation data and procedure described in section 3.2.3

Threshold Sensitivity

The thresholding parameter c influences the characteristics of the stable training set by determining the range of radiometric variation assumed to result from processes *other* than land cover change. Therefore, this tolerance determines the probability of mistakenly identifying a change pixel as stable, and the overall number of stable pixels available for training. The

goal is to select a value of c which minimizes the number of misclassified pixels while maintaining sample sizes adequate to describe the spectral characteristics of land cover classes. We hypothesized that, with respect to classifier performance, there would be an optimum c value above which classifier performance is degraded by the inclusion of misclassified pixels in the training set, and below which class spectral characteristics are inadequately described by the training set due to too few samples. If class separability were observed to decrease with increasing c, then the former portion of the hypothesis would be supported. Reduced performance for individual classes associated with low training set numbers would support the notion that a restrictive c degrades performance by failing to capture the full range of class spectral variability. Sensitivity of the AASG method to c was assessed by classifying the 1992/3/1 ρ_0 TM image using the 2005/7/27 ρ_0 image, and independently classified 2005 land cover map at three different levels of the c parameter: 1, 0.5, and 0.25 (using TM bands 3 and 4 ρ_0 difference images). Class separability of the training set was determined for each level of the thresholding parameter, and overall map accuracy, kappa coefficient, and producer and user accuracies were calculated as before.

3.3 Results

3.3.1 Signature Extension vs. AASG

AASG and traditional signature extension with absolute atmospheric correction performed nearly identically, and best overall of the various methods of generating class signatures for classification of the 1992/5/4 TM image (Table 3.1). Signature extension with relative and TOA reflectance corrections performed slightly worse, but still well overall for the summer-summer image pair. The AASG method was able to maintain high overall classification accuracy (66%) in the winter image (1992/3/1) whereas traditional signature extension performed only slightly better than random assignment ($\kappa = 0.07$).

The AASG method achieved the highest user accuracies for forested classes (Dec and Evg; Tables 3.2 and 3.3), but had low user's and producer's accuracies for the wetlands and suburban classes (Wet and Sub, resp.). All tested methods over-predicted urban class (Urb) membership

Signature Generation Method	Image Date	Overall Acc. (%)	κ
User Supervised	2005/7/27	68.34	0.59
Sig Ext: TOA Reflectance (ρ_0)	1992/5/4	69.13	0.56
Sig Ext: Relative Correction ($\hat{\rho_0}$)	1992/5/4	70.42	0.65
Sig Ext: Absolute Correction (ρ)	1992/5/4	72.79	0.66
Automatic Adaptive Generalization	1992/5/4	72.99	0.68
Sig Ext: TOA Reflectance (ρ_0)	1992/3/1	15.37	0.07
Automatic Adaptive Generalization	1992/3/1	66.02	0.63

Table 3.1: Overall accuracy and kappa statistic (κ), for the classified maps generated via user-supervised signature generation, signature extension with three levels of image correction (conversion to ρ_0, $\hat{\rho_0}$, and ρ), and the AASG method proposed in this investigation.

(high producer's and low user's accuracy), and under-predicted membership (low producer's and high user's accuracy) in the crops/pasture (Agr) class (Tables 3.2 and 3.3). Overall, in comparison to the various methods of signature extension, AASG showed improved or similar performance for producer's and user's accuracies across all classes except suburban, for which AASG performed slightly poorer than signature extension with relative and absolute image corrections.

	2005/7/27 User			1992/5/4 AASG			1992/3/1 AASG		
Class	Prod.	User	Area (%)	Prod.	User	Area (%)	Prod.	User	Area (%)
Agr	41.4	77.4	9.8	39.9	70.5	10.8	51.0	67.3	16.3
Dec	68.4	82.8	22.8	90.6	96.7	26.3	66.7	79.7	29.6
Evg	48.8	62.7	13.8	75.9	84.3	15.4	82.1	83.1	16.2
Sub	78.8	46.6	39.0	65.6	62.0	26.9	45.0	49.7	23.9
Urb	95.6	72.3	4.7	96.7	42.7	7.5	98.9	54.3	5.5
Wat	90.0	100.0	1.4	86.7	100.0	1.4	92.2	100.0	1.6
Wet	65.1	45.6	8.4	60.3	54.3	11.7	100.0	56.8	7.0

Table 3.2: Class producer's and user's accuracy, and the percentage of the study area assigned to each class (Area) for the 2005/7/27 map classified with user-defined training sites, and the 1992/5/4 and 1992/3/1 maps classified with via the AASG method.

The suburban class exhibits the highest spectral variation of all classes and was over-predicted in the 2005/7/27 classified map at the expense of every other class except urban and water. This is evidence of the propagation of error from the 2005/7/27 map to the 1992/5/4 map that is unique to the AASG approach. That is, the training sites generated with the

	1992/5/4 ρ_0			1992/5/4 $\hat{\rho}_0$			1992/5/4 ρ		
Class	Prod.	User	Area (%)	Prod.	User	Area (%)	Prod.	User	Area (%)
Agr	34.3	70.8	8.9	40.9	75.7	15.0	43.4	76.1	15.6
Dec	85.4	93.9	24.0	78.8	83.5	30.9	79.2	83.2	31.1
Evg	37.7	74.4	7.9	67.1	77.1	13.9	67.7	79.6	13.8
Sub	66.1	42.2	44.5	72.0	69.4	25.5	71.4	78.0	25.1
Urb	97.8	35.8	11.9	98.9	43.8	7.3	98.9	44.3	7.2
Wat	84.4	100.0	1.3	89.9	100.0	1.5	86.5	100.0	1.4
Wet	27.0	77.3	1.7	63.5	50.0	5.8	100.0	18.4	5.8

Table 3.3: Class producer's and user's accuracy, and the percentage of the study area assigned to each class (Area) for the 1992/5/4 classified maps generated via signature extension with three levels of image correction (ρ_0, $\hat{\rho}_0$, and ρ).

automatic adaptive approach contain some mislabeled pixels in favor of the suburban class, broadening the spectral envelope of the class and resulting in increased suburban class confusion in the 1992/5/4 classified map. The traditional signature extension approach suffers from relatively low class predicted accuracy, but does not take the additional penalty of contaminated class spectral signatures. Note that this is different than the contamination of spectral signatures due to mislabeling change pixels as stable (described in Section 3.2.3), and emphasizes the importance of the *user's accuracy* of the initial classified map to the AASG approach.

The pattern of producer's and user's accuracies for the 1992/3/1 ρ_0 image classified via AASG is similar to the 1992/5/4 ρ_0 image classified with the same method, with some reduced accuracy in the deciduous and suburban classes. Extension of class signatures from the 2005/7/27 ρ_0 image to the 1992/3/1 ρ_0 image performed poorly, with zero producer's and user's accuracy for all classes except water which was well predicted, and urban which was predicted for all non-water spectral responses (100% and 9%, producer's and user's accuracies, respectively).

3.3.2 Threshold Sensitivity

As previously discussed (Section 3.2.3), the thresholding parameter c determines the characteristics of the pixels used as training sites in the AASG method by limiting the amount of

tolerable variability in band difference images. Overall classified map accuracy was high across all three values of c that we tested. There was a modest reduction in overall accuracy and κ associated with the minimum threshold value, but no difference for the higher c values (Table 3.4). The lack of large changes in overall accuracy can be partially attributed to the fact that classes which are a large constituent of the study area (e.g., deciduous), are relatively well classified and robust against changes in c (Table 3.5). However, class accuracies among the lesser represented classes in the study area exhibited larger changes in accuracy associated with different values of c.

c	Overall (%)	κ
0.25	71.7	0.65
0.50	73.3	0.68
1.00	73.3	0.68

Table 3.4: Overall accuracy and κ for the 1992/5/4 TM image classified with the AASG method and three levels of the thresholding parameter c.

	$0.25 \times \sigma$			$0.5 \times \sigma$			$1 \times \sigma$		
Class	# Pixels	Prod.	User	# Pixels	Prod.	User	# Pixels	Prod.	User
Agr	*36*	**76.3**	**77.0**	1497	39.9	70.5	**18756**	**42.4**	*62.2*
Dec	*1320*	**95.8**	*90.2*	33708	90.6	96.7	**242693**	*88.5*	**97.3**
Evg	*4068*	*62.4*	*84.2*	60791	75.9	84.3	**211455**	**85.8**	*81.7*
Sub	*166*	**74.1**	*45.9*	23789	65.6	62.0	**316450**	*56.6*	**68.6**
Urb	*11*	*14.4*	*39.4*	536	96.7	42.7	**9410**	96.7	**43.9**
Wat	*23088*	**91.1**	100.0	73638	86.7	100.0	**99237**	**87.8**	100.0
Wet	*33*	*19.1*	*31.6*	772	60.3	54.3	**8049**	**65.1**	*51.3*

Table 3.5: Producer's and user's accuracies and the number of stable training pixels per class for the 1992/5/4 classified maps generated via the AASG method at three different threshold levels: $0.25 \times \sigma$, $0.5 \times \sigma$, and $1 \times \sigma$. **Bold** text indicates quantities that are greater than their counterpart when $c = 0.5$, whereas *italic* text indicates the quantity is less.

An increase in c led to an order-of-magnitude increase in the number of pixels in the stable training set in every instance except for water (Table 3.5), which is unique in being much more spatially, spectrally, and temporally uniform than the other classes. When $c = 0.25$, there were few stable pixels selected for the crops/pasture, urban, and wetlands classes. In the case of the urban and wetlands classes, the samples were insufficient to describe the spectral variability,

leading to reduced classification accuracy when $c = 0.25$ compared to the higher thresholds. In contrast, the crops/pasture class had a similarly low number of training pixels (36) when $c = 0.25$, but achieved higher classification accuracies under that condition than when c was increased. This result may be partially explained by the fact that the number of training pixels increased much more as c increased from 0.25 to 0.5 for the crops/pasture class than for the urban and wetlands class, leading to greater propagation of misclassification errors from the reference classified map.

Among the classes with sufficient training pixels to describe the class spectral variability, evergreen forest had lower producer's and user's accuracy when $c = 0.25$ than when $c = 0.5$, whereas deciduous and water classes both reached their highest producer's accuracy at the smallest c value. Producer's accuracy increased and user's accuracy decreased for crop/pasture, evergreen, and wetlands classes as c increases from 0.5 to 1, whereas deciduous and suburban classes show modest opposite trends (Table 3.5). Neglecting the most restrictive threshold, the class specific accuracies are broadly consistent with those of the 2005/7/27 reference map (Table 3.2).

Class separability, as measured by Jeffries-Matusita distance, exceeded 1.8 for all class pairs when $c = 0.5$ (Table 3.6). Class separability decreased when c increased from 0.5 to 1 for all pairs except wetlands-evergreen, and increased when c was decreased from 0.5 to 0.25, though the differences were modest for all pairs except suburban-crops/pasture and suburban-evergreen (Table 3.7). The suburban class became appreciably less separable from crops/pasture and evergreen classes when c was increased from 0.5 to 1.0, ultimately leading to an under-prediction of membership in this class (increased user's accuracy and decreased producer's accuracy, Table 3.5).

3.4 Discussion

3.4.1 Relative Performance of AASG and Signature Extension

Our results indicate that the AASG approach is capable of performing as well as traditional signature extension approaches in the conditions most suited to the traditional approach: an

Class	Agr	Dec	Evg	Sub	Urb	Wat	Wet
Agr	-	2.00	2.00	1.94	2.00	2.00	2.00
Dec	-	-	1.98	1.98	2.00	2.00	1.84
Evg	-	-	-	1.94	2.00	2.00	1.80
Sub	-	-	-	-	2.00	2.00	1.98
Urb	-	-	-	-	-	2.00	2.00
Wat	-	-	-	-	-	-	2.00
Wet	-	-	-	-	-	-	-

Table 3.6: Jeffries-Matusita distance with the AASG threshold parameter c fixed at 0.5

Class	Agr	Dec	Evg	Sub	Urb	Wat	Wet
Agr	-	0	0.02	0.19	0	0	0
Dec	0	-	0.02	0.01	0	0	0.06
Evg	0	-0.02	-	0.16	0	0	-0.1
Sub	-0.03	-0.02	-0.03	-	0	0	0
Urb	0	0	0	0	-	0	0
Wat	0	0	0	0	0	-	0
Wet	0	-0.13	-0.1	-0.02	0	0	-

Table 3.7: Difference in Jeffries-Matusita distance between the training set when $c = 0.5$ and $c = 1$ (upper-triangle), and between $c = 0.5$ and $c = 0.25$ (lower-triangle). For example, the Jeffries-Matusita distance between the Agr and Sub classes was 0.19 greater when $c = 0.5$ than when $c = 1$

in-season image pair with minimal atmospheric or scene moisture/phenological differences. The ability to adapt to changes in class spectral signatures is a significant advantage of the AASG approach over signature extension, particularly in areas where persistent cloud-cover or infrequent image collection lead to temporally sparse data archives. However, the AASG method is vulnerable to contamination of class signatures by propagation of two related errors: misclassification in the initial reference map, and mislabeling of stable/change pixels. As a general rule, if the reduction in classification accuracy resulting from signature contamination in the AASG process is less than the increase in accuracy associated with improved temporal signature generalization, then the AASG approach would be preferred to signature extension. The experimental classification of out-of-season image pairs illustrates this point: the adaptive winter signatures, accepting all misclassification errors, offer large increases in accuracy compared to extension of summer signatures. Under the optimum condition of a summer-summer image pair, the balance struck between errors in the two methods is much closer, and the

importance of the accuracy of the initial reference and stable site maps to the AASG method is emphasized.

A useful boundary condition for signature contamination through misclassified pixels in the automatically generated training set is given by the case when $c = \infty$. In this case, the training set is simply the spatially filtered reference map with no accounting for change pixels. However, if land cover change is rare and the reference map is accurately classified, then the impact of misclassifications on class mean spectral signatures is small (at least for classifiers such as MLC dependent on the mean vector). Furthermore, the spatial filtering process significantly refines the training set by selecting only from homogeneous sites which are more likely to emphasize the central tendency of class spectral signatures than increase class spectral variability due to sub-pixel scene heterogeneity. This suggests that reference map accuracy more strongly determines AASG results than threshold selection. The fact that we observed little change in overall map accuracy with changes in c supports this hypothesis, although at least partial contribution must be given to the areal proportions of land cover and the relatively high classification accuracy for major constituents as discussed previously (Section 3.3.2). We nevertheless observed sensitivities of individual class accuracies to c, due primarily to large differences in training set size. Furthermore, the classification accuracy of the initial reference map is determined by the limitations of a particular study, and not by any consequence of the AASG method. In the context of the development of the AASG method, it is therefore useful to consider the ways in which the selection of c determines training set characteristics.

3.4.2 Threshold Sensitivity

We hypothesized that there should exist an optimum value of c above which classifier performance was reduced by inclusion of misclassified pixels in the training set, and below which the number of pixels in the training set are inadequate to describe the actual spectral variability of classes, also degrading classifier performance. Considering MLC, adding training sites either expands or contracts the decision regions in spectral space (except when the additional set exactly matches the statistical properties of the existing set). Assuming that the existing set

is already sufficient to describe the full range of class spectral variability, and that all other class decision regions are static, broadening decision regions leads to over-prediction of class membership and an associated increase in producer's and decrease in user's accuracy. Contracting the spectral decision region would generate the opposite response, with fewer pixels predicted to belong to a class, but with greater certainty.

Applying this logic to the results of our experiment, crop/pasture, evergreen, and wetlands classes exhibit the pattern of increasing producer's and decreasing user's accuracy associated with a broadening of the class spectral decision regions as c increases from 0.5 to 1, whereas deciduous and suburban classes show modest opposite trends (Table 3.5). In the case of AASG, the assumption that other class decision regions are static is not met, and the actual changes in class accuracies are determined not only by the characteristics of the additional training sites, but also by relative changes in other class spectral decision regions. In that respect, the small increases observed in deciduous and suburban user's accuracy may be due to relative decreases in other classes, and not a refinement of the class spectral signatures. The observed over-prediction of crop/pasture, evergreen, and wetlands classes as c increased is easier to reconcile with the theoretical contamination of class spectral signatures associated with inclusion of misclassified pixels as the thresholding parameter increases. At a minimum, the results indicate that c must be selected in such a way that some minimum number of pixels per class is obtained.

While there is limited dependence of overall map accuracy on c, there is at least the potential for a more informed selection than arbitrarily assigning a constant. An interactive selection procedure that started with a small c value and increased until some minimum number of training sites were achieved in each class would be a simple improvement that would be easy to operationally implement. Our results suggest that further improvements could perhaps be achieved by selecting class specific c values rather than a single value across all classes. The theoretical implication is that classes would have a unique threshold of tolerable temporal spectral variation. Crops/pasture, for instance, shows much larger temporal spectral change than water, and thus requires a higher c value to obtain the same number of stable sites (Table 3.5). Interactively selecting class specific c values would have the benefit of achieving

optimum training site sizes for each class, and limit the spectral contamination resulting from too many training sites in classes with modest temporal spectral variability. Defining an objective function for this interactive selection is an important consideration. The simplest approach would be to require a minimum number of pixels per class, but this runs the risk of not capturing the full spectral variability in diverse classes. A better approach might be to adjust c until the class specific spectral variance/covariance statistics of the training set are within some small deviation of their counterparts in the reference map. This would have the attractive quality of maximizing semantic consistency between the reference and AASG classified maps, but would limit the ability of the training signatures to adapt to changes which altered class (co)variance. A constrained approach to the selection of c could be achieved by attempting to maximize the resulting classification accuracy, either with independent reference data at a single date in the image, or by using the automatically generated signatures to classify the reference date imagery and comparing the result to the reference classified map, although this would result in the same adaptation penalty as previously discussed and would therefore be best suited for in-season image time series.

Despite the similarities between change detection and stable site selection, there are important conceptual and practical differences. In the context of this study, the most important difference is that stable site selection can have more conservative thresholding criteria because there is no penalty for mislabeling a pixel that was actually stable once a sufficient sample of training sites has been determined. In other words, the goal of stable site selection as employed by AASG is to maximize the *user's accuracy* of the resulting binary stable site map with no regards to the producer's accuracy. In contrast, the majority of change detection methods have the goal of maximizing the overall accuracy, and must therefore try to identify the actual "true" threshold value.

3.4.3 Practical Considerations and Limitations

With respect to operational potential, the proposed AASG method has several attractive qualities. It is straightforward to automate, requires only a single well classified reference map for one of the images in the times series, is flexible with respect to classification algorithms,

and has the potential to utilize temporally irregular image time series because signatures are adaptive. AASG offers the additional practical benefit of not requiring an image correction procedure and the associated image-by-image parameterization, but incurs a computational cost due to the spatial filtering process used to determine stable sites. The AASG approach is capable only of within-scene temporal generalization of signatures. In contrast, signature extension has the theoretical potential to accommodate out-of-scene generalization, although it has performed poorly in such applications (Woodcock et al., 2001). This limitation is somewhat ameliorated because there is an increasing number of high-quality, large area classifications limited only in their temporal extent. AASG offers the potential to use these products as reference data, thereby taking advantage of their spatial consistency, but solving the problem of inadequate temporal density.

The most critical assumption of the method is that there are many more stable pixels in the study area than change pixels, and that they can be identified through simple band differencing procedures. Violations of this condition can occur in small study areas where the land cover change proportion is high, or when class changes are not resolvable using band-by-band spectral differences. Class spectral confusion is common to any spectrally based mapping approach, however, and most land cover schema feature classes which are well distinguished in spectral space. Furthermore, the limited impact of change/stable classification errors on AASG performance under such conditions has been previously discussed (Sections 3.2.3 and 3.4.1). It remains, though, that the thresholding criteria exerts the strongest influence on AASG performance aside from those factors which are external to methodological choice (e.g., land cover schema, reference map accuracy, and data properties), and a strategy for optimal selection of c, and band difference images is required for operational deployment.

Of the alternatives to band differencing for change detection summarized by Lu et al. (2004), the only ones amenable to an automated approach are transformations and advanced models. Transformations such as principal components analysis and Kauth-Thomas ("tasseled-cap") may provide more accurate and efficient change detection than band differencing, but the requirement to select a threshold value remains. Advanced models such as spectral mixture models, canopy reflectance models, or estimation of biophysical parameters such as LAI

or fraction impervious surface require additional reference data to fit empirical equations or describe spectral endmembers, and are best suited to detecting specific changes such as forest conversion. It follows that thresholding of either band differences or transformed components is a requirement of automatic, general change detection, and reemphasizes the importance of a refined approach to automatic threshold selection.

Though we demonstrated the AASG approach using the maximum-likelihood classification algorithm, the approach could be implemented with any supervised classification method. However, the ways in which training site characteristics such as misclassification rate and sample size affect performance are different for other classification approaches. For instance, the computational requirements of artificial neural network (ANN) scale with the number of training sites, and having the very large number of sites identified in this study (e.g., at $c = 0.5$, Table 3.5) would present a significant computational burden with an ANN approach, whereas MLC is dependent only on computing the variance/covariance matrix which is considerably less influenced by training set size. Additionally, the fact that training sites are selected from homogeneous areas and thus are more representative of pure class spectral endmembers means that AASG derived training sites would be less than ideal for approaches such as support vector machines which depend on training sites at spectral class boundaries, often occurring at spatial class boundaries. Strategies for generating optimal training set sizes have been previously discussed, but it should be emphasized that tailoring the band thresholding procedure with careful consideration of the theoretical requirements of the chosen classification algorithm will achieve the best results.

3.5 Conclusions

Our investigation was motivated by the need to develop automatic approaches to consistently and accurately classify temporally irregular time series of remote sensing images. Data accessibility and computational limitations have hampered previous development along these lines, but the recent opening of long-term, global image archives such as the Landsat record, and revolutionary developments in computational resources such as massive storage and distributed

computing capabilities have stimulated renewed interest in the subject. Existing signature extension approaches can produce good results under optimal conditions, but have important limitations, and are incapable of adapting to the changes in class spectral signatures necessary to map irregular times series when phenological or surface conditions are present. We developed a method that automatically generates class spectral signatures, uniquely adapted to each image, from locations which are assumed to be stable with respect to land cover class. This automatic adaptive signature generalization scheme has attractive qualities for operational deployment to dense time series, particularly in sparse and irregular records which were of limited use to existing classification methods.

AASG was compared to traditional signature extension by classifying a summer-summer (2005/7/27 & 1992/5/4), and summer-winter (2005/7/27 & 1992/3/1) pair of Landsat TM images over a 100×100 km square study area in central North Carolina. Overall classification accuracy for the summer-summer pair was high for all methods considered, though there was a modest advantage for the AASG and atmospheric correction approaches. Signature extension performed poorly for the summer-winter image pair whereas AASG was able to maintain lower, but acceptably high overall classification accuracies relative to the in-season image pair. With regards to AASG, there is a tradeoff between increased classifier performance due to better signature generalizability, and decreased classifier performance due to propagation of errors from the reference map and stable site determination. At a minimum, AASG will have an advantage when class signatures change as a result of physical scene changes, and has the potential to perform as well as signature extension when spectral signatures are static, depending mainly on the accuracy of the reference and stable site map. It should be noted that even in-season image pairs, or study areas lacking deciduous vegetation may have changes in class spectral conditions due to factors other than atmospheric effects, such as changes in soil moisture status.

We tested the sensitivity of the AASG approach to the selection of the thresholding parameter c and found that c must be high enough to reach a class-specific minimum number of observations necessary to describe the actual class variability. Most class pairs showed

decreased spectral separability when c increased, and several classes showed evidence of over-prediction that would be expected when spectral decision regions are broadened due to signature contamination, supporting our hypothesis that there is an optimum c value, above which class spectral signatures are degraded by error propagation. The results suggest that using a single, arbitrarily selected value of c for all land cover classes is not ideal, and that a refined approach which allows a varying amount of tolerable temporal spectral variability for each class may lead to improvements in the automatically generated signatures. We propose that such a development may best be achieved with a procedure which interactively determines the thresholding parameter by optimization of classified map accuracy with independent data, or the existing reference data.

Though this approach is limited to within-scene applications, it might be used in combination with existing high-quality, large area land cover maps to expand the results to a temporal density limited only by data availability. As such, this development represents substantial progress towards utilizing long-term data records to gain a better understanding of historical land cover and land use change patterns, and for automatic, operational monitoring of land cover dynamics at arbitrary temporal and spatial scales. Important applications include refining land cover inputs to ecosystem and climate simulation models, and parameterizing predictive models of land cover dynamics with empirical change matrices at an unprecedented temporal resolution. The most important considerations in the application of the AASG approach are the accuracy of the classified reference and stable site maps. There is considerable flexibility in implementation, and it is expected that for any given study area, refinement of the classifier, input data, reference map, and change detection method will result in improved final products. For instance, we have already speculated on improvements to the thresholding procedure. However, it remains that we have demonstrated here, in it's most simple form, a novel and flexible approach to automatically classifying irregular time series of remotely sensed images more accurately and consistently than existing signature generalization methods.

Chapter 4
Climate and land cover effects on the hydrology of the Eno River watershed in central North Carolina

4.1 Introduction

The distribution of freshwater resources on Earth is controlled by climatic, physical, and biological processes which vary in time and space. Understanding these processes is essential in order to ensure growing demands on freshwater can be sustainably met in the future. Improved understanding of global water and climate cycles has led to the general conclusion that there will be an overall acceleration of the global hydrologic cycle due to climate change in the future, with global precipitation, evapotranspiration (ET) and runoff all increasing (Loaiciga et al., 1996; Jackson et al., 2001; Huntington, 2006; Oki and Kanae, 2006). Additionally, Land cover and land use influence hydrologic cycles directly through surface physical and biological properties, and through climate system feedbacks (Pielke et al., 1998). Globally, there are trends towards increasingly developed and anthropogenically managed landscapes with hydrological, agricultural, and biochemical implications for water cycles (Foley et al., 2005). Concurrently, there are increasing demands on freshwater resources associated with growing populations and increased per capita water use (Vorosmarty et al., 2000). These factors highlight the critical role that climate, ecosystem, and hydrological sciences play in sustainably managing freshwater resources and argues for coupled climate-ecosystem-hydrology simulation systems to project future dynamics. However, while the expected trends in water balance components are increasingly well defined at the global scale, regional changes are less certain (IPCC, 2007). Furthermore, management decisions are made at local to regional scales and there is a need to reconcile these scales with those of hydrologic and climate modeling investigations so that simulation results can inform environmental management decisions.

Vegetation, particularly forest, dominate much of the Earth's surface and plays a critical role in the global water cycle. Though water-vegetation interactions have long been appreciated, much of our initial hydrologic understanding of the role forest play in controlling watershed dynamics has been gained from the results of paired-catchment experiments dating back to the early 20th century (Hewlett et al., 1969; Bosch and Hewlett, 1982). These studies showed that catchment water yield is influenced by changes in the transpiration, evaporation and interception components of the water balance, all of which tend to increase with the amount of vegetation in the catchment (Stednick, 1996; Zhang et al., 2001; Brown et al., 2005a). The type of vegetation present is also important; forests typically transpire more water than do shrubs and grasses, and coniferous forest intercept and evaporate more precipitation than broad-leaf forests (Swank and Douglass, 1974; Swift et al., 1975; Farley et al., 2005). Planted and natural stands have different hydrologic properties due primarily to the ability of planted stands to support unnaturally high biomass due to irrigation and fertilization, and modeling exercises have demonstrated that plantations tend to reduce water availability (Pearce and Rowe, 1979; Cannell, 1999; Jackson et al., 2005).

Leaves are the primary interface between the forest ecosystem and the atmosphere, and are the site of water, energy and mass transfers. If environmental drivers of ET are held constant, then the amount of transpired water is proportional to the amount of leaves in the canopy, which is typically quantified by leaf area index (LAI). The relationship between vegetation production and environmental controls is generally well understood with water, light, CO_2, and nutrients being the dominant factors (Cowling and Field, 2003; Norby et al., 2003, 2005). Precipitation that is intercepted by plant canopies and subsequently evaporated is also an important part of the water budget (Rutter, 1963), and the differential interception rates of conifer and deciduous stands has been implicated as the most important factor affecting catchment water yields when these forest composition conversions take place (Swank and Miner, 1968). Grier and Running (1977) were the first to quantify the relationship between LAI and site water balance. Eagleson (1982) showed that in moisture-limited systems, vegetation would act to minimize water stress. Nemani and Running (1989) used this hypothesis to predict either equilibrium LAI or soil water–holding capacity when one of those two variables is known.

In general, we can say that vegetation affects the water balance primarily through ET, and that the magnitude of ET is strongly dependent on the amount of vegetation in a canopy. Furthermore, biological factors tend to optimize biomass at least in part according to local water availability. Thus, accurately simulating ET is of primary importance when simulating catchment response to climate and vegetation changes, and accurate characterization of vegetation distributions is necessary.

Stomatal conductance g_s, and it's canopy scale counterpart canopy conductance g_c are the most important limitations to ET in vegetation. It is controlled by plant physiology, specifically the regulation of stomatal aperture in response to water requirements for assimilation and available soil water. Stomata must serve the dual purpose of regulating water loss and allowing the influx of CO_2. The notion that the response of stomata over a given interval of time should act to optimize the amount of carbon gained to water loss was originally put forward by Cowan and Farquhar (1977) and enjoys a great deal of experimental support (as reviewed by Farquhar and Sharkey (1982)). The mechanisms for the regulation of stomatal conductance in response to leaf water balance are reviewed by (Buckley, 2005) who concludes that the hypothesis of "hydro-active local feedback" (a metabolically mediated response of the stomatal guard cells to local water status) explains most of the observed stomatal responses to changing environmental conditions. Many empirical and semi-empirical formulations have been developed to model the change in stomatal conductance with environmental drivers (von Caemmerer and Farquhar, 1981; Collatz et al., 1991; Leuning et al., 1995). In the seminal work of Jarvis (1976) the dominant relationships between g_s and environmental variables was established. He proposed an empirical relationship between g_s and functions of environmental driving variables: temperature, the air-leaf vapor pressure difference, photon flux density, ambient CO_2 concentration, and leaf water potential. These functions contribute a 0–1 coefficient which is used to reduce g_s from a theoretical maximum value. Alternative models such as the "Ball-Berry" model (Ball et al., 1988) which are more mechanistic in nature have also been developed. Despite the limitations of the Jarvis model, it is conceptually simple, easy to implement, and has been used in a wide variety of simulation models with success.

Climate-vegetation feedbacks are important at regional scales where increases in convective

precipitation and changes to sensible-latent heat balances may have large effects on large-scale climate and vegetation patterns. However, at the scale of a local catchment, climate change will affect hydrology primarily through alterations to the precipitation regime and changes in the magnitude of ET (Field et al., 1995). Higher concentrations of CO_2 allow plants to reduce stomatal conductivity leading to increased water use efficiency. This increase in efficiency may be offset by an increase in total leaf area such that the total amount of transpiration remains constant or even increases (Running and Nemani, 1991; Hatton et al., 1992; Field et al., 1995). Increasing temperatures alter the amount of energy available for evaporation and may lengthen growing seasons in some regions, both processes leading to increases in ET. Alternatively, increasing temperatures may exceed the optimal level for photosynthesis and transpiration may be attenuated.

The goal of this investigation was to assess the impacts of climate and land cover changes on streamflow and ET in a forested river basin in central North Carolina. We adopt an ecosystem simulation approach utilizing two existing ecohydrologic models which take different theoretical and structural approaches to simulating basin water balance components. An additional goal of this investigation was to contrast the two models and assess their relative performance. Our approach integrates improved remote sensing inputs describing land cover and vegetation distributions which are thought to increase the accuracy and reliability of simulated quantities. Importantly, this investigation makes progress towards reconciling the scale mismatches between the management and modeling communities by deliberately choosing spatial and temporal scales that are relevant to local environmental decision makers. It should be stressed that this investigation was an experiment designed to assess the relative impacts of climate and land cover changes across two models with contrasting theoretical implementations. As such, the results presented here do not constitute a forecast, and therefore should not be taken to represent a likely future scenario. Instead, these results should be used to compare the relative impacts of climate and land cover changes, and to assess differential responses across the two models used here.

4.2 Methods

We assessed the impact of climate and land cover changes on streamflow and ET in a moderate sized river basin in the North Carolina piedmont using two ecohydrologic models: RHESSys, a physically based, coupled hydrologic and ecosystem process model; and WaSSI, an empirically based model aggregated to 12-digit HUC basins. Three different climate scenarios and two land cover scenarios were considered for a total of six climate-land cover permutations. Climate scenarios were the 1961–1990 WMO baseline period, and 2051–2080 scenarios derived from two Global Climate Models (GCM). Contemporary land cover (2010) derived from remote sensing images was used along with a hypothetical future scenario featuring a large increase in the proportion of evergreen forest. Long-term monthly mean streamflow and ET were compared between model runs to disentangle the independent and combined effects of land cover and climate change. Additionally, WaSSI and RHESSys results were compared relatively and against observed streamflow.

4.2.1 Study Area

The Eno River, along with the Flat and Little Rivers are the major tributaries to Falls Lake (Fig. 4.1). The Eno basin drains 367.0 km^2 of mostly rural territory Northwest of the city of Durham. Terrain is gentle to moderate and elevation ranges from 82 m to 261 m. Contemporary land cover is 61% predominately deciduous forest, 5% predominately evergreen forest, 17% grass/pasture/agriculture, and 16% sparsely vegetated cover types based on the land cover maps developed in Chapter 3. Like much of the southeastern United States, this area seen increased forest area associated with agricultural abandonment and forest planting initiatives, and a more recent growth in developed areas due to a rapidly growing regional population (Wear and Greis, 2001).

Average temperature in the Eno during the baseline period period was 14.6°C with January minimum temperatures averaging −2.6°C and July maximum averaging 31.7°C. Annual precipitation averaged 1209 mm and was distributed evenly throughout the year. Annual average

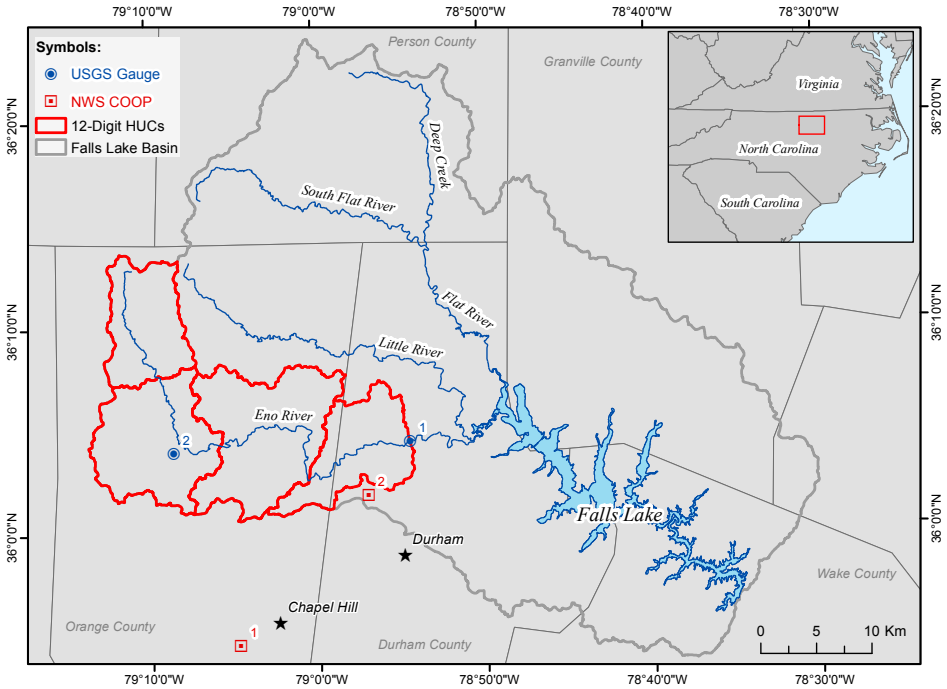

Figure 4.1: The Falls Lake basin in central North Carolina with major hydrological features, 12-digit HUC subbasins for the Eno basin, NWS Coop stations ("1": 31167, "2": 312515), and USGS gauges ("1": 02085070, "2": 02084909) used in this study.

temperature in the Eno basin decreased from the 1950's through the 1980's but has been increasing since then, in line with the overall warming trend observed for the globe (IPCC, 2007). Robinson (2006) found no trend in 20th century annual precipitation in North Carolina, but identified a decreasing trend in summer precipitation and increasing fall precipitation. Annual streamflow on the Eno averages 307 mm and the mean annual runoff ratio is 0.26.

4.2.2 RHESSys

RHESSys is a distributed ecohydrological process model designed to simulate ecosystem processes in small to moderate sized watersheds at a daily time step (Band et al., 1993; Tague and Band, 2004). Core components of the model include a hydrologic model which determines lateral soil moisture distribution (DHVSM (Wigmosta et al., 1994) for explicit routing, or TOPMODEL (Beven and Kirkby, 1979) for implicit routing), an ecological process model (BIOME-BGC (Running and Hunt, 1993)) providing simulated carbon, nutrient, and plant water cycles, a soil biochemical model controlling soil nitrogen processes (based on CENTURY

(Parton et al., 1996)), and a microclimatic model which accounts for topographic controls on precipitation and temperature (MTCLIM (Running et al., 1987)). A unique feature of RHESSys is its GIS managed, hierarchical landscape representation whereby the basin is subdivided into successively smaller units such as hillslopes and patches. Structuring the model in this way allows processes to be simulated at distinct spatial scales appropriate to the phenomenon, and allows greater flexibility in defining more ecologically meaningful landscape divisions than simple grids (Tague and Band, 2004). Previous investigations have demonstrated the utility of RHESSys for assessing the ecological and hydrological impacts of climate and land cover changes across basins with diverse vegetation, climate, and topographic regimes (e.g. Baron et al. (1998); Zierl et al. (2007); Tague et al. (2008, 2009)).

RHESSys utilizes the Penman-Monteith combination equation (Monteith, 1965) to simulate ET based on landscape properties and climatic drivers derived from the input series of minimum and maximum temperature and precipitation. RHESSys employs the Jarvis (1976) model of g_s. Conductance is scaled to the canopy by multiplying by the shaded and sunlit LAI adopting the approach of Chen et al. (1999). Canopy conductance is also used in the Farquhar and vonCaemmerer (1982) carbon assimilation model used by RHESSys which calculates a photosynthetic rate dependent on leaf enzymes, irradiance, conductance, CO_2 concentration, atmospheric pressure, and temperature (Waring and Running, 2007).

Lateral soil moisture redistribution are simulated at the finest spatial scale (the patch) via the quasi-spatially distributed statistical approach of TOPMODEL, or the explicit routing model adapted from DHVSM. Both approaches may be calibrated to provide reasonable results in many basins, but there are some important differences. Explicit routing is capable of simulating the observed shift in spatial patterns of saturated subsurface flow from spatially variable, locally controlled patterns during dry periods to more homogeneous flow regimes during wet periods, whereas the TOPMODEL approach generally maintains consistent spatiotemporal patterns of soil moisture (Tague and Band, 2001). When spatial patterns of soil moisture are important, in a land cover change assessment, for instance, the explicit approach would be preferred. Preliminary testing with calibrated models indicated that the explicit approach better replicated the observed patterns of streamflow for a small calibration basin

and was therefore adopted in this investigation. The RHESSys explicit routing algorithm calculates saturated throughflow between patches based on patch geometry, local surface slope, and transmissivity. The method described in Wigmosta et al. (1994) is adapted to account for non-uniform patch elements (Tague and Band, 2004). Transmissivity is calculated based on a local saturation deficit, saturated hydraulic conductivity at the surface (K_{sat0}), and the decay of hydraulic conductivity with depth (m). Lateral and vertical moisture fluxes are controlled by the vertical profile of hydraulic conductivity which is assumed to decrease exponentially with depth.

Spatial variability in soil properties is accommodated by an input soil map and associated parameters. However, preferential flowpaths and macropore flows dominate lateral redistribution at the hillslope scale and the hydraulic model must be calibrated to account for these site specific conditions (McDonnell, 1990). Typically m and K_{sat0} are calibrated against observed streamflow in order to account for preferential flow properties of the soil matrix, although it should be noted that these values are used as tuning parameters rather than intended to reflect any measurable soil properties (Tague and Band, 2001). Groundwater parameters, controlling the amount of water moving from the saturated soil store to groundwater store, are also calibrated. A Monte-Carlo approach is usually employed whereby random parameter values within user-defined ranges are selected and simulated streamflow is assessed against observed flow using an objective function such as Nash-Sutcliffe Efficiency (NSE). This process continues until an optimum set of parameters is achieved (typically thousands of model iterations).

4.2.3 WaSSI

In contrast to the process-oriented approach of RHESSys, WaSSI takes a simplified empirical approach to the estimation of ET and basin water yield. WaSSI has been used to investigate the ecohydrological impacts of climate change, land cover change, and supply/demand dynamics (Sun et al., 2011b). The core of the model is an empirical model for ET developed from flux tower and sapflow observations (Sun et al., 2008, 2011a). ET is predicted as a function of potential evaporation (calculated via Hamon's method (Lu et al., 2005)), LAI, and precipitation. Fluxes are calculated at a monthly time step for eight land cover types and aggregated to

basins according to areal fraction. Initially, WaSSI was developed for 8-digit USGS Hydrologic Units (8-digit HUC), but it has since been downscaled to the 12-digit HUC scale and coupled with an empirical water use efficiency model to simulate carbon dynamics (Sun et al., 2011a). Infiltration, soil storage, and runoff processes are simulated using soil parameters and components of the Sacramento Soil Moisture Accounting Model which allows ET to be constrained by soil moisture.

4.2.4 Climate Scenarios

Daily and monthly series of observed maximum and minimum temperature and precipitation were assembled from NWS Coop stations for the 1961–1990 baseline climate period. Data from two stations were used in this investigation (Fig 4.1). The Chapel Hill station (NWS Coop ID: 311677, 35°54′32″N, 79°04′44″) has a record of minimum and maximum temperature and precipitation from 1891/1/1 to present. The Durham station (NWS Coop ID: 312515, 36°02′33″N, 78°57′45″) has a similarly long record, with the first observation recorded on 1899/3/1. Data from the two stations were used in order to fill intermittent missing data. After verifying no systematic bias between the two stations, the temperature and precipitation records were merged by averaging daily values when both stations had observed data and filling data when only one station recorded data.

Output from two global climate models and a stochastic weather generator were used to construct daily and monthly series of temperature and precipitation for the 2051–2080 future climate period. The third version of the Hadley Center Coupled Model (HADCM3) and the Canadian Centre for Climate Modeling and Analysis' Coupled Global Climate Model version three (CGCM3) were used in this investigation in part because previous versions of these GCMs have been used for other climate impact assessments in the southeastern United States (Burkett et al., 2000; Sun et al., 2000). Gridded model output for temperature and precipitation were retrieved from the WCRP CMIP3 multi-model dataset for the SRES A2 emissions scenario (economic and technological growth are fragmented and regionally oriented) for the 2000–2100 simulation period. Monthly mean values of temperature and precipitation for the model grid cell covering central North Carolina were extracted from the datasets for the

2051–2080 period. Anomalies were constructed relative to the baseline period via comparison to the high resolution global gridded CRUTEM3 product (Brohan et al., 2006). This was done rather than via comparison to the NWS Coop observed values because anomalies calculated from individual stations may not accurately reflect the magnitude of future changes due to mismatches in spatial scale.

HADCM3 and CGCM3 predict similar increases in mean annual temperature in 2051-2080 relative to the baseline period (2.2°C and 2.6°C), but there are differences in the seasonal pattern of change. Whereas the CGCM3 simulated temperature increase is essentially temporally uniform, HADCM3 shows a distinct seasonality favoring much warmer summers and baseline or slightly cooler winters (Fig. 4.2). Mean monthly temperatures calculated from station data were consistently 1.6° higher than the CRUTEM3 values. The HADCM3 model predicts a modest increase in mean annual precipitation (35 mm). Mean annual precipitation is increased by 136 mm under the CGCM3 climate scenario. Both models share a similar pattern of reduced late summer precipitation and increased winter and spring precipitation, although the magnitude of winter and spring increase is much greater for the CGCM3 model than the HADCM3 model. CRUTEM3 and Coop precipitation are generally in good agreement except for late summer months when the Coop values are around 20 mm lower than the CRUTEM3 values.

These monthly climate series and anomalies are sufficient input for the WaSSI model, but RHESSys requires daily series. The challenge of downscaling climate data spatially and temporally is the subject of a large literature (see reviews by Hewitson and Crane (1996); Wilby and Wigley (1997); Xu (1999); Fowler et al. (2007)). Methodologies can broadly be grouped into dynamic modeling and statistical approaches. The former uses the results of coarser scale GCMs to constrain finer scale regional climate models. Statistically based methods include a large variety of techniques which seek to identify relationships between observed data and broader scale patterns and use these empirical relationships to adjust GCM predictions. Statistical approaches are easier to implement and have been shown to perform as well or better than dynamic modeling approaches in a limited number of comparison studies although they tend to underestimate inter-annual variability (Fowler et al., 2007). Among statistical

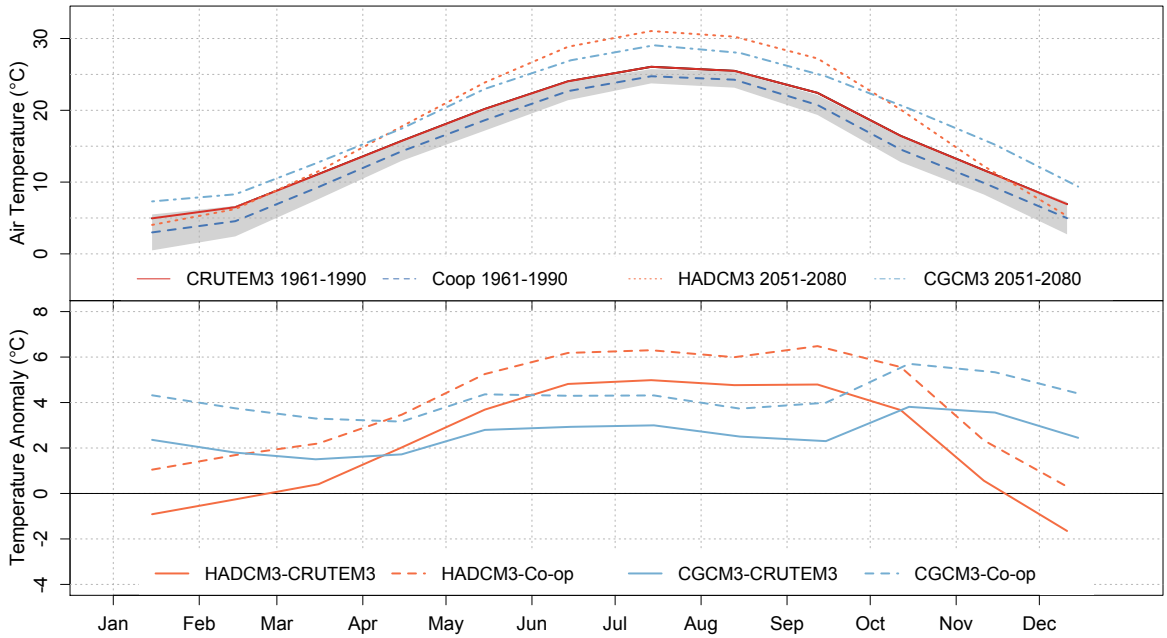

Figure 4.2: Temperature anomalies for HADCM3 and CGCM3 climate models relative to NWS Coop observations (dashed lines) and the CRUTEM3 global dataset (solid lines). Solid area in upper panel indicates one standard deviation around the mean for the NWS Coop data record.

approaches, regression, machine learning, weather typing, and stochastic weather generators are all commonly employed techniques. We chose to use the stochastic weather generator LARS-WG (Semenov and Barrow, 1997) for its proven performance (Semenov et al., 1998), and because weather generation methods of downscaling have been shown to be a reliable statistical method (Wilby and Wigley, 1997). Precipitation is the major variable used by LARS-WG to adjust all other climate variables and simulation of precipitation is based on observed distributions of wet and dry day series. We conditioned LARS-WG using the NWS Coop observed data and generated daily time series of minimum and maximum temperature and precipitation to correspond to the 2051–2080 GCM climate change scenarios.

4.2.5 Land Cover Scenario

In addition to future climate dynamics we also consider a future land cover scenario wherein there is widespread expansion of evergreen forests at the expense of deciduous, agricultural,

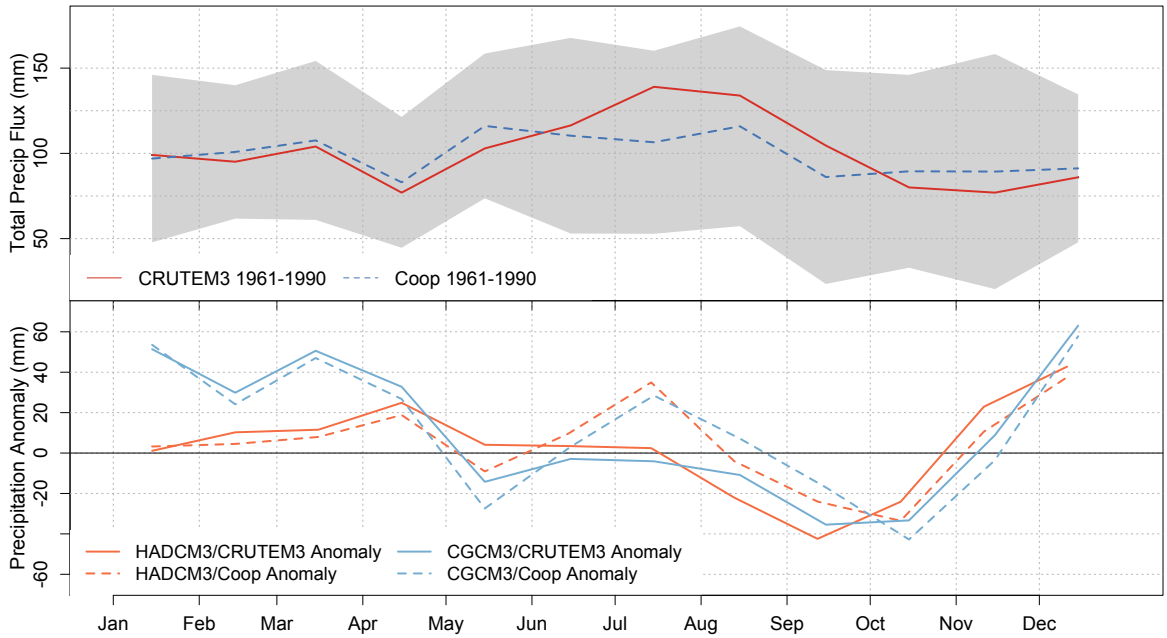

Figure 4.3: Precipitation anomalies for HADCM3 and CGCM3 climate models relative to NWS Coop observations (dashed lines) and the CRUTEM3 global dataset (solid lines). Solid area in upper panel indicates one standard deviation around the mean for the NWS Coop data record.

and pasture areas. This particular land cover scenario, while perhaps not being the most likely, is interesting in several respects. First, production of softwood products, primarily from southern pine species, is a major economic force in the southeast which provides 40% of the national supply (McNulty et al., 1996; Wear and Greis, 2001). Furthermore, the area of planted pine stands in the southeast is increasing and accounts for nearly half of the total pine forest area in the southeast (Wear and Greis, 2001; McGrath et al., 2004). Additionally, large-scale conversions from natural deciduous to managed evergreen stands are interesting because they have the potential to alter water balances through variable ecological water use. The consequences of such conversions have long been recognized , but have received increasing attention recently due to suggestions that increased pine afforestation may have benefits for climate mitigation and biofuel production (Jackson et al., 2005, 2007; Jackson and Baker, 2010). These recent investigations highlight the negative impacts of these types of conversions on water availability, particularly in already water stressed areas.

In order to isolate the effect of increased pine area on the hydrologic cycle of the Eno river we developed a hypothetical future land cover map by iteratively growing regions of existing evergreen forest cover at the expense of all other vegetation types. We began with the land cover maps generated in Chapter 3. In this way, only vegetation composition changes are considered, and the overall vegetated area and relative frequencies of other land cover types remain constant. We also prescribed a 30% increase of LAI in newly established pine areas under the assumption that they would be intensively managed and thus be able to support higher productivity. The starting map was a form of the previously generated land cover map (Chapter 3) adapted to broad, hydrologically significant land cover classes: deciduous vegetation, evergreen vegetation, grass/agriculture/pasture, and not vegetated. The contemporary basin proportion of 6% evergreen forest was increased in the future scenario to 37% with an associated reduction in deciduous forest from 61% to 34%, and 17% to 13% for grass/agriculture/pasture.

4.2.6 Model Parameterization, Calibration, and Simulation

Major inputs to RHESSys include the previously described daily climate series, maps of leaf area index, land cover, and soils, topographic information, and a collection of vegetation and soil parameters. We assembled these inputs through a variety of methods and organized the spatial data using the GRASS GIS (GRASS Development Team, 2012). A 1-arc second resolution National Elevation Dataset digital elevation model (DEM) was subset to the study area, reprojected to UTM coordinates, and resampled to 30 m spatial resolution. A sink filled version of the DEM and derivative products (e.g. slope, aspect, flow accumulation) were used to delineate the Eno basin from the USGS gauges at the outlet above Falls Lake and at Sevenmile Creek (4.1). Hillslopes were defined based on area thresholds selected interactively to correspond to streams digitized from USGS 1:24000 Quadrangles. Soils texture data were obtained from SSURGO maps and collapsed to broad categories (e.g. “clay”, “loam”, “sandy-loam”, etc.) so that RHESSys required soil physical properties could be derived from literature values (Clapp and Hornberger, 1978). Vegetation related parameters such as maximum g_s, optimum photosynthetic temperature, and phenological information were gathered from literature reported values (White et al., 2000) and mapped to the previously described adapted land cover

maps. The LAI estimation method described in Chapter 2 was modified to account for the lack of analogous high temporal resolution imagery over the entire Eno basin and used to initialize RHESSys canopy carbon stores. RHESSys patches were assigned as individual 30 m DEM grid cells.

Explicit routing is computationally intensive and requires special considerations when simulating at the spatial scales of this investigation. The typical RHESSys calibration procedure relies on many thousands of model runs to identify an optimum parameter set, but this amount of computation was infeasible for the entire Eno basin. Instead, we chose to calibrate RHESSys using the smaller Sevenmile Creek subbasin and assumed the parameters would be applicable to the entire basin. The Sevenmile Creek watershed is located in the southwest corner of the Eno basin, is approximately one-tenth the size of the Eno (36.2 km^2), and has land cover proportions approximately equal to those of the larger basin. The twelve water year period between 1989 and 2000 was used as the calibration period because it includes a diversity of flows and precipitation events. Observed streamflow from a USGS gauge on Sevenmile Creek (USGS ID: 02084909, 36°03′56″N, 79°08′39″W, record period: 1981/6/24–2004/10/21) was used to calculate NSE for actual and log-transformed flows at daily and monthly time steps. Over 5000 simulations with unique values of K_{sat0}, m, and groundwater parameters were performed on a cluster computing facility at the University of North Carolina. Parameter ranges were individually restricted over successive model runs based on observed patterns of model skill in order to converge on an optimum parameter set.

Computational limitations require further considerations to scale the model up to the entire Eno Basin. We opted for an "embarassingly parallel" implementation whereby the Eno basin is subdivided into smaller basins which are individually simulated and the results aggregated using areally-weighted averaging. This approach allowed for an efficient implementation on a research cluster computing facility. The optimal parameter set identified on the Sevenmile Creek calibration basin were assumed to be optimal for the entire Eno River basin and extended to 11 subbasins ranging in area from 73.2 km^2 to 13.0 km^2.

Four 12-digit HUCs comprise the Eno River basin (Fig. 4.1). Land cover proportions, LAI, and soils data were extracted for each 12-digit HUC and used to parameterize four

individual WaSSI models. Results from each subbasin were aggregated as before using areally-weighted averaging of streamflow and ET. No attempt at calibration of the model functions for ET, streamflow, or soil moisture was conducted for WaSSI simulations. Instead, we used the existing model configuration which reflects global relationships between water fluxes and meteorological driving variables derived from flux tower data.

Simulations were performed for all six permutations of the climate change and land cover scenarios using both RHESSys and WaSSI models for the Eno basin. RHESSys utilized the daily observed climate series, and the daily future climate series developed with the LARS-WG stochastic weather generator as meteorological forcing data whereas WaSSI used the monthly versions of these series. Flow observations from a USGS stream gauge on the Eno, located just upstream of the river's outlet in Falls Lake (USGS ID: 0208570, 36°04′20″N, 78°54′28″W), was used to asses the performance of both models over the baseline 1962–1990 period. NSE and log-NSE were used to assess the skill of the models in reproducing observed patterns of daily and monthly streamflow across the basin. The individual and combined effects of climate and land cover change were assessed by comparing mean monthly and annual simulated streamflow and ET. Relative model performance was assessed over the baseline period through correlation analysis and comparison of simulated values.

4.3 Results

4.3.1 RHESSys Calibration

Maximum NSE and log-NSE (0.53 and 0.57, resp.) were observed for a Sevenmile Creek simulation with $m = 1.44$, $K_{sat0} = 130.4$, and the multipliers for water moving from the saturated to groundwater stores and groundwater stores to the stream at 0.009 and 0.61, respectively. Monthly NSE was higher than daily NSE for both raw and log-transformed flows (0.79 and 0.66, resp.) indicating that the model does a slightly better job simulating low flows than peak flows. Figure 4.4 indicates that the calibrated RHESSys model generally replicates the magnitude and timing of flow events and the characters of the rising and recessional hydrograph limbs. Extremely low flows are over-predicted but the overall magnitude of the

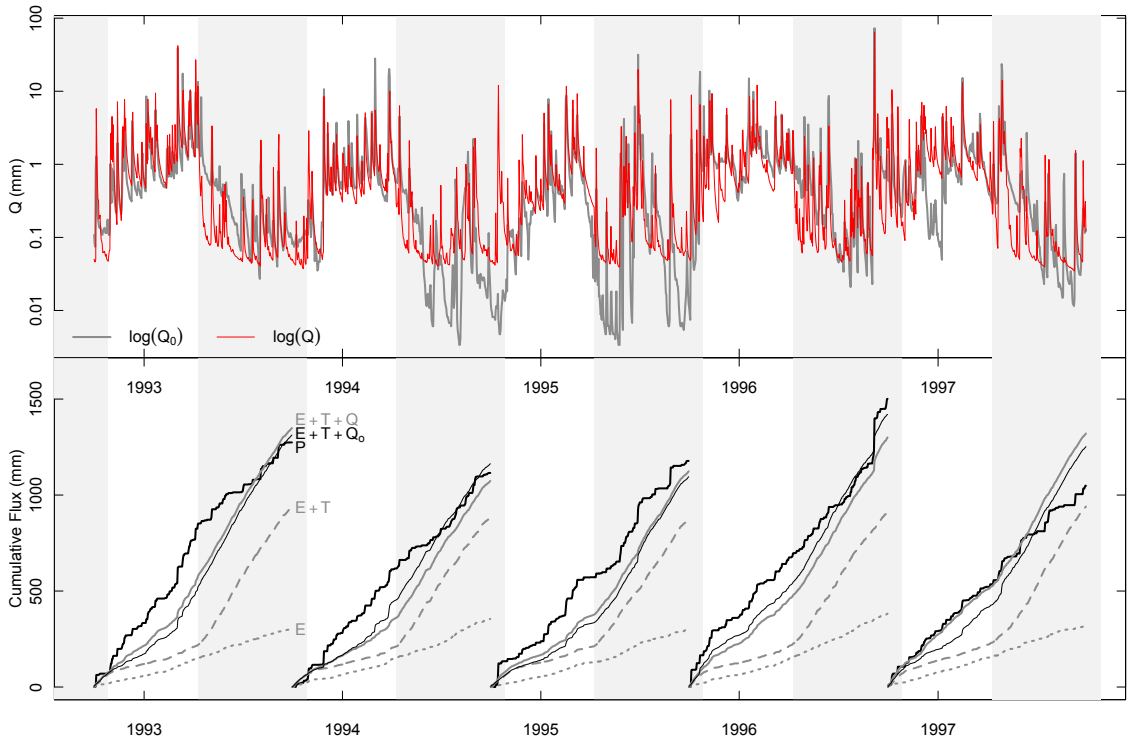

Figure 4.4: RHESSys results for Sevenmile Creek for five water years during the calibration period. Upper panel depicts observed and simulated daily log-transformed streamflow. Lower panel depicts cumulative simulated and observed water year fluxes.

differences are small. Peak flows, however, are usually underestimated. Water year cumulative fluxes indicate low inter-annual variability in ET and overall good agreement between observed and simulated water year cumulative streamflow. Streamflow is nearly balanced by ET and streamflow at the water year temporal scale except in 1996–1997 when simulated and observed streamflow and ET significantly exceed the precipitation input.

4.3.2 RHESSys and WaSSI Simulation Results

RHESSys simulated mean annual streamflow was 347 mm for the baseline climate period under contemporary land cover conditions. Mean annual streamflow was increased by 24.7 and 95.3 mm under the HADCM3 and CGCM3 climate scenarios, respectively, with land cover fixed at contemporary conditions (Fig. 4.5, and Table 4.1). These increases are associated with the significant increase in winter and early-spring precipitation predicted under these scenarios. In fact, modest reductions in streamflow were observed for most summer months associated

with decreased summer precipitation and increased water vapor flux due to increased energy available for evaporation. The variability of streamflow was decreased under the climate change scenarios with overall less years with very low flows, and fewer years with exceptionally high flows, while the ET variability was constant across scenarios.

Whereas annual increases in precipitation under both climate scenarios resulted in increased streamflow, changes in vegetation composition to an increased pine forest condition (with attendant increases in LAI) led to a reduction in simulated annual streamflow. Under the baseline climate scenario, the increase in pine area led to a 39.4 mm reduction in streamflow, and a 12.6 mm reduction under the HADCM3 climate (Table 4.1). The increase in streamflow accompanying the large increase in precipitation predicted by the CGCM3 climate model was reduced to 47.7 mm under the pine land cover scenario, a smaller increase than the 95.3 mm simulated under contemporary land cover (Table 4.1). In general, the two climate scenarios investigated here led to increases in simulated streamflow due to increased precipitation, while the change to increased pine area led to reductions with the net effect depending on the relative magnitudes.

Climate and land cover changes both increased simulated mean annual ET, though the magnitude of the increases varied. Under the baseline climate, mean annual simulated ET increased by 40.9 mm when the land cover was modified to an increased pine condition (Table 4.2). Under the HADCM3 climate, ET was increased by 32.0 and 69.6 mm, whereas under the CGCM3 climate the increases were 49.6 and 97.6 mm under contemporary and pine land cover conditions, respectively (Table 4.2). These increases in ET may be attributed to increased precipitation (greater evaporation from nonvegetated surfaces and canopy intercepted water), increased air temperature, and increased vapor pressure deficit (associated with higher temperatures).

At the monthly scale, the largest increases in simulated mean streamflow occurred in December, January, and March under the CGCM3 climate change scenario (Fig. 4.6). Patterns of streamflow change were similar across all months for both climate scenarios, but the magnitude of simulated changes were consistently higher under the CGCM3 climate scenario. Reductions

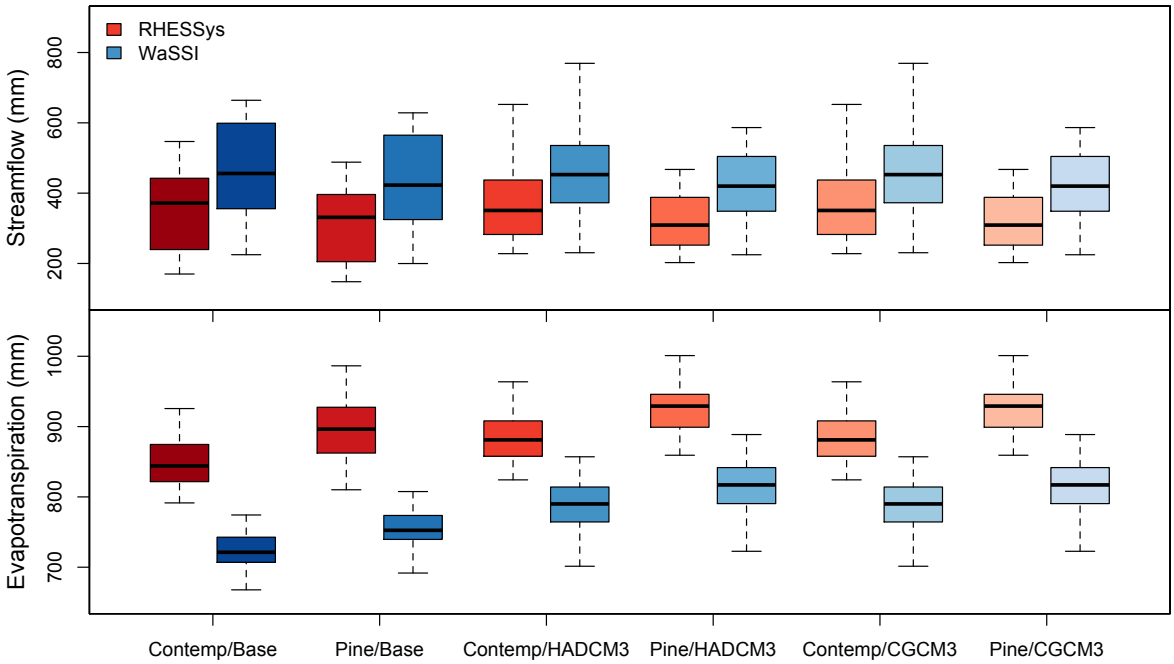

Figure 4.5: Boxplots of annual simulated streamflow and ET for the RHESSys and WaSSI models over all six permutations of climate and land cover change

	RHESSys		WaSSI	
	Contemp	Pine	Contemp	Pine
Base	–	-39.4	–	-29.6
HADCM	24.7	-12.6	7.5	-19.4
CGCM	95.3	47.7	90.8	62.6

Table 4.1: Simulated change in mean annual streamflow (mm yr^{-1}) relative to baseline climate and contemporary land cover conditions. Positive values indicate that the simulated quantity was greater under the given land-cover/climate treatment than the baseline climate and contemporary land-cover conditions.

	RHESSys		WaSSI	
	Contemp	Pine	Contemp	Pine
Base	–	40.9	–	29.6
HADCM	32.0	69.6	80.7	107.7
CGCM	49.6	97.6	88.8	116.5

Table 4.2: Simulated change in mean annual evapotranspiration (mm yr^{-1}) relative to baseline climate and contemporary land cover conditions. Positive values indicate that the simulated quantity was greater under the given land-cover/climate treatment than the baseline climate and contemporary land-cover conditions.

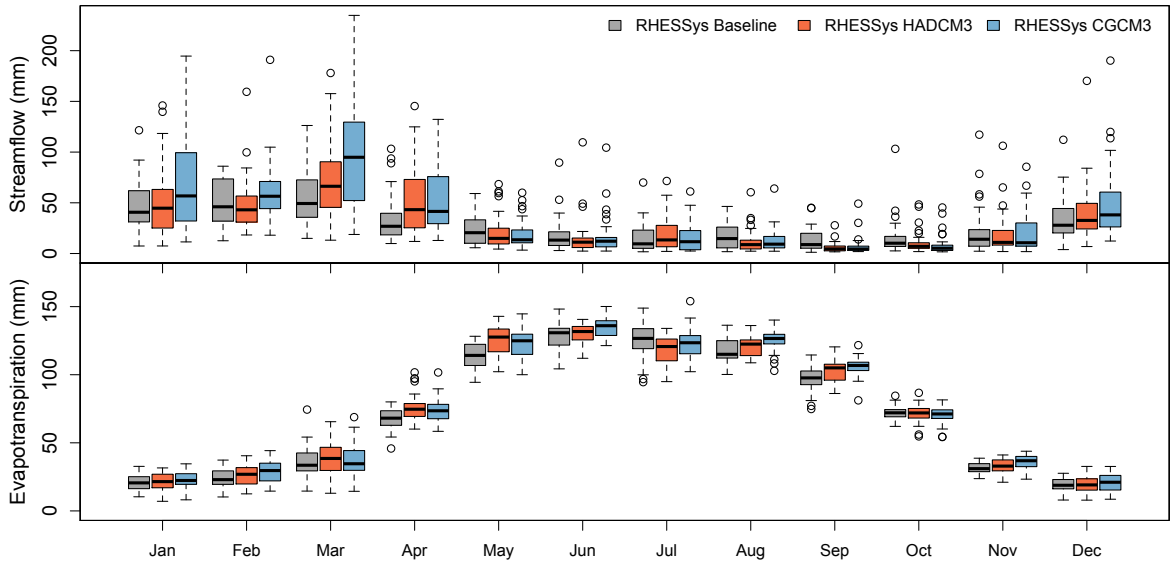

Figure 4.6: RHESSys simulated monthly streamflow and ET for three climate scenarios and contemporary land cover.

in monthly mean streamflow, and streamflow variability were observed for summer months under both HADCM3 and CGCM3 climates. Monthly patterns of streamflow change were similar under contemporary and enhanced pine land cover scenarios (Fig. 4.7), but the magnitudes of streamflow increases are reduced under the pine land cover scenario, and reductions in mean monthly streamflow are larger. Increases in mean monthly ET are simulated across all months except July and October for both HADCM3 and CGCM3 climate scenarios (mean monthly ET enhancement is 4% under HADCM3 and 7.5% under CGCM3) and the magnitudes of the increases are greatest under the pine land cover scenario.

WaSSI simulated mean annual streamflow showed a similar response to varying climate and land cover as the RHESSys simulations. The simulated reduction in mean annual streamflow in response to increased pine area was 29.6 mm, whereas increases of 7.5 and 90.8 mm were simulated for contemporary land cover and HADCM3 and CGCM3 climate scenarios, respectively (Table 4.1). Under the increased pine land cover condition streamflow was reduced by 19.4 mm under the HADCM3 climate, and increased by 62.6 mm for the CGCM3 climate. Annual streamflow variability was increased for climate change scenarios with contemporary land cover, and reduced or constant relative to the contemporary land cover condition for the pine

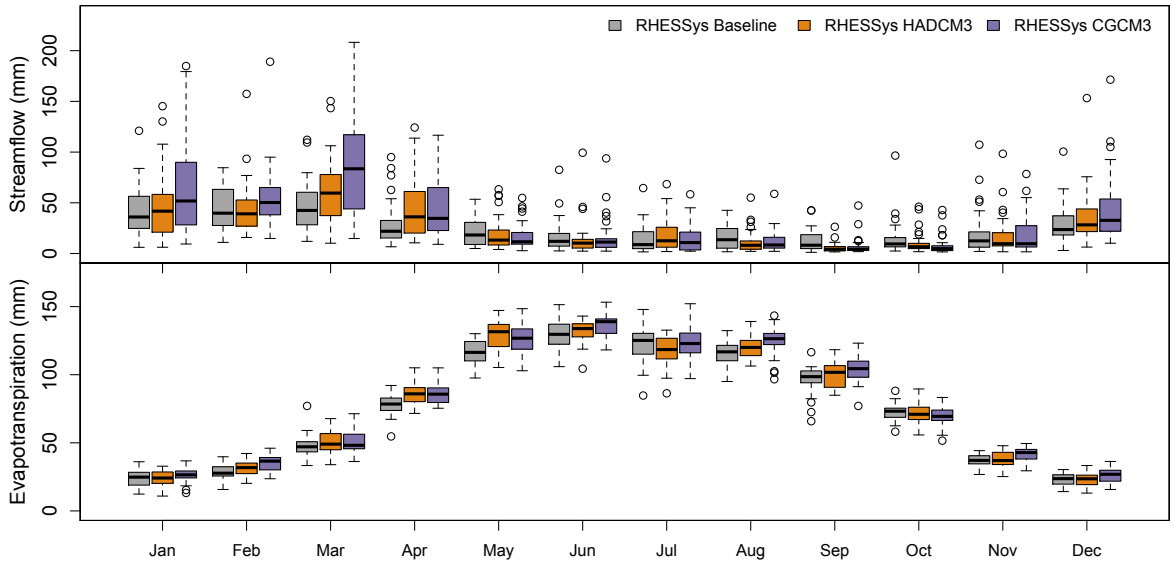

Figure 4.7: RHESSys simulated monthly streamflow and ET for three climate scenarios and the increased pine land cover scenario.

land cover scenarios. It should be noted that while the magnitudes of simulated mean annual streamflow differed between WaSSI and RHESSys, the responses to land cover and climate were consistent in sign between the models, and the magnitudes of the impacts were similar. Similar to the RHESSys simulated results, WaSSI simulated mean annual ET increased under every land cover and climate condition tested, and the increase was greatest under the pine land cover condition and the CGCM3 climate (Table 4.2).

WaSSI results at the monthly scale had a similar pattern to the RHESSys results (Figures 4.8 and 4.9). Relative increases in monthly mean streamflow were greatest for the winter months while summer months had modestly reduced streamflow under both climate scenarios. September and October mean streamflow were significantly reduced under climate change scenarios due reduced precipitation during these months. Significant increases in ET were simulated by WaSSI under both climate scenarios for all months except October and November which saw modest reductions. Under the enhanced pine land cover scenario WaSSI simulates increased ET in all months under the baseline climate scenario, and larger increases under both climate change scenarios except for the month of October for which there is a modest reduction in simulated monthly mean ET relative to the contemporary land cover condition.

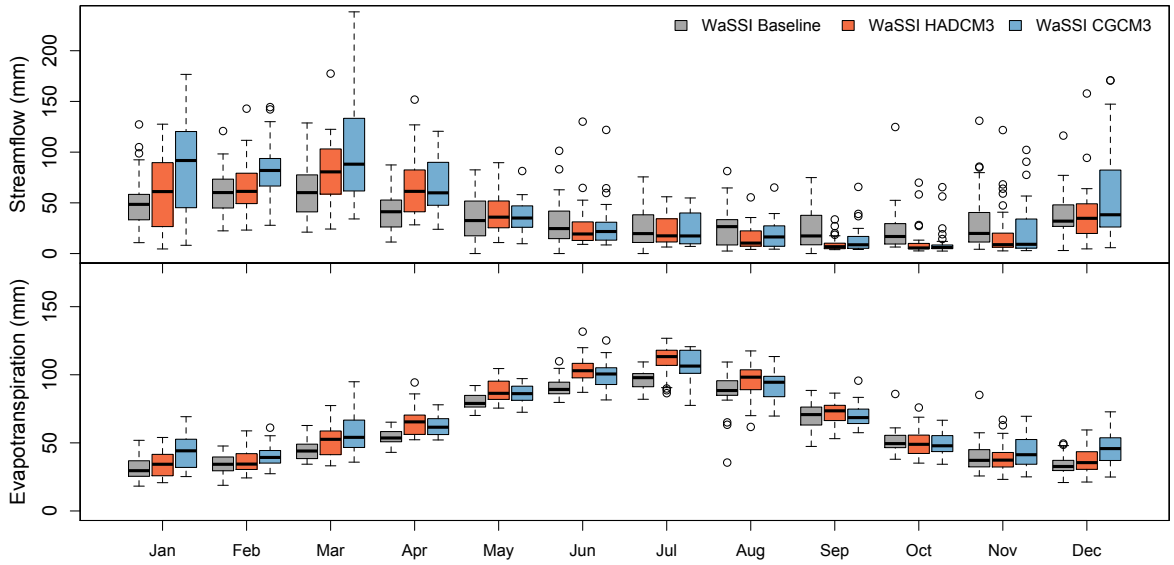

Figure 4.8: WaSSI simulated monthly streamflow and ET for three climate scenarios and contemporary land cover.

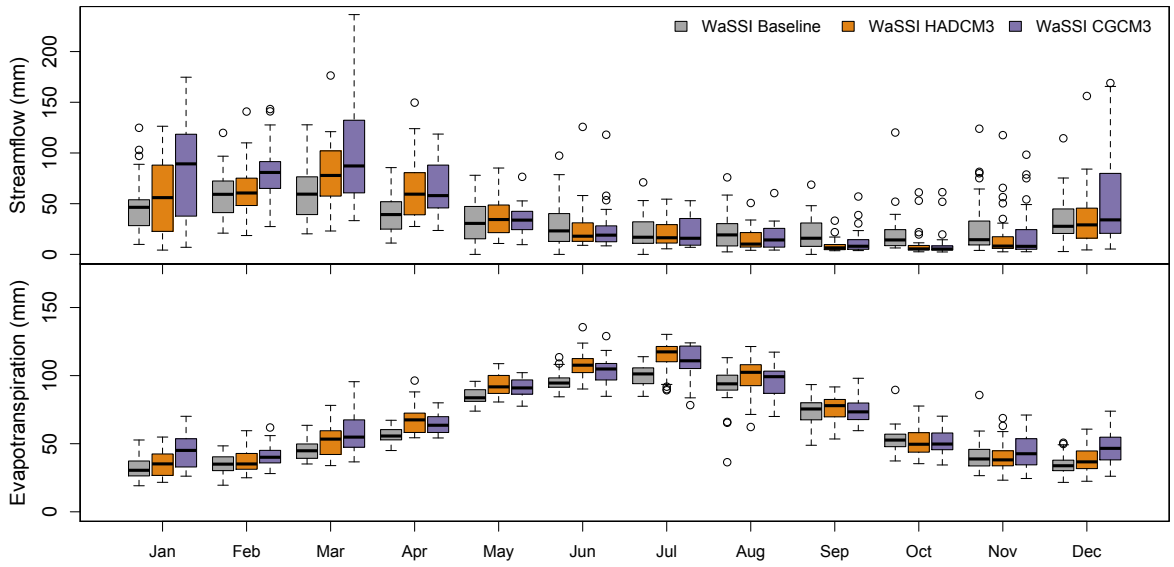

Figure 4.9: WaSSI simulated monthly streamflow and ET for three climate scenarios and the increased pine land cover scenario.

Following Tague et al. (2009) we assessed changes in the occurrence of summer low flows under the various climate and land cover scenarios. A threshold was determined as the number of years in which August streamflow was less than or equal to the lower quartile value under the baseline climate and contemporary land cover conditions. Occurrences of August streamflow less than this threshold were calculated for each model run. Under baseline climate and contemporary land cover, low August flows occurred in 26.7% of RHESSys and WaSSI simulated years. Relative occurrences of low flows increased to 30% of RHESSys simulated years under the HADCM3 climate scenario and contemporary land cover, and remained constant at 26.7% for the CGCM3 scenario. The land cover change alone resulted in an increase in August low flow proportion to 30% for the RHESSys results. WaSSI results indicate an increase in simulated years with low August flows from 26.7% to 33.3% under the HADCM3 and 30% under the CGCM3 climate scenario for both contemporary and enhanced pine land cover scenarios.

4.3.3 RHESSys and WaSSI Comparison

Monthly NSE and log-NSE for the Eno Basin RHESSys simulation, over the entire baseline simulation period were 0.80 and 0.78, respectively. WaSSI NSE and log-NSE over this period were 0.49 and 0.41. On average, WaSSI annual simulated streamflow is 110 mm higher than RHESSys simulations, and WaSSI simulated annual ET is 147 mm lower (Figures 4.11 and 4.12). Correlation analysis between simulated results for the baseline climate and contemporary land cover indicate a slight positive bias for WaSSI results relative to RHESSys across the full range of simulated flows (Table 4.3, and Fig. 4.10). Seasonally, the mismatch is greatest for fall months where WaSSI indicates monthly streamflows that are on average 16 mm higher than the RHESSys results. Correlations between RHESSys and WaSSI simulated monthly ET are high at the annual time scale, but low during the winter and summer months. In general, WaSSI estimated ET is higher than RHESSys during months with low ET, and lower during months with high ET.

	$\beta_{0,Q}$	$\beta_{1,Q}$	${R^2}_Q$	$\beta_{0,ET}$	$\beta_{1,ET}$	${R^2}_{ET}$
DJF	8.77	0.98	0.69	18.07	0.73	0.33
MAM	16.24	0.85	0.78	28.06	0.44	0.81
JJA	9.52	1.14	0.74	95.53	-0.04	< 0.01
SON	6.52	1.14	0.84	25.47	0.43	0.54
Annual	10.57	0.97	0.79	22.29	0.53	0.83

Table 4.3: Seasonal and annual relationship between RHESSys and WaSSI simulated monthly streamflow (Q) and ET (ET) for observed baseline climate and contemporary land cover. Values are the intercept, slope, and coefficient of determination (β_0, β_1, and R^2) for the linear regression: $\text{WaSSI}_{Q/ET} = \beta_{0,Q/ET} + \beta_{1,Q/ET} \cdot \text{RHESSys}_{Q/ET}$ All estimated parameters are significant at $p < 0.001$ except $\beta_{1,ET}$ for summer months (JJA) where $p > 0.1$.

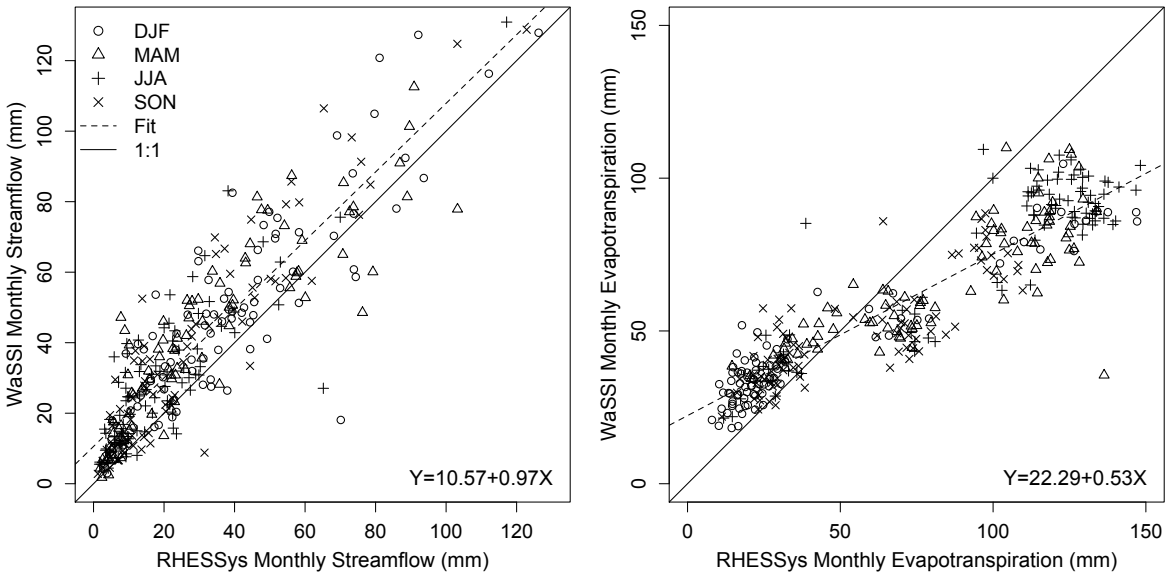

Figure 4.10: Relationship between RHESSys and WaSSI simulated monthly streamflow and ET for observed baseline climate and contemporary land cover with linear fit.

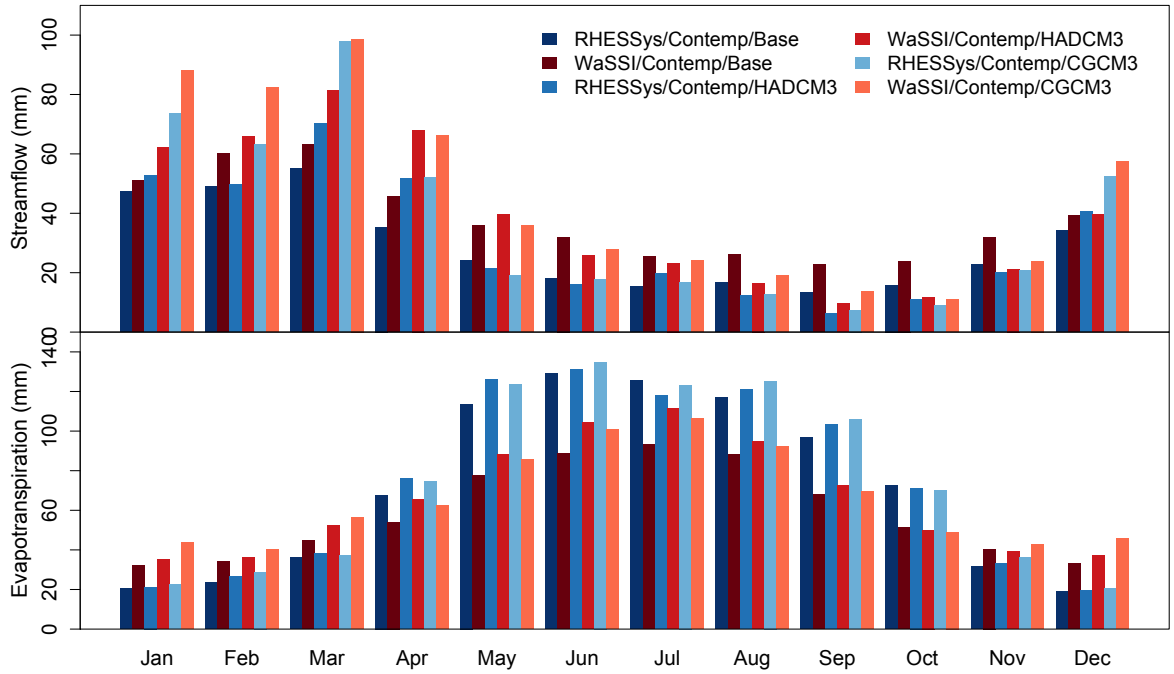

Figure 4.11: RHESSys and WaSSI mean monthly simulated streamflow and ET across for contemporary land cover and each climate scenario.

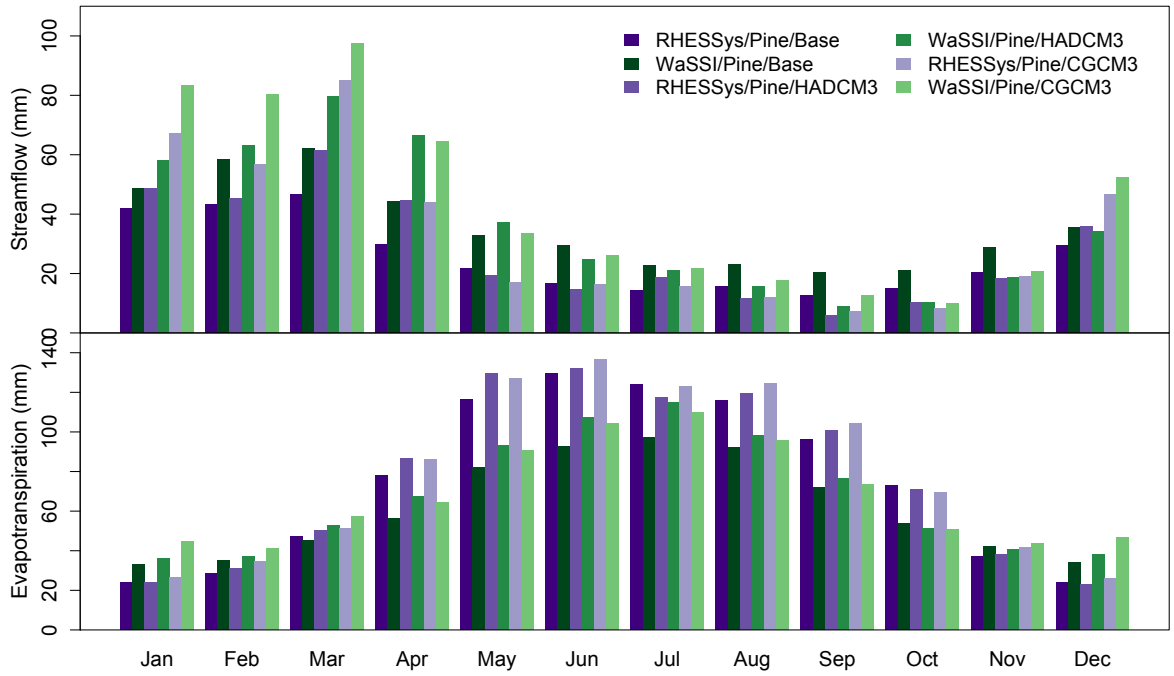

Figure 4.12: RHESSys and WaSSI mean monthly simulated streamflow and ET across for the increased pine land cover scenario and each climate scenario.

4.4 Discussion

4.4.1 The Effects of Climate Change and Land Cover Change

Although these results do not constitute a forecast, these experiments indicate that future climate and/or land cover regimes could significantly alter streamflow and ET patterns in the Eno River basin. Model simulations highlight the important role that vegetation composition plays in this mostly forested watershed. Significant reductions in streamflow were observed to result from enhanced ET when pine area was increased. However, these decreases are offset by increased streamflow resulting from climate change driven precipitation increases, so that the net effect under both climate and land cover changes depends on the magnitude of the precipitation change. For instance, the relatively modest increase in precipitation under the HADCM3 climate scenario was insufficient to offset the impact of increased pine area and streamflow was decreased, whereas streamflow increased under the CGCM3 scenario with its more substantial increase in precipitation. Although temperature increases are associated with higher evaporation and transpiration, changes in precipitation dominate the simulated patterns of streamflow in the Eno. This is due to the fact that even though ET increases with available energy, the magnitude of precipitation changes are larger and dominate the streamflow response. These trends are in line with what would be expected as part of a synoptic scale acceleration of the hydrologic cycle. Furthermore, increased atmospheric water vapor due to increased ET may reinforce this trend leading to still greater precipitation. Importantly, the predicted changes under HADCM3 and CGCM3 scenarios would introduce an increased precipitation seasonality favoring drier growing seasons (particularly late summer), and wetter dormant periods.

Indeed, the occurrence of late summer low flows were predicted to increase across all simulations associated with decreased precipitation inputs and increased late summer ET. While the magnitude of late summer streamflow reductions were insufficient to balance the dormant period increases (leading to higher annual streamflows under climate change scenarios), the trend has important implications for water resource availability in the Eno. Summer flows are already relatively low due primarily to hot summers and abundant vegetation, and climate

changes which reduce summer precipitation and increase temperature may exacerbate the situation leading to late season water stress in vegetation and perhaps increased mortality. The climate changes considered here do not indicate that decreased summer precipitation limits vegetation productivity. In fact, there is a simulated decrease in summer evaporation and increase in transpiration for RHESSys climate change simulations. However, there is a point at which soil moisture becomes limiting and transpiration and productivity are reduced. Summer temperatures that are higher than the scenarios considered here, and/or greater reductions in summer precipitation could transition the system towards a more water-limited regime wherein late summer productivity would decrease with possible increases in mortality. Streamflow was most reduced under the increased pine land cover scenario and further increases in these areas, particularly when they replace deciduous and sparse vegetation, could similarly move the basin towards increasing water stress.

Previous studies have noted the insensitivity of temperate forest ET to inter-annual variation in precipitation (Roberts, 1983; Phillips and Oren, 2001; Oishi et al., 2010). While this holds for deciduous forest, many pine stands in the southeast indicate tighter coupling with climatic drivers of ET (Stoy et al., 2006). Hydrologically, the impact of these phenomenon is a strong dependence of streamflow on precipitation inputs, rather than plant water use withdrawals. Our results indicate an increased correlation between monthly precipitation and simulated ET under the pine land cover scenario relative to contemporary land cover conditions. This trend is partly explained by greater evaporation of canopy intercepted water due to enhanced LAI, and, in climate change scenarios, increased winter evaporation associated with increased temperature and precipitation. However, this trend may indicate a greater coupling between precipitation inputs and ecological processes in the basin associated with the relative increase in moisture sensitive vegetation.

4.4.2 Relative Performance of RHESSys and WaSSI

RHESSys performed better than WaSSI in replicating the observed patterns of basin monthly streamflow over the baseline period. The patterns of streamflow and ET response to climate and land cover changes were similar for both models, however, strengthening our confidence

in the signs, if not the magnitudes, of the predicted changes. The costs of including detailed process representation and explicit flow routing in RHESSys simulations are much greater data and computational requirements. RHESSys requires not only daily series of climate data, but a multitude of environmental data and parameter sets, whereas the WaSSI model can be run with monthly climate series and relatively less and easier to assemble input data. This is an attractive feature of the WaSSI model, particularly for assessing climate impacts using GCM results which are usually reported at monthly time steps. However, the empirical approach of WaSSI has important limitations. Most importantly, the relations between ET and predictor variables established from observed flux tower and sapflow data may not be constant in future climate regimes. For instance, a large literature has reported that water use efficiency may increase in atmospheres with increased CO_2 concentration (Field et al., 1995; Betts et al., 2007; Katul et al., 2009). These types of ecophysiological changes may invalidate the relationships established under historic conditions. Accounting for these types of changes is the primary reason that process-based ecohydrological models may be preferred for assessing future climate and land cover impacts.

Aside from differences in model structure, the higher performance of RHESSys in replicating observed streamflow may be partially attributed to the fact that, in contrast to WaSSI, the RHESSys model is calibrated over thousands of iterations with observed streamflow data. Though the calibrated parameters are meant to account for unmeasurable properties of the soil matrix, mainly macropores and preferential flowpaths, in practice they act as tuning parameters which better match simulated to observed streamflow. It is likely that calibration of WaSSI to the Eno River basin would result in improved performance. The most straightforward way to accomplish this calibration would be to tailor the empirical ET equation to data observed in a particular watershed rather than from geographically diverse lumped data. Likewise, multiple empirical ET equations could be used for specific vegetation types in watersheds where those differences are important. As used in this investigation, a single ET relation is used for all forested vegetation types and hydrological differences are assumed to be accounted for by LAI alone. While this assumption is ideal for capturing ecological variability at the large-scale applications WaSSI was designed for, improvements in local applications are likely

to be realized with vegetation-specific relations developed with local or regional data.

4.4.3 Limitations and Future Improvements

This investigation focused on isolating the individual and combined effects of changes in mean temperature and precipitation and land cover change on hydrologic processes in the Eno. While changes in long-term average temperature and precipitation have important environmental consequences, there are a wide variety of additional effects that were not considered in this investigation. For example, we chose to keep atmospheric CO_2 concentrations constant throughout our simulations rather than varying the ambient concentrations in accordance with specific scenarios. Though we recognize the importance of CO_2 concentrations to the processes investigated here, we made this choice in order to more clearly assess the isolated effects of land cover, temperature, and precipitation drivers. Increasing CO_2 concentrations may increase plant water use efficiency and alter the site-climate relationships observed historically, although at many sites the increase in water use efficiency may be offset by increases in LAI so that the total vegetated water use remains constant (Drake et al., 1997; Field et al., 1995; Betts et al., 2007; Katul et al., 2009). Simulating these processes would require a modified approach to simulation that incorporates dynamic vegetation growth, and a modification to the Jarvis stomatal conductance model (e.g. Tague et al. (2009)). Changes in temperature and precipitation variability, and differential changes in maximum and minimum temperature were also not considered in this investigation, although these quantities are likely to change in the future along with their mean values.

We considered only on land cover scenario, and this scenario included only changes in vegetation composition and not changes in overall vegetation abundance, or changes in other land cover types such as increased impervious surface. While the increased pine forest scenario considered here is interesting with respect to spatiotemporal soil-moisture/vegetation interactions, carbon sequestration, and climate mitigation opportunities, our choice of this scenario should not be interpreted as an implication that this particular scenario is likely to occur in the Eno. Instead, this scenario is useful in understanding the role that vegetation functional types

play in structuring the Eno River water cycle, and represents a relatively extreme endmember along the spectrum of likely future land cover changes. More realistic future projections of water availability should rely on land cover projections that are constrained by economic data. A variety of such models have been developed in the literature (e.g. the CLUE-S model of Verburg et al. (1999)). Coupling such models with RHESSys and WaSSI would enable the models to not only investigate probable future change scenarios, but also the transient dynamics accompanying the changes.

4.5 Conclusions

This investigation sought to assess the individual and combined impacts of climate and land cover change on streamflow and ET in the Eno River basin in central North Carolina. Additionally, we sought to assess the relative performance of two ecohydrologic models with very different structural approaches. Whereas RHESSys is a detailed, process-oriented simulation system offering explicit routing of soil moisture and physically-based submodels describing assimilation and ET, WaSSI is a mostly empirical model developed from a large collection of *in situ* measurements from eddy covariance towers and sapflow measurements. Models were parameterized using an approach that integrated improved remote sensing techniques (to map LAI and land cover) with literature reported values of soil and vegetation physical properties. We considered a baseline climate period (1961-1990) with observations obtained from NWS Coop stations near the basin, and two different climate change scenarios (2051–2080) derived from GCM output under the IPCC SRES A2 emissions scenario. The HADCM3 model predicts large increases in average temperature during the summer months, moderate to no warming during other seasons, and an overall modest increase in precipitation with reductions in late summer and fall precipitation and increases in winter and spring. In contrast, the CGCM3 model indicates a more uniform increase in temperature across the year and similar patterns of precipitation, although the overall magnitude of precipitation increase is greater than the HADCM3 model, particularly during the spring. We also considered a future land cover scenario in which evergreen forest was expanded from it's contemporary proportion of 6% of the

basin area to 37% by growing into areas of deciduous forest and grass/pasture/agriculture.

Our results indicate that both climate and land cover changes significantly impact the basin hydrologic cycle. Annual streamflow was increased across all simulations which featured a climate change and contemporary land cover, due to increased precipitation. While increased pine area reduced mean annual streamflow, this reduction was offset by increased precipitation under the CGCM3 scenario resulting in a net streamflow increase. Streamflow increases were greatest during winter and spring months and under the CGCM3 scenario. Summer streamflows were significantly attenuated due to decreases in late summer precipitation and increases in ET. The probability of August streamflows falling below the baseline lower quartile level was increased for climate change scenarios and indicates that future water availability may be seasonally restricted. ET increased with increasing temperature and precipitation associated with climate change, and increases were greatest under the pine future land cover scenario. Land cover change alone led to modest reductions in streamflow as more soil moisture was used for transpiration. RHESSys better replicated the observed patterns of monthly streamflow than did WaSSI (NSE=0.80 and NSE=0.49, resp.). WaSSI predicted annual streamflows that were 110 mm higher on average than RHESSys predictions, and WaSSI simulated ET was on average 147 mm lower than RHESSys.

Taken together, our results indicate that climate change and land cover change may result in significant perturbations of the existing water cycle in the Eno River basin. Specifically, if precipitation seasonality is altered in the ways predicted by the CGCM3 and HADCM3 models, then the region is likely to be increasingly water stressed during the summer months despite an increase in annual precipitation. Increased pine area can exacerbate this stress by increased ET and further reductions in water availability. We stress that while these results are useful for investigating relative changes in water balance components, and assessing how climate and land cover drivers contribute to structuring vegetation-water interactions, they are not intended to provide reliable quantitative estimates of changes in water fluxes. Future progress can be made by considering transient climate and land cover dynamics, consideration of alternate change scenarios, investigation of CO_2 concentration changes, and coupling land cover models to the ecohydrologic simulators.

Chapter 5
Conclusions

Climate and land cover changes in the coming century will have important impacts on local, regional, and global water cycles with implications for freshwater availability. Previous research has indicated that the effects of these changes will be most strongly felt in regions that are already water stressed, and in regions where there are increasing demands on freshwater resources associated with growing and developing human populations. Population growth in the southeastern United States is more rapid than elsewhere in the United States, highlighting the importance of reliably managing existing supplies to meet increased demand into the future in this region. Coupled ecosystem simulation investigations are necessary in order to predict the ecological and hydrological response of basins to dynamic climate and landscape drivers of change. This investigation utilized an integrated remote sensing and ecosystem simulation approach to understanding the impacts of climate and land cover change on the hydrology of the Eno River basin in central North Carolina. The principal objectives of our investigation were threefold: 1) improve remote sensing based methods of mapping LAI to address existing shortcomings related to estimating LAI in high biomass stands and characterizing temporal patterns of vegetation evolution, 2) develop a method of efficiently utilizing large archives of remotely sensed images to obtain accurate and consistent maps of land cover and land cover change, and 3) assess the long-term impacts of specific climate and land cover changes on streamflow and ET in the Eno River basin, and contrast the performance of two structurally different approaches to simulating basin hydrological processes.

I first investigated the potential of a multi-sensor information fusion approach to LAI mapping to overcome acknowledged remote sensing methodological deficiencies. The bulk of existing methods adopt an empirical approach which seeks to develop relationships between ground measurements of LAI and remotely sensed predictors such as spectral vegetation indices. These methods have been widely employed with varying degrees of success. There are three principal limitations to this approach. First, SVI tend to saturate at moderate to high biomass levels which restricts the predictable range of LAI and lowers the certainty of LAI estimates in densely vegetated stands. Second, there is little consensus regarding which SVI predictors should be used and what form the empirical relation should take. Third, even the most successful empirical relations are only capable of providing maps of LAI at a single point in time, and thus are incapable of supplying information regarding spatiotemporal variability.

The approach developed in this investigation addresses and overcomes each of these limitations by combining information from multiple satellite based sensors in a modeling framework that is capable of supplying land cover maps at an arbitrary temporal interval. The most significant contribution of this study was to demonstrate that spatial information (texture) from very high resolution remotely sensed images are significant predictors of LAI in closed

canopy forests, and that these metrics may be used along with conventional spectral predictors to overcome the problem of SVI saturation and increase the predictable range of LAI. We found that the variance of a moving window, the dimensions of which are determined with spatial statistical methods, was a better predictor of ground measured LAI than any of the SVI considered, and that a multiple linear regression model which included texture metrics improved the ability to map LAI across the heavily forested study landscape. Additionally, we employed multi-model selection statistical tools to address the issue of predictor and model selection. Our results show that these methods help to reconcile the observed variability in published LAI models by demonstrating that multiple models and predictor combinations can perform very similarly, and that there is likely no single best model form or predictor set for mapping LAI using remotely sensed data. Finally, we combined the spatial-spectral empirical LAI model with remotely sensed phenological information in a novel model which is capable of mapping the spatiotemporal patterns of LAI at a user-selected temporal interval. This approach was demonstrated using a small area over Duke Forest in central North Carolina where we mapped daily LAI using IKONOS, Landsat, and MODIS data.

Next, I developed an improved method of consistently and accurately classifying time series of remotely sensed images. Though land cover mapping/classification enjoys the most robust literature in all of remote sensing science, there remain significant challenges and limitations. Most efforts to map land cover rely on identifying representative spectral signatures for the various land cover types of interest, and then using statistical and/or machine learning algorithms to map land cover over the entire study area. While this method works well for *ad hoc* land cover mapping, and in situations where only one map of land cover at a specific time is required, there are challenges to scaling this approach to larger spatial scales and for obtaining a multitemporal understanding of land cover patterns.

The main problem is that spectral signatures obtained for a single image are not directly generalizable to images from other areas or from different times. Atmospheric, view/illumination geometry, phenological changes, and surface moisture conditions alter the radiometric properties of individual images and adaptation of either images or spectral signatures is necessary to extend the mapping to other times or areas. Signature extension is a widely employed method of addressing this issue which seeks to radiometrically rectify individual images so that they have common radiometric response by either estimation and removal of effects using radiative transfer models, or by relative adjustments of image radiometric quantities to match a base image. Unfortunately, signature extension methods are limited because it is not possible to remove all image differences, particularly when they result from actual physical changes on the ground (phenological progression, for example), and so the success of signature extension depends critically on the magnitude and character of the image differences. Individually classifying images with unique reference data is an alternative method which alters the spectral signatures to match individual images rather than adjusting radiometric properties of the images themselves. However, this method is extremely time and labor intensive and invites the possibility of semantic confusion between land cover classes at different times. These challenges have been a significant limitation to realizing the potential of long-term image archives to provide global scale understandings of land cover change.

I develop a novel approach which overcomes these limitations and provides an alternative method of classifying time series of remotely sensed images: automatic adaptive signature generalization. The essential concept of the AASG approach is that if land cover changes can be assumed to be rare (i.e. most of the landscape is stable), and locations with stable land cover

may be reliably identified, then spectral signatures which are uniquely adapted to individual images may be automatically derived from these stable locations. A single well classified map of the study area is the only required input in addition to the time series of images. The most significant contribution of this new method is to allow for temporally mismatched images to be classified without resorting to individual classification with unique reference data. In fact, I demonstrate that the AASG method can classify a winter-summer image pair suffering only a modest reduction in overall accuracy relative to an in-season image pair. The method is found to be sensitive to the thresholding parameter used to distinguish stable sites, and we discuss some strategies for selection of this quantity. This development makes significant progress towards leveraging growing data archives to gain an unprecedented understanding of global land cover change.

Finally, I used these improved remote sensing inputs to parameterize ecohydrologic models and assessed the impact of climate and land cover changes on long-term average streamflow and ET in the Eno River basin. Investigations such as this are more important than ever as growing demands on freshwater resources, current and future climate changes, and anthropogenic landscape modification cause uncertainty about the ability of freshwater resources to meet human and ecosystem needs. The observed distribution of freshwater resources on Earth are a result of interacting climate, physical, and biological processes which must be understood in a holistic, coupled manner in order to successfully attribute drivers of hydrologic change and assess future impacts. Intensive scientific inquiry into these subjects has resulted in a wide variety of ecosystem models with varying levels of sophistication and different structural and theoretical approaches. I used two such models which bracket some this variability. The RHESSys model is a well-validated ecohydrological simulation system which couples physically based hydrological, ecological, and climatological submodels. In contrast, WaSSI is an ecosystem water balance and assimilation model which takes an empirical rather than a physical approach to estimation and is developed using *in situ* measurements of water and carbon fluxes and environmental driving variables.

I used both models to simulate the long-term response of streamflow and ET to two climate change scenarios derived from GCM output, and a single hypothetical land cover scenario specifying vegetation compositional changes. Results indicated that climatic drivers, specifically precipitation, dominate the basin's hydrological response. Specifically, increases in annual precipitation lead to increased mean annual streamflows, but changes in precipitation seasonality favoring wetter dormant periods and drier growing seasons may increase water stress in the catchment and increase the occurrences of anomalously low summer streamflows. Changes in vegetation composition produced a measurable effect, but were far less important than climate changes. The two models produced similar responses to climate and land over changes, but had important relative differences. WaSSI simulated higher streamflows and lower evapotranspiration than RHESSys, and RHESSys better replicated the observed patterns of streamflow over a baseline climate period. Taken together, these results indicate the importance of future climate changes in structuring basin level water cycles and cautions that water stress may increase in the Eno and similar areas if future precipitation changes are similar to those predicted by global climate models.

This investigation also illuminated several directions for possible future research. With respect to LAI estimation, it is hoped that other experiments will strengthen the conclusion that texture metrics are able to improve LAI estimation in high biomass stands. However, there is a critical need to better explain the physical processes that are responsible for the

relationship. Though I've previously discussed the various factors which conspire to produce different canopy textures, and sketched a theoretical justification for the relationship between LAI and these textures, there is a critical need to develop a better physical understanding of these processes. This understanding may allow the reconciliation of texture measures across varying sensors and view/illumination/scene geometry which is not currently possible, but is essential if these techniques are to be scaled up in space. The AASG method developed here was demonstrated in its simplest form and there is ample room for methodological improvements. Specific improvements have been discussed previously, but alterations which improve the selection of change thresholds, and implement alternative classification algorithms are the most likely to have immediate positive impacts. So too will further developments in simulation modeling improve scientific understanding of the ways in which climate, topography, and vegetation influence water balances, and how basins will respond to future changes in climate and land cover. Coupling land cover change models with existing ecohydrologic models, and assessing transient climate and land cover dynamics is a natural progression which will increase the reliability of simulation models and provide valuable information to environmental managers and policy makers.

The principal contributions of this research are significantly improved remote sensing methods to map land cover and LAI which overcome many significant existing limitations, and a detailed understanding of the relative roles that climate and land cover play in structuring the hydrologic regime of the Eno basin. It is expected that these advances will have appreciable impacts on the discipline of remote sensing science where the methods developed here may be used and refined to gain improved understandings of historical land cover and vegetation properties, increase the reliability of simulation results through improved accuracy in landscape representation, and more confidently monitor and manage natural resources. Results of the simulation exercises conducted here improve our understanding of how future changes are likely to impact water resource availability in the Eno and similar forested watershed in southeastern United States. These results will help land managers and planners to assess the impacts of various development scenarios, and will help to ensure that existing resources are sustainably managed into the future.

References

Allen, M. R. and Ingram, W. J. (2002). Constraints on future changes in climate and the hydrologic cycle. *Nature*, 419(6903):224–232.

Asner, G. P., Scurlock, J. M. O., and Hicke, J. A. (2003). Global synthesis of leaf area index observations: implications for ecological and remote sensing studies. *Global Ecology and Biogeography*, 12(3):191–205.

Ball, J. T., Berry, J. A., and Woodrow, I. (1988). Photosynthetic biochemistry, the environment, and control of transpiration. *Plant Physiology (Rockville)*, 86(4 SUPPL).

Band, L. E., Patterson, P., Nemani, R., and Running, S. W. (1993). Forest ecosystem processes at the watershed scale - incorporating hillslope hydrology. *Agricultural and Forest Meteorology*, 63(1-2):93–126.

Baraldi, A. and Parmiggiani, F. (1995). An investigation of the textural characteristics associated with gray-level cooccurence matrix statistical parameters. *IEEE Transactions on Geoscience and Remote Sensing*, 33(2):293–304.

Baret, F. and Guyot, G. (1991). Potentials and limits of vegetation indexes for LAI and APAR assessment. *Remote Sensing of Environment*, 35(2-3):161–173.

Baron, J. S., Hartman, M. D., Kittel, T. G. F., Band, L. E., Ojima, D. S., and Lammers, R. B. (1998). Effects of land cover, water redistribution, and temperature on ecosystem processes in the south platte basin. *Ecological Applications*, 8(4):1037–1051.

Betts, R. A., Boucher, O., Collins, M., Cox, P. M., Falloon, P. D., Gedney, N., Hemming, D. L., Huntingford, C., Jones, C. D., Sexton, D. M. H., and Webb, M. J. (2007). Projected increase in continental runoff due to plant responses to increasing carbon dioxide. *Nature*, 448(7157):1037–U5.

Beven, K. and Kirkby, M. (1979). A physically-based, variable contributing area model of basin hydrology. *Hydrological Sciences Bulletin*, 24(43–69).

Bonan, G. B. (1993). Importance of leaf-area index and forest type when estimating photosynthesis in boreal forests. *Remote Sensing of Environment*, 43(3):303–314.

Bosch, J. M. and Hewlett, J. D. (1982). A review of catchment experiments to determine the effect of vegetation changes on water yield and evapotranspiration. *Journal of Hydrology*, 55(1-4):3–23.

Botkin, D., Estes, J., MacDonal, R., and Wilson, M. (1984). Studying the Earth's vegetation from space. *Bioscience*, 34(8):508–514.

Breda, N. J. J. (2003). Ground-based measurements of leaf area index: a review of methods, instruments and current controversies. *Journal of Experimental Botany*, 54(392):2403–2417.

Brohan, P., Kennedy, J., Harris, I., Tett, S., and Jones, P. (2006). Uncertainty estimates in regional and global observed temperature changes: A new data set from 1850. *Journal of Geophysical Research-Atmospheres*, 111(D12).

Brown, A. E., Zhang, L., McMahon, T. A., Western, A. W., and Vertessy, R. A. (2005a). A review of paired catchment studies for determining changes in water yield resulting from alterations in vegetation. *Journal of Hydrology*, 310(1-4):28–61.

Brown, D. G., Johnson, K. M., Loveland, T. R., and Theobald, D. M. (2005b). Rural land-use trends in the conterminous united states, 1950-2000. *Ecological Applications*, 15(6):1851–1863.

Brown, L., Chen, J. M., Leblanc, S. G., and Cihlar, J. (2000). A shortwave infrared modification to the simple ratio for LAI retrieval in boreal forests: An image and model analysis. *Remote Sensing of Environment*, 71(1):16–25.

Bruniquel-Pinel, V. and Gastellu-Etchegorry, J. P. (1998). Sensitivity of texture of high resolution images of forest to biophysical and acquisition parameters. *Remote Sensing of Environment*, 65(1):61–85.

Buckley, T. N. (2005). The control of stomata by water balance. *New Phytologist*, 168(2):275–291.

Burkett, V., Ritschard, R., McNulty, S., J.J., O., Abt, R., Jones, J., Hatch, U., Murray, B., Jagtap, S., and Cruise, J. (2000). Climate change impacts on the United States. ch. 5: Potential consequences of climate variability and change for the southeastern United States. Technical report, US Global Change Research Program.

Burnham, K. and Anderson, D. (2002). *Model selection and multimodel inference: a practical information-theoretic approach*. Springer, New York.

Cannell, M. G. R. (1999). Environmental impacts of forest monocultures: water use, acidification, wildlife conservation, and carbon storage. *New Forests*, 17(1-3):239–262.

Carper, W. J., Lillesand, T. M., and Kiefer, R. W. (1990). The use of intensity-hue-saturation transformations for merging SPOT panchromatic and multispectral image data. *Photogrammetric Engineering and Remote Sensing*, 56(4):459–467.

Carr, J. R. and de Miranda, F. P. (1998). The semivariogram in comparison to the co-occurrence matrix for classification of image texture. *IEEE Transactions on Geoscience and Remote Sensing*, 36(6):1945–1952.

Chander, G., Markham, B. L., and Helder, D. L. (2009). Summary of current radiometric calibration coefficients for Landsat MSS, TM, ETM+, and EO-1 ALI sensors. *Remote Sensing of Environment*, 113(5):893–903.

Chavez, P. S., Sides, S. C., and Anderson, J. A. (1991). Comparison of 3 different methods to merge multiresolution and multispectral data: Landsat TM and SPOT panchromatic. *Photogrammetric Engineering and Remote Sensing*, 57(3):295–303.

Chen, J., Liu, J., Cihlar, J., and Goulden, M. (1999). Daily canopy photosynthesis model through temporal and spatial scaling for remote sensing applications. *Ecological Modelling*, 124(2–3):99–119.

Chen, J., Liu, J., Leblanc, S., Lacaze, R., and Roujean, J. (2003). Multi-angular optical remote sensing for assessing vegetation structure and carbon absorption. *Remote Sensing of Environment*, 84(4):516–525.

Chen, J. M. (1996). Optically-based methods for measuring seasonal variation of leaf area index in boreal conifer stands. *Agricultural and Forest Meteorology*, 80(2-4):135–163.

Chen, J. M. and Black, T. A. (1992). Defining leaf-area index for non-flat leaves. *Plant Cell and Environment*, 15(4):421–429.

Chen, J. M. and Cihlar, J. (1996). Retrieving leaf area index of boreal conifer forests using Landsat TM images. *Remote Sensing of Environment*, 55(2):153–162.

Chen, J. M., Govind, A., Sonnentag, O., Zhang, Y. Q., Barr, A., and Amiro, B. (2006). Leaf area index measurements at Fluxnet-Canada forest sites. *Agricultural and Forest Meteorology*, 140(1-4):257–268.

Clapp, R. and Hornberger, G. (1978). Empirical equations for some soil hydraulic properties. *Water Resources Research*, 14(4):601–604.

Cohen, W. B., Spies, T. A., and Bradshaw, G. A. (1990). Semivariograms of digital imagery for analysis of conifer canopy structure. *Remote Sensing of Environment*, 34(3):167–178.

Collatz, G. J., Ball, J. T., Grivet, C., and Berry, J. A. (1991). Physiological and environmental-regulation of stomatal conductance, photsynthesis and transpiration- a model that includes a laminar boundary-layer. *Agricultural and Forest Meteorology*, 54(2-4):107–136.

Colombo, R., Bellingeri, D., Fasolini, D., and Marino, C. M. (2003). Retrieval of leaf area index in different vegetation types using high resolution satellite data. *Remote Sensing of Environment*, 86(1):120–131.

Congalton, R. G. (1991). A review of assessing the accuracy of classifications of remotely sensed data. *Remote Sensing of Environment*, 37(1):35–46.

Coppin, P. and Bauer, M. (1996). Change detection in forest ecosystems with remote sensing digital imagery. *Remote Sensing Reviews*, 13:207–234.

Cowan, I. R. and Farquhar, G. D. (1977). Stomatal function in relation to leaf metabolism and environment. In *Symposium for the Society of Experimental Biology*, volume 31, pages 471–505.

Cowling, S. A. and Field, C. B. (2003). Environmental control of leaf area production: Implications for vegetation and land-surface modeling. *Global Biogeochemical Cycles*, 17(1):1007.

Curran, P. J. (1988). The semivariogram in remote sensing: An introduction. *Remote Sensing of Environment*, 24(3):493–507.

DeFries, R. (2008). Terrestrial vegetation in the coupled human-earth system: Contributions of remote sensing. *Annual Review of Environment and Resources*, 33:369–390.

DeFries, R., Foley, J., and Asner, G. (2004). Land-use choices: balancing human needs and ecosystem function. *Frontiers in Ecology and the Environment*, 2(5):249–257.

Defries, R. S. and Townshend, J. R. G. (1994). NDVI-derived land-cover classifications at a global-scale. *International Journal of Remote Sensing*, 15(17):3567–3586.

Drake, B., González-Meler, M., and Long, S. (1997). More efficient plants: A consequence of rising atmospheric co2. *Annual Review of Plant Physiology and Plant Molecular Biology*, 48:609–639.

Eagleson, P. S. (1982). Ecological optimality in water–limited natural soil–vegetation systems. 1. theory and hypothesis. *Water Resources Research*, 18(2):325–340.

Farley, K. A., Jobbagy, E. G., and Jackson, R. B. (2005). Effects of afforestation on water yield: a global synthesis with implications for policy. *Global Change Biology*, 11(10):1565–1576.

Farquhar, G. and vonCaemmerer, S. (1982). Modeling photosynthetic response to environmental conditions. In Lange, O., Nobel, P., Osmond, C., and Ziegler, H., editors, *Encyclopedia of Plant Physiology*, volume 12B of *New Series*, pages 549–587. Springer-Verlag.

Farquhar, G. D. and Sharkey, T. D. (1982). Stomatal conductance and photosynthesis. *Annual Review of Plant Physiology and Plant Molecular Biology*, 33:317–345.

Fassnacht, K. S., Gower, S. T., MacKenzie, M. D., Nordheim, E. V., and Lillesand, T. M. (1997). Estimating the leaf area index of North Central Wisconsin forests using the Landsat Thematic Mapper. *Remote Sensing of Environment*, 61(2):229–245.

Ferro, C. J. S. and Warner, T. A. (2002). Scale and texture in digital image classification. *Photogrammetric Engineering and Remote Sensing*, 68(1):51–63.

Field, C. B., Jackson, R. B., and Mooney, H. A. (1995). Stomatal responses to increased co2: implications from the plant to the global scale. *Plant Cell and Environment*, 18(10):1214–1225.

Fiorella, M. and Ripple, W. J. (1993). Determining successional stage of temperate coniferous forests with Landsat satellite data. *Photogrammetric Engineering and Remote Sensing*, 59(2):239–246.

Fischer, A. (1994). A model for the seasonal variations of vegetation indices in coarse reslution data and its inversion to extract crop parameters. *Remote Sensing of Environment*, 48(2):220–230.

Fisher, J. I., Mustard, J. F., and Vadeboncoeur, M. A. (2006). Green leaf phenology at Landsat resolution: Scaling from the field to the satellite. *Remote Sensing of Environment*, 100(2):265–279.

Foley, J. A., DeFries, R., Asner, G. P., Barford, C., Bonan, G., Carpenter, S. R., Chapin, F. S., Coe, M. T., Daily, G. C., Gibbs, H. K., Helkowski, J. H., Holloway, T., Howard, E. A., Kucharik, C. J., Monfreda, C., Patz, J. A., Prentice, I. C., Ramankutty, N., and Snyder, P. K. (2005). Global consequences of land use. *Science*, 309(5734):570–574.

Foody, G. M. (2002). Status of land cover classification accuracy assessment. *Remote Sensing of Environment*, 80(1):185–201.

Fortier, J., Rogan, J., Woodcock, C. E., and Runfola, D. M. (2011). Utilizing temporally invariant calibration sites to classify multiple dates and types of satellite imagery. *Photogrammetric Engineering and Remote Sensing*, 77(2):181–189.

Fowler, H. J., Blenkinsop, S., and Tebaldi, C. (2007). Linking climate change modelling to impacts studies: recent advances in downscaling techniques for hydrological modelling. *International Journal of Climatology*, 27(12):1547–1578.

Franklin, S. E., Hall, R. J., Moskal, L. M., Maudie, A. J., and Lavigne, M. B. (2000). Incorporating texture into classification of forest species composition from airborne multispectral images. *International Journal of Remote Sensing*, 21(1):61–79.

Franklin, S. E., Maudie, A. J., and Lavigne, M. B. (2001). Using spatial co-occurrence texture to increase forest structure and species composition classification accuracy. *Photogrammetric Engineering and Remote Sensing*, 67(7):849–855.

Franklin, S. E. and Peddle, D. R. (1989). Spectral texture for improved class discrimination in complex terrain. *International Journal of Remote Sensing*, 10(8):1437–1443.

Franklin, S. E. and Wulder, M. A. (2002). Remote sensing methods in medium spatial resolution satellite data land cover classification of large areas. *Progress in Physical Geography*, 26(2):173–205.

Franklin, S. E., Wulder, M. A., and Lavigne, M. B. (1996). Automated derivation of geographic window sizes for use in remote sensing digital image texture analysis. *Computers and Geosciences*, 22(6):665–673.

Friedl, M., McIver, D., Hodges, J., Zhang, X., Muchoney, D., Strahler, A., Woodcock, C., Gopal, S., Schneider, A., Cooper, A., Baccini, A., Gao, F., and Schaaf, C. (2002). Global land cover mapping from MODIS: algorithms and early results. *Remote Sensing of Environment*, 83(1–2):287–302.

Ganguly, S., Samanta, A., Schull, M. A., Shabanov, N. V., Milesi, C., Nemani, R. R., Knyazikhin, Y., and Myneni, R. B. (2008a). Generating vegetation leaf area index earth system data record from multiple sensors. part 2: Implementation, analysis and validation. *Remote Sensing of Environment*, 112(12):4318–4332.

Ganguly, S., Schull, M. A., Samanta, A., Shabanov, N. V., Milesi, C., Nemani, R. R., Knyazikhin, Y., and Myneni, R. B. (2008b). Generating vegetation leaf area index earth system data record from multiple sensors. part 1: Theory. *Remote Sensing of Environment*, 112(12):4333–4343.

Gao, B. C. (1996). NDWI - a normalized difference water index for remote sensing of vegetation liquid water from space. *Remote Sensing of Environment*, 58(3):257–266.

Gao, F., Masek, J., Schwaller, M., and Hall, F. (2006). On the blending of the Landsat and MODIS surface reflectance: Predicting daily Landsat surface reflectance. *IEEE Transactions on Geoscience and Remote Sensing*, 44(8):2207–2218.

Gao, F., Morisette, J. T., Wolfe, R. E., Ederer, G., Pedelty, J., Masuoka, E., Myneni, R., Tan, B., and Nightingale, J. (2008). An algorithm to produce temporally and spatially continuous modis-lai time series. *IEEE Geoscience and Remote Sensing Letters*, 5(1):60–64.

Gower, S. T., Kucharik, C. J., and Norman, J. M. (1999). Direct and indirect estimation of leaf area index, fAPAR, and net primary production of terrestrial ecosystems. *Remote Sensing of Environment*, 70(1):29–51.

GRASS Development Team (2012). *Geographic Resources Analysis Support System (GRASS GIS) Software*. Open Source Geospatial Foundation, USA.

Grier, C. C. and Running, S. W. (1977). Leaf area of mature northwestern coniferous forests – relation to site water-balance. *Ecology*, 58(4):893–899.

Hall, F. G., Strebel, D. E., Nickeson, J. E., and Goetz, S. J. (1991). Radiometric rectification: Toward a common radiometric response among multidate, multisensor images. *Remote Sensing of Environment*, 35(1):11–27.

Haralick, R. M. (1979). Statistical and structural approaches to texture. *Proceedings of the IEEE*, 67(5):786–804.

Haralick, R. M., Shanmuga.K, and Dinstein, I. (1973). Textural features for image classification. *IEEE Transactions on Systems Man and Cybernetics*, SMC3(6):610–621.

Hatton, T. J., Walker, J., Dawes, W. R., and Dunin, F. X. (1992). Simulations of hydroecological responses to elevated co2 at the catchment scale. *Australian Journal of Botany*, 40(4-5):679–696.

Hewitson, B. and Crane, R. (1996). Climate downscaling: Techniques and application. *Climate Research*, 7(2):85–95.

Hewlett, J. D., Lull, H. W., and Reinhart, K. G. (1969). In defense of experimental watersheds. *Water Resources Research*, 5(1):306–316.

Hilker, T., Wulder, M. A., Coops, N. C., Seitz, N., White, J. C., Gao, F., Masek, J. G., and Stenhouse, G. (2009). Generation of dense time series synthetic Landsat data through data blending with MODIS using a spatial and temporal adaptive reflectance fusion model. *Remote Sensing of Environment*, 113(9):1988–1999.

Homer, C., Huang, C. Q., Yang, L. M., Wylie, B., and Coan, M. (2004). Development of a 2001 national land-cover database for the United States. *Photogrammetric Engineering and Remote Sensing*, 70(7):829–840.

Huete, A., Justice, C., and van Leeuwen, W. (1999). MODIS vegetation index (MOD13) algorithm theoretical basis document. Technical report, NASA.

Huntington, T. G. (2006). Evidence for intensification of the global water cycle: Review and synthesis. *Journal of Hydrology*, 319(1-4):83–95.

IPCC (2007). *Climate Change 2007: Contribution of Working Groups I, II and III to the Fourth Assessment Report of the Intergovernmental Panel on Climate Change*. IPCC, Geneva, Switzerland.

Jackson, R. B. and Baker, J. S. (2010). Opportunities and constraints for forest climate mitigation. *Bioscience*, 60(9):698–707.

Jackson, R. B., Carpenter, S. R., Dahm, C. N., McKnight, D. M., Naiman, R. J., Postel, S. L., and Running, S. W. (2001). Water in a changing world. *Ecological Applications*, 11(4):1027–1045.

Jackson, R. B., Farley, K. A., Hoffmann, W. A., Jobbagy, E. G., and L., M. R. (2007). Carbon and water tradeoffs in conversions to forests and shrublands. In Canadell, J., Pataki, D., and Pitelka, L., editors, *Terrestrial Ecosystems in a Changing World.*, chapter 19, pages 237–246. Springer.

Jackson, R. B., Jobbagy, E. G., Avissar, R., Roy, S. B., Barrett, D. J., Cook, C. W., Farley, K. A., le Maitre, D. C., McCarl, B. A., and Murray, B. C. (2005). Trading water for carbon with biological sequestration. *Science*, 310(5756):1944–1947.

Jackson, R. B., Jobbagy, E. G., and Nosetto, M. D. (2009). Ecohydrology in a human-dominated landscape. *Ecohydrology*, 2(3):383–389.

Jarvis, P. G. (1976). Interpretation of variations in leaf water potential and stomatal conductance found in canopies in the field. *Philosophical Transactions of the Royal Society of London Series B-Biological Sciences*, 273(927):593–610.

Jonckheere, I., Fleck, S., Nackaerts, K., Muys, B., Coppin, P., Weiss, M., and Baret, F. (2004). Review of methods for in situ leaf area index determination. Part I. theories, sensors and hemispherical photography. *Agricultural and Forest Meteorology*, 121(1-2):19–35.

Jonsson, P. and Eklundh, L. (2002). Seasonality extraction by function fitting to time-series of satellite sensor data. *IEEE Transactions on Geoscience and Remote Sensing*, 40(8):1824–1832.

Jordan, C. F. (1969). Derivation of leaf-area index from quality of light on forest floor. *Ecology*, 50(4):663–667.

Katul, G. G., Palmroth, S., and Oren, R. (2009). Leaf stomatal responses to vapour pressure deficit under current and co2-enriched atmosphere explained by the economics of gas exchange. *Plant Cell and Environment*, 32(8):968–979.

Kayitakire, F., Hamel, C., and Defourny, P. (2006). Retrieving forest structure variables based on image texture analysis and IKONOS-2 imagery. *Remote Sensing of Environment*, 102(3-4):390–401.

Knyazikhin, Y., Glassy, J., Privette, J. L., Tian, Y., Lotsch, A., Zhang, Y., Wang, Y., Morisette, J. T., Votava, P., Myneni, R., Nemani, R. R., and Running, S. W. (1999). MODIS leaf area index (LAI) and fraction of photosynthetically active radiation absorbed by vegetation (FPAR) product (MOD15) algorithm theoretical basis document. Technical report, NASA.

Knyazikhin, Y., Martonchik, J. V., Myneni, R. B., Diner, D. J., and Running, S. W. (1998). Synergistic algorithm for estimating vegetation canopy leaf area index and fraction of absorbed photosynthetically active radiation from MODIS and MISR data. *Journal of Geophysical Research-Atmospheres*, 103(D24):32257–32275.

Kobayashi, H., Delbart, N., Suzuki, R., and Kushida, K. (2010). A satellite-based method for monitoring seasonality in the overstory leaf area index of Siberian larch forest. *Journal of Geophysical Research-Biogeosciences*, 115.

Leuning, R., Kelliher, F. M., Depury, D. G. G., and Schulze, E. D. (1995). Leaf nitrogen, photosynthesis, conductance and transpiration - scaling from leaves to canopies. *Plant Cell and Environment*, 18(10):1183–1200.

Loaiciga, H. A., Valdes, J. B., Vogel, R., Garvey, J., and Schwarz, H. (1996). Global warming and the hydrologic cycle. *Journal of Hydrology*, 174(1-2):83–127.

Loveland, T., Sohl, T., Stehman, S., Gallant, A., Sayler, K., and Napton, D. (2002). A strategy for estimating the rates of recent United States land-cover changes. *Photogrammetric Engineering and Remote Sensing*, 68(10):1091–1099.

Lu, D., Mausel, P., Brondizio, E., and Moran, E. (2004). Change detection techniques. *International Journal of Remote Sensing*, 25(12):2365–2407.

Lu, J. B., Sun, G., McNulty, S. G., and Amatya, D. M. (2005). A comparison of six potential evapotranspiration methods for regional use in the southeastern united states. *Journal of the American Water Resources Association*, 41(3):621–633.

Lucas, N. and Curran, P. (1999). Forest ecosystem simulation modelling: the role of remote sensing. *Progress in Physical Geography*, 23(3):391–423.

Masson, V., Champeaux, J. L., Chauvin, F., Meriguet, C., and Lacaze, R. (2003). A global database of land surface parameters at 1-km resolution in meteorological and climate models. *Journal of Climate*, 16(9):1261–1282.

McCarthy, H. R., Oren, R., Finzi, A. C., Ellsworth, D. S., Kim, H. S., Johnsen, K. H., and Millar, B. (2007). Temporal dynamics and spatial variability in the enhancement of canopy leaf area under elevated atmospheric CO2. *Global Change Biology*, 13(12):2479–2497.

McDonnell, J. (1990). A rationale for old water discharge through macropores in a steep, humic catchment. *Water Resources Research*, 26(11):2821–2832.

McGrath, D. A., Evans, J. P., Smith, C. K., Haskell, D. G., Pelkey, N. W., Gottfried, R. R., Brockett, C. D., Lane, M. D., and Williams, E. D. (2004). Mapping land-use change and monitoring the impacts of hardwood-to-pine conversion on the southern cumberland plateau in tennessee. *Earth Interactions*, 8:9.

McNulty, S. G., Vose, J. M., and Swank, W. T. (1996). Potential climate change effects on loblolly pine forest productivity and drainage across the southern united states. *Ambio*, 25(7):449–453.

Mertens, B. and Lambin, E. F. (2000). Land-cover-change trajectories in southern Cameroon. *Annals of the Association of American Geographers*, 90(3):467–494.

Minter, T. C. (1978). Methods of extending crop signatures from one area to another. In *Proceedings of Technical Sessions, the LACIE Symposium*, volume 1–2, pages 757–800. NASA Johnson Space Center.

Monteith, J. . L. (1965). Evaporation and environment. *Symposia of the Society for Experimental Biology*, 29(205-234).

Myneni, R. B., Hoffman, S., Knyazikhin, Y., Privette, J. L., Glassy, J., Tian, Y., Wang, Y., Song, X., Zhang, Y., Smith, G. R., Lotsch, A., Friedl, M., Morisette, J. T., Votava, P., Nemani, R. R., and Running, S. W. (2002). Global products of vegetation leaf area and fraction absorbed PAR from year one of MODIS data. *Remote Sensing of Environment*, 83(1-2):214–231.

Myneni, R. B., Nemani, R. R., and Running, S. W. (1997). Estimation of global leaf area index and absorbed PAR using radiative transfer models. *IEEE Transactions on Geoscience and Remote Sensing*, 35(6):1380–1393.

Nemani, R., Pierce, L., Running, S., and Band, L. (1993). Forest ecosystem processes at the watershed scale - sensitivity to remotely-sensed leaf-area index estimates. *International Journal of Remote Sensing*, 14(13):2519–2534.

Nemani, R. R. and Running, S. W. (1989). Testing a theoretical climate-soil-leaf area hydrologic equilibrium of forests using satellite data and ecosystem simulation. *Agricultural and Forest Meteorology*, 44(3-4):245–260.

Norby, R. J., DeLucia, E. H., Gielen, B., Calfapietra, C., Giardina, C. P., King, J. S., Ledford, J., McCarthy, H. R., Moore, D. J. P., Ceulemans, R., De Angelis, P., Finzi, A. C., Karnosky, D. F., Kubiske, M. E., Lukac, M., Pregitzer, K. S., Scarascia-Mugnozza, G. E., Schlesinger, W. H., and Oren, R. (2005). Forest response to elevated CO2 is conserved across a broad range of productivity. *Proceedings of the National Academy of Sciences of the United States of America*, 102(50):18052–18056.

Norby, R. J., Sholtis, J. D., Gunderson, C. A., and Jawdy, S. S. (2003). Leaf dynamics of a deciduous forest canopy: no response to elevated co2. *Oecologia*, 136(4):574–584.

Norman, J. M. and Welles, J. M. (1983). Radiative-transfer in an array of canopies. *Agronomy Journal*, 75(3):481–488.

Nunez, J., Otazu, X., Fors, O., Prades, A., Pala, V., and Arbiol, R. (1999). Multiresolution-based image fusion with additive wavelet decomposition. *IEEE Transactions on Geoscience and Remote Sensing*, 37(3):1204–1211.

Oishi, A. C., Oren, R., Novick, K. A., Palmroth, S., and Katul, G. G. (2010). Interannual invariability of forest evapotranspiration and its consequence to water flow downstream. *Ecosystems*, 13(3):421–436.

Oishi, A. C., Oren, R., and Stoy, P. C. (2008). Estimating components of forest evapotranspiration: A footprint approach for scaling sap flux measurements. *Agricultural and Forest Meteorology*, 148(11):1719–1732.

Oki, T. and Kanae, S. (2006). Global hydrological cycles and world water resources. *Science*, 313(5790):1068–1072.

Olthof, I., Butson, C., and Fraser, R. (2005). Signature extension through space for northern landcover classification: A comparison of radiometric correction methods. *Remote Sensing of Environment*, 95(3):290–302.

Parton, W., Mosier, A., Ojima, D., Valentine, D., Schimel, D., Weier, K., and Kulmala, A. (1996). Generalized model for n_2 and n_2o production from nitrification and denitrification. *Global Biogeochemical Cycles*, 10(3):401–412.

Pax-Lenney, M., Woodcock, C., Macomber, S., Gopal, S., and Song, C. (2001). Forest mapping with a generalized classifier and Landsat TM data. *Remote Sensing of Environment*, 77(3):241–250.

Pearce, A. J. and Rowe, L. (1979). Forest management effects on interception, evaporation, and water yield. *Journal of Hydrology (N.Z.)*, 18(73–87).

Peddle, D. R., Johnson, R. L., Cihlar, J., and Latifovic, R. (2004). Large area forest classification and biophysical parameter estimation using the 5-scale canopy reflectance model in multiple-forward-mode. *Remote Sensing of Environment*, 89(2):252–263.

Peterson, D. L., Spanner, M. A., Running, S. W., and Teuber, K. B. (1987). Relationship of Thematic Mapper Simulator data to leaf-area index of temperate coniferous forests. *Remote Sensing of Environment*, 22(3):323–341.

Phillips, N. and Oren, R. (2001). Intra- and inter-annual variation in transpiration of a pine forest. *Ecological Applications*, 11(2):385–396.

Piao, S. L., Friedlingstein, P., Ciais, P., de Noblet-Ducoudre, N., Labat, D., and Zaehle, S. (2007). Changes in climate and land use have a larger direct impact than rising co2 on global river runoff trends. *Proceedings of the National Academy of Sciences of the United States of America*, 104(39):15242–15247.

Pielke, R. A., Avissar, R., Raupach, M., Dolman, A. J., Zeng, X. B., and Denning, A. S. (1998). Interactions between the atmosphere and terrestrial ecosystems: influence on weather and climate. *Global Change Biology*, 4(5):461–475.

Pilon, P., Howarth, P., Bullock, R., and Adeniyi, P. (1988). An enhanced classification approach to change detection in semi-arid environments. *Photogrammetric Engineering and Remote Sensing*, 54(12):1709–1716.

Puissant, A., Hirsch, J., and Weber, C. (2005). The utility of texture analysis to improve per-pixel classification for high to very high spatial resolution imagery. *International Journal of Remote Sensing*, 26(4):733–745.

Ridd, M. and Liu, J. (1998). A comparison of four algorithms for change detection in an urban environment. *Remote Sensing of Environment*, 63(2):95–100.

Roberts, J. (1983). Forest transpiration: A conservative hydrological process? *Journal of Hydrology*, 66(1–4):133–141.

Robinson, P. J. (2006). Implications of long-term precipitation amount changes for water sustainability in North Carolina. *Physical Geography*, 27(4):286–296. Congress of the International-Geographical-Union, Glasgow, SCOTLAND, ,.

Rodriguez-Iturbe, I. (2000). Ecohydrology: A hydrologic perspective of climate-soil-vegetation dynamics. *Water Resources Research*, 36(1):3–9.

Rogan, J., Franklin, J., Stow, D., Miller, J., Woodcock, C., and Roberts, D. (2008). Mapping land-cover modifications over large areas: A comparison of machine learning algorithms. *Remote Sensing of Environment*, 112(5):2272–2283.

Rouse, J. W., Haas, R. H., Schell, J. A., and Deering, D. W. (1973). Monitoring vegetation systems in the Great Plains with ERTS. In Freden, S. C., Mercanti, E. P., and Becker, M. A., editors, *Third Earth Resources Technology Satellite–1 Symposium–Volume I: Technical Presentations*.

Running, S. W. and Hunt, E. R. (1993). Generalization of a forest ecosystem process model for other biomes, BIOME-BGC, and an application for global-scale models. In Ehleringer, J. R. and Field, C. B., editors, *Scaling physiological processes: leaf to globe*. Academic Press, San Diego.

Running, S. W. and Nemani, R. R. (1991). Regional hydrologic and carbon balance responses of forests resulting from potential climate change. *Climatic Change*, 19(4):349–368.

Running, S. W., Nemani, R. R., and Hungerford, R. D. (1987). Extrapolation of synoptic meteorological data in mountainous terrain and its use for simulating forest evapotranspiration and photosynthesis. *Canadian Journal of Forest Research*, 17(6):472–483.

Running, S. W., Nemani, R. R., Peterson, D. L., Band, L. E., Potts, D. F., Pierce, L. L., and Spanner, M. A. (1989). Mapping regional forest evapotranspiration and photosythesis by coupling satellite data with ecosystem simulation. *Ecology*, 70(4):1090–1101.

Running, S. W., Peterson, D. L., Spanner, M. A., and Teuber, K. B. (1986). Remote-sensing of coniferous forest leaf-area. *Ecology*, 67(1):273–276.

Rutter, A. J. (1963). Studies in the water relations of pinus-sylvestris in plantation conditions. i. measurements of rainfall and interception. *Journal of Ecology*, 51(1):191–203.

Sader, S. (1995). Spatial characteristics of forest clearing and vegetation regrowth as detected by Landsat Thematic Mapper imagery. *Photogrammetric Engineering and Remote Sensing*, 61(9):1145–1151.

Scanlon, B. R., Jolly, I., Sophocleous, M., and Zhang, L. (2007). Global impacts of conversions from natural to agricultural ecosystems on water resources: Quantity versus quality. *Water Resources Research*, 43(3):W03437.

Sellers, P. J., Dickinson, R. E., Randall, D. A., Betts, A. K., Hall, F. G., Berry, J. A., Collatz, G. J., Denning, A. S., Mooney, H. A., Nobre, C. A., Sato, N., Field, C. B., and HendersonSellers, A. (1997). Modeling the exchanges of energy, water, and carbon between continents and the atmosphere. *Science*, 275(5299):502–509.

Semenov, M. and Barrow, E. (1997). Use of a stochastic weather generator in the development of climate change scenarios. *Climatic Change*, 35(4):397–414.

Semenov, M., Brooks, R., Barrow, E., and Richardson, C. (1998). Comparison of the WGEN and LARS-WG stochastic weather generators for diverse climates. *Climate Research*, 10(2):95–107.

Shiklomanov, I. A. (2000). Appraisal and assessment of world water resources. *Water International*, 25(1):11–32.

Singh, A. (1989). Digital change detection techniques using remotely-sensed data. *International Journal of Remote Sensing*, 10(6):989–1003.

Song, C. (2007). Estimating tree crown size with spatial information of high resolution optical remotely sensed imagery. *International Journal of Remote Sensing*, 28(15):3305–3322.

Song, C. and Dickinson, M. B. (2008). Extracting forest canopy structure from spatial information of high resolution optical imagery: tree crown size versus leaf area index. *International Journal of Remote Sensing*, 29(19):5605 – 5622.

Song, C. and Woodcock, C. E. (2003). Estimating tree crown size from multiresolution remotely sensed imagery. *Photogrammetric Engineering and Remote Sensing*, 69(11):1263–1270.

Song, C., Woodcock, C. E., Seto, K. C., Lenney, M. P., and Macomber, S. A. (2001). Classification and change detection using Landsat TM data: When and how to correct atmospheric effects? *Remote Sensing of Environment*, 75(2):230–244.

Song, C. H., Dickinson, M. B., Su, L. H., Zhang, S., and Yaussey, D. (2010). Estimating average tree crown size using spatial information from IKONOS and QuickBird images: Across-sensor and across-site comparisons. *Remote Sensing of Environment*, 114(5):1099–1107.

Song, C. H. and Woodcock, C. E. (2002). The spatial manifestation of forest succession in optical imagery - the potential of multiresolution imagery. *Remote Sensing of Environment*, 82(2-3):271–284.

Soudani, K., Francois, C., le Maire, G., Le Dantec, V., and Dufrene, E. (2006). Comparative analysis of IKONOS, SPOT, and ETM+ data for leaf area index estimation in temperate coniferous and deciduous forest stands. *Remote Sensing of Environment*, 102(1-2):161–175.

Spanner, M., Johnson, L., Miller, J., McCreight, R., Freemantle, J., Runyon, J., and Gong, P. (1994). Remote-sensing of seasonal leaf-area index across the Oregon transect. *Ecological Applications*, 4(2):258–271.

Spanner, M. A., Pierce, L. L., Peterson, D. L., and Running, S. W. (1990). Remote-sensing of temperate coniferous forest leaf-area index – the influence of canopy closure, understorey vegetation and background reflectance. *International Journal of Remote Sensing*, 11(1):95–111.

St-Onge, B. A. and Cavayas, F. (1995). Estimating forest stand sructure from high-resolution imagery using the directional variogram. *International Journal of Remote Sensing*, 16(11):1999–2021.

Stednick, J. D. (1996). Monitoring the effects of timber harvest on annual water yield. *Journal of Hydrology*, 176(1-4):79–95.

Stehman, S. (1999). Basic probability sampling designs for thematic map accuracy assessment. *International Journal of Remote Sensing*, 29(12):2423–2441.

Stehman, S. V. and Wickham, J. D. (2011). Pixels, blocks of pixels, and polygons: Choosing a spatial unit for thematic accuracy assessment. *Remote Sensing of Environment*, 115(12):3044 – 3055.

Stoy, P. C., Katul, G. G., Siqueira, M. B. S., Juang, J. Y., Novick, K. A., McCarthy, H. R., Oishi, A. C., Uebelherr, J. M., Kim, H. S., and Oren, R. (2006). Separating the effects of climate and vegetation on evapotranspiration along a successional chronosequence in the southeastern us. *Global Change Biology*, 12(11):2115–2135.

Sun, G., Alstad, K., Chen, J., Chen, S., Ford, C. R., Lin, G., Liu, C., Lu, N., McNulty, S. G., Miao, H., Noormets, A., Vose, J. M., Wilske, B., Zeppel, M., Zhang, Y., and Zhang, Z. (2011a). A general predictive model for estimating monthly ecosystem evapotranspiration. *Ecohydrology*, 4(2, SI):245–255.

Sun, G., Amatya, D. M., McNulty, S. G., Skaggs, R. W., and Hughes, J. H. (2000). Climate change impacts on the hydrology and productivity of a pine plantation. *Journal of the American Water Resources Association*, 36(2):367–374.

Sun, G., Caldwell, P., Noormets, A., McNulty, S. G., Cohen, E., Myers, J. M., Domec, J.-C., Treasure, E., Mu, Q., Xiao, J., John, R., and Chen, J. (2011b). Upscaling key ecosystem functions across the conterminous united states by a water-centric ecosystem model. *Journal of Geophysical Research-Biogeosciences*, 116.

Sun, G., McNulty, S. G., Myers, J. A. M., and Cohen, E. C. (2008). Impacts of multiple stresses on water demand and supply across the southeastern united states. *Journal of the American Water Resources Association*, 44(6):1441–1457.

Swank, W. T. and Douglass, J. E. (1974). Streamflow greatly reduced by converting deciduous hardwood stands to pine. *Science*, 185(4154):857–859.

Swank, W. T. and Miner, N. H. (1968). Conversion of hardwood-covered watersheds to white pine reduces water yield. *Water Resources Research*, 4(5):947–954.

Swift, L. W., Swank, W. T., Mankin, J. B., Luxmoore, R. J., and Goldstein, R. A. (1975). Simulation of evapotranspiration and drainage from mature and clear-cut deciduous forests and young pine plantation. *Water Resources Research*, 11(5):667–673.

Tague, C. and Band, L. (2004). RHESSys: Regional hydro-ecologic simulation system: An object-oriented approach to spatially distributed modeling of carbon, water and nutrient cycling. *Earth Interactions*, 8(19):1–42.

Tague, C., Grant, G., Farrell, M., Choate, J., and Jefferson, A. (2008). Deep groundwater mediates streamflow response to climate warming in the Oregon Cascades. *Climatic Change*, 86(1–2):189–210.

Tague, C., Seaby, L., and Hope, A. (2009). Modeling the eco-hydrologic response of a mediterranean type ecosystem to the combined impacts of projected climate change and altered fire frequencies. *Climatic Change*, 93(1-2):137–155.

Tague, C. L. and Band, L. E. (2001). Evaluating explicit and implicit routing for watershed hydro-ecological models of forest hydrology at the small catchment scale. *Hydrological Processes*, 15(8):1415–1439.

Townshend, J., Justice, C., Gurney, C., and McManus, J. (1992). The impact of misregistration on change detection. *IEEE Transactions on Geoscience and Remote Sensing*, 30(5):1054–1060.

Turner, D. P., Cohen, W. B., Kennedy, R. E., Fassnacht, K. S., and Briggs, J. M. (1999). Relationships between leaf area index and Landsat TM spectral vegetation indices across three temperate zone sites. *Remote Sensing of Environment*, 70(1):52–68.

Verburg, P., de Koning, G., Kok, K., Veldkamp, A., and Bouma, J. (1999). A spatial explicit allocation procedure for modelling the pattern of land use change based upon actual land use. *Ecological Modelling*, 116(1):45–61.

Verger, A., Baret, F., and Weiss, M. (2008). Performances of neural networks for deriving LAI estimates from existing CYCLOPES and MODIS products. *Remote Sensing of Environment*, 112(6):2789–2803.

Verger, A., Baret, F., and Weiss, M. (2011). A multisensor fusion approach to improve LAI time series. *Remote Sensing of Environment*, 115(10):2460–2470.

Vogelmann, J. E., Howard, S. M., Yang, L. M., Larson, C. R., Wylie, B. K., and Van Driel, N. (2001). Completion of the 1990s national land cover data set for the conterminous united states from landsat thematic mapper data and ancillary data sources. *Photogrammetric Engineering and Remote Sensing*, 67(6):650–662.

von Caemmerer, S. and Farquhar, G. D. (1981). Some relationships between the biochemistry of photosynthesis and the gas-exchange of leaves. *Planta*, 153(4):376–387.

Vorosmarty, C. J., Green, P., Salisbury, J., and Lammers, R. B. (2000). Global water resources: Vulnerability from climate change and population growth. *Science*, 289(5477):284–288.

Vose, J. M., Sun, G., Ford, C. R., Bredemeier, M., Ostsuki, K., Wei, A., Zhang, Z., and Zhang, L. (2011). Forest ecohydrological research in the 21st century: what are the critical needs? *Ecohydrology*.

Waring, R. and Running, S. (2007). *Forest ecosystems analysis at multiple scales*. Elsevier Academic Press, 3 edition.

Warner, T. and Steinmaus, K. (2005). Spatial classification of orchards and vineyards with high spatial resolution panchromatic imagery. *Photogrammetric Engineering and Remote Sensing*, 71(2):179–187.

Wear, D. and Greis, J. (2001). The southern forest resource assessment summary report. General technical report, U.S. Department of Agriculture Forest Service.

Weiss, M., Baret, F., Smith, G. J., Jonckheere, I., and Coppin, P. (2004). Review of methods for in situ leaf area index (LAI) determination. Part II. estimation of LAI, errors and sampling. *Agricultural and Forest Meteorology*, 121(1-2):37–53.

Welles, J. M. and Norman, J. M. (1991). Instrument for indirect measurement of canopy architecture. *Agronomy Journal*, 83(5):818–825.

White, E. M., Morzillo, A. T., and Alig, R. J. (2009). Past and projected rural land conversion in the us at state, regional, and national levels. *Landscape and Urban Planning*, 89(1-2):37–48.

White, M. A., Thornton, P. E., Running, S. W., and Nemani, R. R. (2000). Parameterization and sensitivity analysis of the BIOME-BGC terrestrial ecosystem model: Net primary production controls. *Earth Interactions*, 4(3):1–85.

Wigmosta, M. S., Vail, L. W., and Lettenmaier, D. P. (1994). A distributed hydrology-vegetation model for complex terrain. *Water Resources Research*, 30(6):1665–1679.

Wilby, R. and Wigley, T. (1997). Downscaling general circulation model output: a review of methods and limitations. *Progress in Physical Geography*, 21(4):530–548.

Woodcock, C. E., Macomber, S. A., Pax-Lenney, M., and Cohen, W. B. (2001). Monitoring large areas for forest change using landsat: Generalization across space, time and Landsat sensors. *Remote Sensing of Environment*, 78(1-2):194–203.

Woodcock, C. E., Strahler, A. H., and Jupp, D. L. B. (1988). The use of variograms in remote-sensing: 1. scene models and simulated images. *Remote Sensing of Environment*, 25(3):323–348.

Wulder, M., Franklin, S., and Lavigne, M. (1996). High spatial resolution optical image texture for improved estimation of forest stand leaf area index. *Canadian Journal of Remote Sensing*, 22(4):441–449.

Wulder, M. A., LeDrew, E. F., Franklin, S. E., and Lavigne, M. B. (1998). Aerial image texture information in the estimation of northern deciduous and mixed wood forest leaf area index (LAI). *Remote Sensing of Environment*, 64(1):64–76.

Xu, C. (1999). From GCMs to river flow: a review of downscaling methods and hydrologic modelling approaches. *Progress in Physical Geography*, 23(2):229–249.

Yocky, D. A. (1996). Multiresolution wavelet decomposition image merger of Landsat Thematic Mapper and SPOT panchromatic data. *Photogrammetric Engineering and Remote Sensing*, 62(9):1067–1074.

Zhang, L., Dawes, W. R., and Walker, G. R. (2001). Response of mean annual evapotranspiration to vegetation changes at catchment scale. *Water Resources Research*, 37(3):701–708.

Zhang, X. Y., Friedl, M. A., Schaaf, C. B., Strahler, A. H., Hodges, J. C. F., Gao, F., Reed, B. C., and Huete, A. (2003). Monitoring vegetation phenology using MODIS. *Remote Sensing of Environment*, 84(3):471–475.

Zierl, B., Bugmann, H., and Tague, C. L. (2007). Water and carbon fluxes of European ecosystems: An evaluation of the ecohydrological model RHESSys. *Hydrological Processes*, 21(24):3328–3339.